JET PROPULSION

A publication of the
AMERICAN ROCKET SOCIETY

Research and Development

VOLUME 28 **FEBRUARY 1958** **NUMBER 2**

OPERATION FARSIDE

From "off the shelf" to thousands of miles into space

Balloon-carried to 100,000 feet and launched up through the big bubble, the four-stage Operation Farside missile achieved the greatest height ever attained by a man-made object—an estimated 4,000 miles to the edge of outer space.

A cluster of four Thiokol solid propellant Recruit engines supplied the critical first stage take-off thrust, followed by a single Recruit as the second stage.

Farside again emphasized the flight reliability of Thiokol solid propellant rocket engines, whether ground, sea or air-launched. And the five Recruit engines were standard "off-the-shelf" models. The Recruit has been proven time after time for power and performance. Since the engine is a regular production item, precious time and dollars were saved for the Farside project.

Thiokol®

CHEMICAL CORPORATION

TRENTON, N.J. · ELKTON, MD.
HUNTSVILLE, ALA. · MARSHALL, TEXAS
MOSS POINT, MISS. · BRIGHAM CITY, UTAH

*Registered trademark of the Thiokol Chemical Corporation for its liquid polymers, rocket propellants, plasticizers and other chemical products

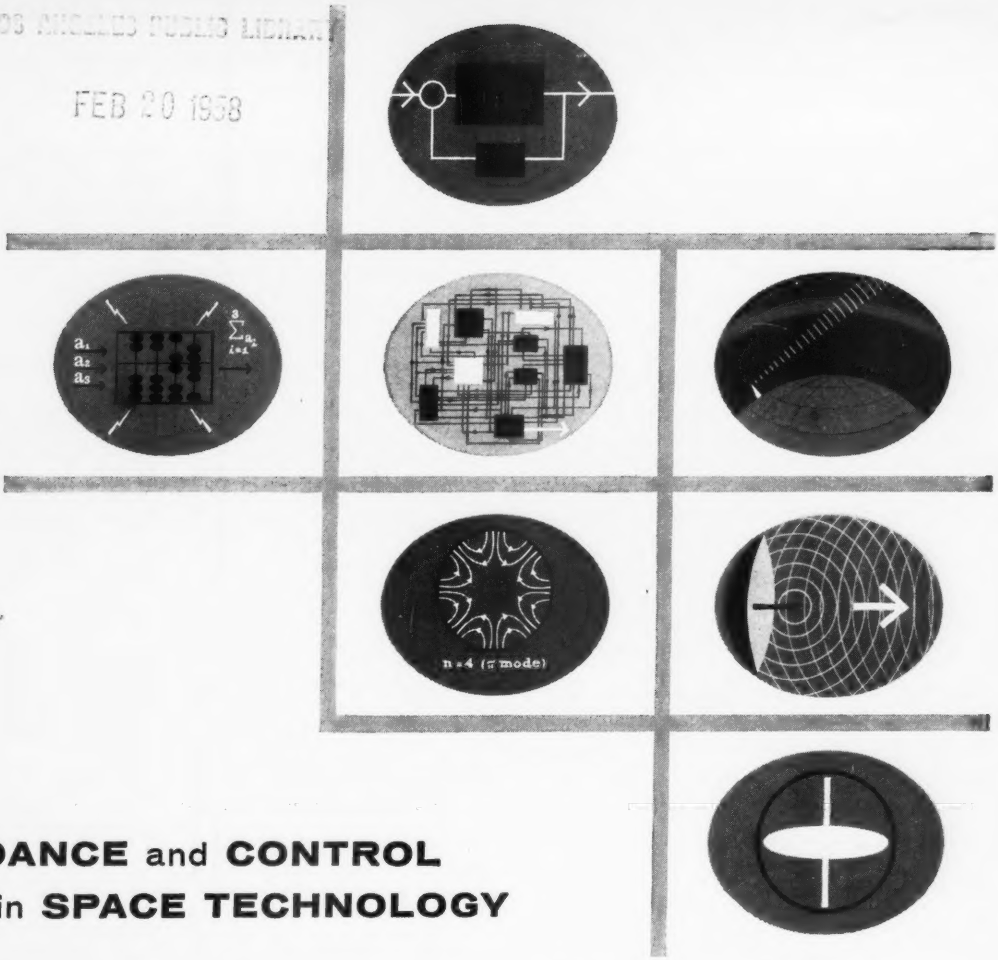

GUIDANCE and CONTROL in SPACE TECHNOLOGY

It is becoming increasingly apparent that many of the techniques and analyses, and much of the equipment, developed for the present Air Force ICBM-IRBM programs will have a wide future application in space technology. For instance, many of the guidance and control techniques for ICBM's are applicable to the space vehicles of the near future.

An important element of these applications is precision. The precision required of the guidance and control system for vehicles aimed at the moon or one of the planets is not substantially greater than that required for the Air Force ICBM-IRBM programs. And, the precision needed to guide a vehicle into a near-circular orbit of Earth is even less than that required for ICBM's.

The problem of communication with lunar and planetary vehicles is, of course, made more difficult by the much greater distances involved. This, however, is not an insurmountable difficulty if today's trends continue in the use of higher transmitted power, narrower communication bandwidths and amplifiers with very low noise-figures.

The problems of operating electronic equipment in the space beyond our atmosphere are already encountered on present ballistic missile trajectories. The principal difference in the case of space vehicle applications is the requirement for longer equipment lifetimes. Electronic equipment and power supplies will have to last for several hours or days or weeks, instead of a few minutes, under conditions of vacuum pressure, zero "g" fields, and bombardment by micrometeorites, high-energy particles, and radiation.

The preceding examples serve to illustrate some of the ways in which the ICBM-IRBM programs are advancing the basic techniques of space technology.

Since 1954, Space Technology Laboratories has been providing over-all systems engineering for these programs. Both in support of this responsibility and in anticipation of future system requirements, the Laboratories are presently engaged in a wide variety of advanced analytical and experimental work directed toward the exploration of new approaches in space vehicle electronics, propulsion, and structures.

The scope of STL's work requires a staff of unusual technical breadth and competence. Engineers and scientists who are interested in advanced experimental development projects (as distinct from development for manufacturing, in which STL is not engaged) are invited to investigate the many opportunities on the Laboratories' Technical Staff.

SPACE TECHNOLOGY LABORATORIES

A Division of The Ramo-Wooldridge Corporation

5730 ARBOR VITAE STREET • LOS ANGELES 45, CALIFORNIA

JET PROPULSION

A publication of the

AMERICAN ROCKET SOCIETY

Research and Development

Scope of JET PROPULSION

This Journal is a publication of the American Rocket Society devoted to the advancement of the field of jet propulsion through the dissemination of original papers disclosing new knowledge or new developments. As used herein, the term "jet propulsion" embraces all engines that develop thrust by rearward discharge of a jet through a nozzle or duct; and thus it includes air-consuming engines and underwater systems as well as rockets. JET PROPULSION is open to contributions dealing not only with propulsion but with other aspects of jet-propelled flight, such as flight mechanics, guidance, telemetering, and research instrumentation. Increasing emphasis will be given to the scientific problems of extraterrestrial flight.

Information for Authors

Manuscripts must be as brief as the proper presentation of the ideas will allow. Exclusion of dispensable material and conciseness of expression will influence the Editors' acceptance of a manuscript. In terms of standard-size double-spaced typed pages, a typical maximum length is 22 pages of text (including equations), 1 page of references, 1 page of abstract, and 12 illustrations. Fewer illustrations permit more text, and vice versa. Greater length will be acceptable only in exceptional cases.

Short manuscripts, not more than one quarter of the maximum length stated for full articles, may qualify for publication as Technical Notes. They may be devoted either to new developments requiring prompt disclosure or to comments on previously published papers. Such manuscripts are usually published within two months of the date of receipt.

Sponsored manuscripts are published occasionally as an ARS service to the industry. A manuscript that does not qualify for publication according to the above-stated requirements as to subject scope or length, but which nevertheless deserves widespread distribution among jet propulsion engineers, may be printed as an extra part of the Journal or as a special supplement, if the author or his sponsor will reimburse the Society for actual publication costs. Estimates are available on request. Acknowledgment of such financial sponsorship appears as a footnote on the first page of the article. Publication is prompt since such papers are not in the ordinary backlog.

Manuscripts must be double spaced on one side of paper only with wide margins to allow for instructions to printer. Include a 100 to 200 word abstract. State the authors' positions and affiliations in a footnote on the first page. Do not type equations; write them in ink. Identify unusual symbols or Greek letters for the printer. References are to be grouped at the end of the manuscript and are to be given as follows: for journal articles: authors first, then title, journal, volume, year, page numbers; for books: authors first, then title, publisher, city, edition, and page or chapter numbers. Line drawings must be clear and sharp to make clear engravings. Use black ink on white paper or tracing cloth. Lettering should be large enough to be legible after reduction. Photographs should be glossy prints, not matte or semi-matte. Each illustration must have a legend; legends should be listed in order on a separate sheet.

Manuscripts must be accomplished by written assurance as to security clearance in the event the subject matter lies in a classified area or if the paper originates under government sponsorship. Full responsibility rests with the author.

Submit manuscripts in duplicate (original plus first carbon, with two sets of illustrations) to the Editor, Martin Summerfield, Professor of Aeronautical Engineering, Princeton University, Princeton, N. J. Preprints of papers presented at ARS national meetings are automatically considered for publication.

JET PROPULSION is published monthly by the American Rocket Society, Inc., and the American Interplanetary Society at 20th & Northampton Sts., Easton, Pa., U. S. A. Editorial offices: 500 Fifth Ave., New York 36, N. Y. Price: $12.50 per year, $2.00 per single copy. Second-class mail privileges authorized at Easton, Pa. Notice of change of address should be sent to the Secretary, ARS, at least 30 days prior to publication. Opinions expressed herein are the authors' and do not necessarily reflect the views of the Editors or of the Society.

Recent Advances In Dynamic Pressure Measurement Techniques

F. F. LIU and T. W. BERWIN

Dresser Dynamics, Inc., A Subsidiary of Dresser Industries, Inc., Northridge, Calif.

Frederick F. Liu is presently executive vice-president of Dresser Dynamics, Inc., a subsidiary of Dresser Industries. Dr. Liu received his B.S.E.E. summa cum laude, China; Dipl. Ing., Germany; B.S.M.E. from CIT; and his doctorate from Princeton University. Entering the rocket research field at the Forrestal Research Center, he designed electronic and rocket measurement systems and co-developed the Li-Liu pickup there. While a research engineering specialist of Rocketdyne, he directed the technical activities of propulsion physics laboratory and made notable contributions in high speed rocket control and measuring devices, and shock wave and hypersonic studies. He serves as a consultant to AEC's KEWB program.

T. W. Berwin received his B.S.E.E. from UCLA, was research engineer at Collins Radio, and later a senior research engineer at Rocketdyne. He has several patents in the electronic field and is currently the head of the electronic division of Dresser Dynamics, Inc.

Introduction

THE development of methods for measuring dynamic pressures has been spurred in recent years largely as a result of the increasing requirements of combustion and other propulsion kinetics research efforts (1).[1] Prior to this, the main efforts in the development and use of such equipment were in the internal combustion engine research fields where significant progress was made. At the present time, however, even these earlier requirements are being exceeded by the demands of high velocity shock wave, detonation and other aerothermodynamic studies (2). These demands have the same basic objective; namely, the determination of the true magnitude of pressure relating to the physical phenomena under study and the recording of its pattern of change with time. They differ, however, in speed requirements. Phenomenological changes can take place within a period of microseconds or shorter: Their pressure-time wave forms often have to be determined with a maximum of accuracy and precision; in other words, with a minimum distortion in amplitude, frequency and phase response.

In this paper a review of some recent advances in pressure measurement as it pertains to rocketry, gas dynamics and nuclear kinetics research are presented together with a critical survey of a number of recent developments. A brief description of several techniques developed by the authors for measuring high speed pressure transients is also included.

The problems involved in dynamic pressure measurement are invariably more complex than those associated with static pressure measurement. In speaking of these problems, it is no longer possible to confine our attention solely to gages and pickups.

It is well understood that whenever there is pressure propagation through a confined channel, there will be associated pressure attenuation due to frictional losses and accompanying modification of the time constant of the original pressure waveform. Moreover, since pressure is related to the rate of deformation, the compressibility effect introduces another time constant and corresponding attenuation factor. If a length of tubing is introduced in the measuring system, the acceleration of the gas as well as the reflection at the end of the tubing will further distort the waveform. These phenomena are well known to fluid dynamicists and recently have been studied rigorously by a number of workers including Iberall (3). From the applied standpoint, rocket engineers have since found out that the thrust chamber pressure pattern as measured through a length of tubing and as measured by a pickup mounted flush in a chamber wall may appear altogether different. The flush mounted pickup is, of course, capable of giving the truer pressure pattern.

The majority of combustion phenomena pertaining to inflammable mixtures may be considered either as deflagration (subsonic) waves, or as detonation (supersonic) waves involving shock. Shock fronts have pressure rise times estimated in the order of millimicroseconds; high frequency oscillations in a small rocket chamber can be 6000 cps or more. When these pressure changes are sensed by systems without the requisite transient and frequency responses, the measurements will be true neither in magnitude nor in "pressure vs. time" waveform. In the space domain a shock front which propagates at a velocity many times the speed of sound has a thickness in terms of mean free paths (20.5×10^{-5} cm for N_2 at 11 atm at Mach 1.128) (4). A 6000 cps pressure oscillation propagating at a velocity of 3600 fps and at a temperature of between 4000 and 5000 F has a wave length of 7.2 in. Due to the transit time effect, a pressure pickup which has a circular diaphragm diameter of,

Presented at the ARS Semi-Annual Meeting, San Francisco, Calif., June 10–13, 1957.

[1] Numbers in parentheses indicate References at end of paper.

for example,[2] $\frac{7}{16}$ in. and which is mounted perpendicular to the propagation direction, will not yield the correct transient waveform since at any time the indicated pressure to a step function p is given by

$$p_{\text{ind}} = KF = K\int_0^A p\,dA$$

$$A = 2\int_{-r/c}^{(x/c)=t} (r^2 - c^2t^2)^{1/2}\, c\,dt = 2c^2\int_{-r/c}^{(x/c)=t} [(r^2/c^2) - t^2]^{1/2}\, dt$$

where p_{ind} and p are the indicated and actual pressure; A is the diaphragm area with radius r; c is the propagation velocity of the phenomenon; F is the pressure-summed force exerted upon the sensing element; t denotes the time; and K is a constant of proportionality.

Thus, in the case of measuring 6000 cps pressure oscillations, the diaphragm covers a length of only about $\frac{1}{16}$ of the wave length or angularly 22 deg. Its indicated value at any time, then, is the mean squared value over this 22 deg arc.

Rocket Engine Dynamic Pressure Pickups

Certain rocket propellant combinations have already attained combustion chamber temperatures above 5000 F, and higher combustion temperatures are in sight. Thus, the development of a dynamic pickup which can operate successfully at such high temperatures for a reasonably prolonged period and withstand acceleration as high as 1000 g without sacrificing appreciably its measurement stability is of practical importance to rocket research. One of the major contributions in this direction, attributed to the cooperative effort between Princeton University and MIT, is the development of the flush-mounted water-cooled Li-Liu pickup. By means of liquid cooling, errors due to thermoelastic sources are kept to a minimum yet the additional coolant mass does not contribute excessive acceleration effects. During the last few years this pickup has proved itself to be a useful tool among rocket research institutions (5). In its earliest stage of development, barring any negligence in the cooling system, the Li-Liu pickup had successfully withstood many rocket firings with estimated temperatures ranging from 4280 to 6200 F under both stable and screaming conditions. The heat transfer rate across the diaphragm as determined by Tischler and his colleagues at NACA Lewis Laboratory was 3.92 Btu/in.^{2}-sec for a screaming run. During this firing the estimated temperature was 6200 F; the water temperature at the entrance of the pickup's cooling system was 64 F; and at the outlet 87.3 F; the coolant flow rate was 0.028 lb/sec.[3] With later adjustments, and with calculations based on the area of the diaphragm alone, a heat transfer rate of 7.6 Btu/in.^{2}-sec was attained. Newer models of super Li-Liu pickups can now achieve even higher heat transfer rates.

The use of water-cooling over thin diaphragms has certainly resolved many previous difficulties. Without efficient cooling a diaphragm made of materials now available cannot endure the flame temperature even for a brief period; the diaphragm would be warped (outward) and the sensing element be damaged so severely as to render dependable measurement virtually impossible. High temperature also causes drastic changes in the elastic moduli of the sensing element. The resultant signal output then becomes erroneous by the standard of room-temperature calibration. These advantages being apparent, it is nevertheless necessary to make an analysis as to whether the coolant also may exert any adverse influence.

Understandably, the coolant between the diaphragms would constitute an additional mass to the moving parts. Consequently, the effects are an increase in the inertial term resulting in greater overshoot and, concurrently, a decrease in natural frequency. The liquid coolant also exerts some damping effect, causing the damping ratio to increase. These effects are evidenced in Figs. 1 and 2 which show the response of the Li-Liu pickup and Photocon pickup to identical step functions from a pneumatic shock. These oscillograms were taken both with and without the cooling water present. (Note the sweep rate of the trace is 20 microsec per centimeter for the Photocon pickup, and 10 microsec per centimeter for the Li-Liu pickup.) The cooling water causes some additional overshoot in both the pickups; the rise time has been increased from approximately 6 microsec to 10 microsec in the case of the Li-Liu pickup, causing its natural frequency to drop from 31.2 kc to approximately 18.7 kc. For the Photocon pickup the rise time increased from approximately 16 to 20 microsec resulting in a decrease of natural frequency from 25 kc to approximately 20 kc. These tests, however, were conducted at extreme conditions with very fast driving functions. During lower frequency operation the cooling water apparently has little or no detrimental effects.

In addition to the Li-Liu pickup and Photocon pressure indicator, several new water-cooled pickups show promise for rocket engine uses. The E. Broza water-cooled *Drucksgeber*, made in Tettnang, West Germany, is a quartz-type pressure transducer; the Omega-Liu pickup utilizes a different cooling technique, lateral cooling of small-diameter diaphragms.

Developments in Pressure Transducer Design

Sensing Elements and Methods of Transduction

Numerous new types of transducing methods for pressure pickups have appeared in recent years (6). In rocket testing the resistive strain gage and capacitance types of pickups are still used most extensively for high frequency combustion chamber pressure measurements. The Li-Liu pickups use the former principle and the Photocon is an example of the capacitance type. The bonded strain gage, particularly when employing mutually crossed type grid windings on a strain tube, has excellent point-by-point temperature compensation and is characterized by low thermal drift over a wide temperature range. First order thermal effects can be reduced to virtually an insignificant magnitude by such compensation techniques. The wire gages add very little mass to the moving elements. They contribute a negligible amount of acceleration sensitivity and do not materially worsen the dynamic performance.

Good linearity is another advantage of the well designed strain gage sensing element if, during the dynamic measurement, the strain $\Delta l/l$ of the elastic element is kept below 0.1 per cent. When coupled to its associated electronic system, the low output impedance of resistive strain gages is a desirable feature because a typical strain gage with resistance on the order of 200 ohm has a capacitance of about 10 mmf and an inductance of 0.015 microhenry. The time constant of the gage itself is thus only about 0.002 microsec. To this, however, must be added the capacitances of the excitation sources (on the order of 100 mmf) and the capacitance of the lead cable (which depends upon the length and type of cable used). These reactances and the stray capacitances should contribute relatively minor factors to the frequency and transient responses of a shielded, d-c excited bridge using resistors of low residual reactances. The upper frequency limit (ω_{lim}) of a strain gage bridge, namely, the 3db point, can be estimated from the relation: $\omega_{\text{lim}} = 1/RC$. Assuming a 200-ohm strain gage pickup having a total active and stray capacitance value of 500 mmf, then, electrically, the strain gage itself should be able to reach an

[2] A few pressure pickups, for instance the sensors produced by Omega Instrument Company, Pasadena, have diaphragm diameters down to $\frac{1}{8}$ in.

[3] Communication from A. O. Tischler to Forrestal Research Center, Princeton University.

upper frequency limit of about 1 megacycle. This, nevertheless, is not practically obtainable due to the limiting dynamic response of the mechanical part of the sensing element. The latter limits most of the commercially available strain-gage pickups to below 100 kc natural frequency. One problem of the bonded-type strain gage is its instability under irradiation by strong neutron flux for prolonged periods. There have been reports of erratic changes of strain gage output up to 10 per cent. The precise nature of such radiation effect, however, has yet to be studied (7).

Many of the advantages of the bonded strain gages are shared by the unbonded strain gages barring such exceptions as the greater residual reactance values and the greater sensitivity to acceleration of the latter (8). The use of unbonded strain gage sensing elements is predominant, however, for low pressure measurements. A disadvantage of both types of strain gages is the relatively low signal output, generally in the millivolt range even when used in a bridge circuit with 6 to 12 volt excitation. Several promising approaches to improve the strain gage output have been made available recently. Statham Laboratories has developed the Zero-length unbonded strain gage which yields an output of up to $\frac{1}{2}$ volt with 12-volt excitation (9). Recently in co-operation with the senior author and under the auspices of a program conducted by the AEC and Atomics International, Statham Laboratories and Dynamic Instrument Company have successfully developed newer types of unbonded gage transducers capable of higher transient response and reasonably suitable for reactor use.

Electronic approaches to this problem include the use of pulse excitation methods, such as those reported by Yates et al. in England and by Sander and Brodie of NACA (10). With such techniques, a short pulse of excitation voltage up to 200 volts can be applied to the bridge momentarily to obtain a high output. In addition, several techniques producing frequency modulation by means of resistance change have been developed, including one by Berwin.

The condenser type of pressure sensing element has large signal output made possible by the frequency modulation or phase-modulation techniques used in the Photocon and Rutishauser systems.[4] Using high carrier frequencies (800 kc for Photocon and 25 megacycles for Rutishauser) it is possible to achieve high sensitivity with minute changes in capacity and also to attain a wide range of frequency response (11).

[4] Newer models now manufactured by Omega Instrument Co., Pasadena; in the strictest sense of the word, Photocon pickups use a quasi-FM electronic system.

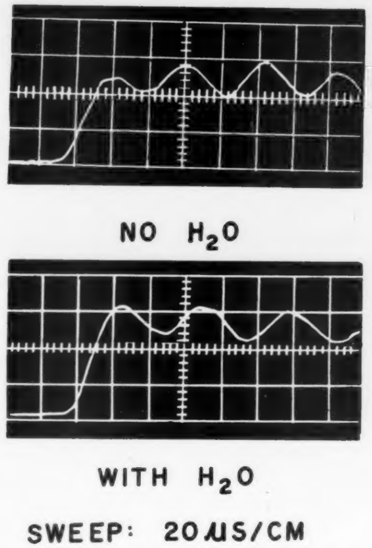

Fig. 1 Response of Photocon pickup to shock wave using nitrogen

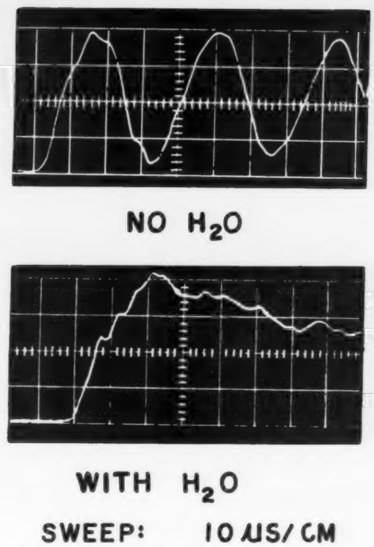

Fig. 2 Response of Li-Liu pickup to shock wave using nitrogen

With an FM system the "number of counts per time period" can be adapted for pressure integration purposes. Although the capacitance principle is not, by itself, strongly susceptible to temperature effects, some capacitance gage systems do suffer seriously from thermal drift. This may be due to the thermoelastic effects on the diaphragm or to changes in the dielectric constant at elevated temperatures. In many atomic energy applications where neutron irradiation effects are anticipated, changes in the dielectric constant due to nuclear activity in a number of capacitative and piezo-electric types of pickups can result in static readings which have no bearing on pressure, sometimes creating errors of from 50 to several hundred per cent (12). The transient response, however, is not likely to be seriously affected over a very short exposure time period.

The capacitance type of pickup has been used rather extensively in Europe. Diehl and Visser at Delft, Holland have developed several such pickups of unique designs (13). The British have a number of outstanding pickups, including those made by Southern Instrument Co. These pickups are used primarily with the FM carrier system.

Electronic pulse techniques have also been used in sensing capacitance changes. Linlor, Kerns and Mark at Berkeley have reported a novel method which they have applied successfully in measuring liquid hydrogen pressure in the presence of pulsed magnetic fields (14). Pulses from a common source feed two cables, one of which is terminated by the pressure measuring capacitor in the pickup, and the other by an adjustable reference capacitor. These pulses are reflected from the terminations in magnitudes corresponding to their respective impedance values, and their difference is amplified and displayed as voltage output by suitable circuitry. The advantage of this method is that distributed capacitance of the cables does not affect the sensitivity of the system. Cables of up to several thousand feet in length can, therefore, be used.

Another new and significant development pertaining to capacitance-type pressure measurement devices is the T-42 ionization transducer credited to Lion of MIT and Switzerland. The system makes use of the gaseous electronic principle of migration of space charges. It consists of a gas ionization tube exposed to a radio frequency field. The electrodes of the ionization tubes are connected to both a reference capacitance C_{ref} and the capacitance C_x to be measured. When there is change in C_x, a relatively large d-c signal is developed so that

$$V_{out} = K\left(\frac{1}{C_{ref}} - \frac{1}{C_x}\right)$$

where C_{ref}, C_x and K have compatible units and K is a constant. Since $C_x = \epsilon\,(A/d)$, the output can be made essentially a linear function of the change of distance d (for small changes of C_x).

Piezo-electric gages have been used for dynamic pressure measurements for many years. Some years ago the "Princeton Unit" was developed for shock wave study and other research physics. Bleakney and Arons have given an authoritative account of this type of pickups in their papers (15). In Germany many developments in piezo-electric pressure transducers were achieved in earlier years. Due to their low curie points and pyroelectric sensitivity, the piezo-electric pickups are not suit-

(*Continued on page 128*)

On the Validity of Continuum Theory for Satellite and Hypersonic Flight Problems at High Altitudes

MAC C. ADAMS[1] and RONALD F. PROBSTEIN[2]

Avco Research Laboratory, Everett, Mass.

A study is made of the validity of continuum flow theory applied to hypersonic flight in a rarefied gas. Order of magnitude estimates are made to establish the flight conditions for which a continuum analysis should be applicable in the stagnation region of a blunt body. Differential equations are presented for the flow in the stagnation region for the flight regime where neither boundary layer theory nor free molecule theory is valid. The results of the study are applied to the problem of re-entry of a satellite and it is concluded that a continuum analysis, with no slip at the body surface, is valid for the flight conditions where heating is important.

Introduction

TSIEN (1)[3] and others (see, e.g., Siegel (2)) have proposed a division of fluid mechanics into various regimes according to the degree of rarefaction as measured by the corresponding range of values of the Knudsen number, defined as the ratio of the mean free path λ to a characteristic flow length. Tsien utilized as a flow length either a characteristic body dimension, which we will denote by R_b, or the boundary layer thickness. Of the various realms into which he and others have categorized fluid mechanics only two of these are reasonably well defined: They are the limiting cases of ordinary continuum gas dynamics where the density is high enough so that intermolecular collisions dominate ($\lambda/R_b \ll 1$), and free molecule flow where the gas is sufficiently rarefied so that collisions with the boundaries dominate ($\lambda/R_b \gg 1$). In between these two limiting regimes there is of course a wide class of flows, although it is generally accepted (see, e.g., p. 381 of (3)) that for $\lambda/R_b > 1$ a gas flow may properly be called rarefied.

In the literature on low density flows (see, e.g., Schaaf and Chambré (4)) it is usually stated that continuum theory breaks down for a rarefied gas flow and that flow problems in this regime require treatment from the point of view of kinetic theory. However, Liepmann and Roshko (3) have pointed out that such a statement is much too strong and very often results from a comparison of a rarefied gas flow experiment with a solution of the Navier-Stokes equations which does not apply to the problem. For example, we would not expect the results of ordinary boundary layer theory, which are valid for high Reynolds numbers, to apply to a rarefied gas flow which is usually a low Reynolds number flow. It is for this reason that the use of the ratio of the mean free path to the boundary layer thickness is not completely satisfactory for defining the regimes of high Mach number rarefied gas flows. Furthermore, regardless of the characteristic length utilized it has been usual to compare this length with the mean free path in the free stream, λ_∞. However, this too is not satisfactory since for hypersonic flight the compression of the gas across the shock wave and at the body increases the local density appreciably, so that the mean free path accordingly decreases in comparison with its free-stream value.

Analysis of Flow Parameters

In order to clarify more specifically the differences in mean free path we note, since $\lambda_\infty \sim \nu_\infty/a_\infty$ (ν_∞ is the kinematic viscosity and a_∞ the speed of sound), that the Knudsen number can be expressed in terms of the free-stream Mach and Reynolds number as

$$\frac{\lambda_\infty}{R_b} \sim \frac{M_\infty}{Re_\infty} \qquad [1]$$

On the other hand, the mean free path behind a shock wave is given by

$$\lambda_s \sim \lambda_\infty \left(\frac{\mu_s}{\mu_\infty}\right)\left(\frac{\rho_\infty}{\rho_s}\right)\left(\frac{a_\infty}{a_s}\right)$$

But $a \sim T^{1/2}$, and at high temperatures the viscosity $\mu \sim T^{1/2}$; hence $\lambda_s \sim \epsilon\lambda_\infty$, where $\epsilon = \rho_\infty/\rho_s$ is the density ratio across the shock wave. Therefore behind a shock wave

$$\frac{\lambda_s}{R_b} \sim \epsilon \frac{M_\infty}{Re_\infty} \qquad [2]$$

Now for air behaving as an ideal gas at hypersonic speeds $\epsilon \to \frac{1}{6}$, while for actual atmospheric hypersonic flight because of the activation of more degrees of freedom (vibration, dissociation) $\epsilon \sim \frac{1}{10}$ to $\frac{1}{15}$. Of course for a weak shock wave $\epsilon \to 1$, and Equation [2] reduces to the usual comparison given by Equation [1].

Carrying our arguments one step further, let us determine the mean free path at the body for the practical hypersonic flight case where the surface temperature is of the order of the free-stream temperature.[4] Under this condition the mean free path at the body $\lambda_b \sim (p_\infty/p_b)\lambda_\infty$. If, for simplicity, we restrict our considerations to the stagnation point region then $p_b/p_\infty \sim \rho_\infty U^2/p_\infty \sim M_\infty{}^2$, and

$$\frac{\lambda_b}{R_b} \sim \frac{1}{M_\infty{}^2}\frac{\lambda_\infty}{R_b} \sim \frac{1}{M_\infty Re_\infty} \qquad [3]$$

We may now inquire as to what our previous results imply in terms of the actual flow field, say in the neighborhood of the stagnation region of a convex blunt body at hypersonic speeds (see Fig. 1). Assuming a continuum flow, from elementary continuity considerations we can determine the thickness Δ of the shock layer at the stagnation point, that is, the distance between the body and the outer edge of the shock wave. The result may be expressed as $\Delta/R_b \approx \rho_\infty/\bar{\rho}$ where R_b refers

Received Nov. 25, 1957.

[1] Deputy Director. Mem. ARS.

[2] Consultant. Also Associate Professor of Engineering, Brown University.

[3] Numbers in parentheses indicate References at end of paper.

[4] The surface temperature will of course be greater than the free-stream temperature. However, unless the surface temperature is considerably in excess of 2000 F, the effect on mean free path at the body surface will not be too significant. For example, at a surface temperature of 2000 F, λ_b will be about five times larger than given by Equation [3].

specifically to the body radius of curvature at the stagnation point and where $\bar{\rho}$ denotes a mean density which is equal in magnitude to the density corresponding to sonic conditions. Since $\rho^*/\rho_0 \sim 0(1)$ (the asterisk denotes sonic conditions and the subscript 0 stagnation conditions) it follows that

$$\frac{\Delta}{R_b} \sim \epsilon \qquad [4]$$

On the other hand, at hypersonic speeds without considering relaxation effects, the shock thickness is given approximately by $\delta_s \sim \mu^*/a^*\rho^*$. Hence for $\mu \sim T^{1/2}$ we have

$$\delta_s \sim \left(\frac{T^*}{T_0}\right)^{1/2}\left(\frac{a_\infty}{a^*}\right)\left(\frac{\rho_0}{\rho^*}\right)\left(\frac{\rho_\infty}{\rho_0}\right)\left(\frac{\mu_\infty}{U\rho_\infty}\right) M_\infty$$

But $(\rho_0/\rho^*) \sim 0(1)$ and $\epsilon \approx \rho_\infty/\rho_0$; hence

$$\frac{\delta_s}{R_b} \sim \epsilon\, \frac{M_\infty}{Re_\infty} \sim \epsilon\, \frac{\lambda_\infty}{R_b} \qquad [5]$$

Since the radius of curvature of the body is of the order of the radius of curvature of the shock wave and since $\epsilon \ll 1$, then one thing we see from Equation [5] is that the shock thickness will be small compared to its radius of curvature so long as $\lambda_\infty/R_b < 0(1)$. Now still assuming the continuum estimates given by Equations [4, 5] to be valid, under what conditions will the shock layer thickness become of the same order as the shock wave thickness (see Fig. 1)? By equating Equations [4] and [5] this will occur for

$$\frac{\lambda_\infty}{R_b} \sim \frac{M_\infty}{Re_\infty} \sim 1 \text{ (shock thickness} \sim \text{shock layer thickness)} \qquad [6]$$

In other words, for the condition of Equation [6] the shock wave and shock layer will have merged into one thin layer. But are continuum concepts valid for this condition?

According to our definition of a rarefied gas we can say that behind the shock wave whenever $\lambda_s/R_b < 1$ the flow behaves as a continuum.[5] However, from Equation [2] this is true whenever

$$\frac{\lambda_\infty}{R_b} \sim \frac{M_\infty}{Re_\infty} < \frac{1}{\epsilon} \qquad \text{(continuum behind shock)} \qquad [7]$$

Thus it is clear from the above condition and Equation [6] that under these circumstances the flow within the merged layer behaves as a continuum.

Mention should also be made of the "ordinary boundary layer thickness" for the flight conditions we have been considering. For example, from the work in (5) it can be shown that at hypersonic speeds for a highly cooled boundary layer the boundary layer thickness in the neighborhood of the stagnation point is given roughly by

$$\delta_{b.l.}{}^2 \sim \left(\frac{\rho_b}{\rho_s}\right)^2 \frac{\nu_b R_b}{U\sqrt{\epsilon}}$$

If we make the same reductions as previously, assuming the body temperature to be of the order of the free-stream temperature, we find that

$$\left(\frac{\delta_{b.l.}}{R_b}\right)^2 \sim \left(\frac{\lambda_\infty}{R_b}\right) M_\infty \epsilon^{3/2} \qquad [8]$$

The ratio of the usual boundary layer to shock layer thickness then becomes

[5] The shock wave in this case is not defined sharply; however λ_s is taken to be of the order of magnitude of the mean free path corresponding to sonic conditions.

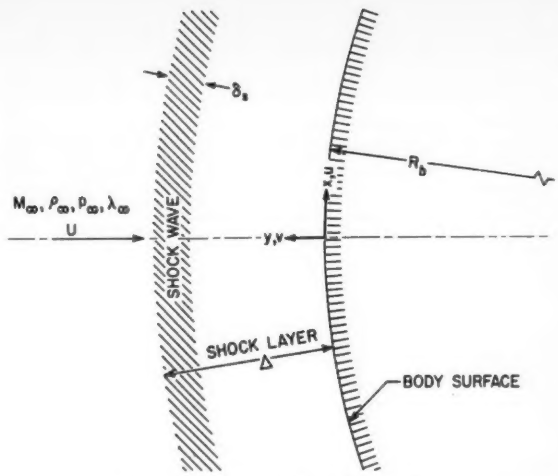

Fig. 1 Schematic diagram of stagnation region for rarefied hypersonic flow

$$\frac{\delta_{b.l.}}{\Delta} \sim \left(\frac{\lambda_\infty}{R_b}\right)^{1/2}\left(\frac{M_\infty}{\sqrt{\epsilon}}\right)^{1/2} \qquad [9]$$

and the inviscid flow region disappears when

$$\frac{\delta_{b.l.}}{\Delta} \sim 1 \quad \text{or} \quad \frac{\lambda_\infty}{R_b} \sim \frac{\sqrt{\epsilon}}{M_\infty}$$

We may now interpret this result in terms of an approach to rarefied gas conditions from the usual continuum gas dynamic regime. That is, considering the direction of increasing mean free path in the free stream we find that the ordinary "inviscid" shock layer has merged with the usual viscous boundary layer to give a fully "viscous" shock layer, before the shock wave begins to thicken appreciably. Thus, we still have a detached shock wave whose thickness is very small compared to the body radius in the region where we can no longer distinguish between an ordinary inviscid and boundary layer behind the shock.

In a similar manner we can examine the familiar continuum gas dynamic "no slip" and "no temperature jump" boundary conditions at the wall. From the usual estimates (see, e.g., (1, 3 or 4)) these effects will be negligible whenever $\lambda_b/R_b \ll 1$. But from Equation [3] we have

$$\frac{\lambda_b}{R_b} \sim \frac{\lambda_\infty}{R_b}\left(\frac{1}{M_\infty{}^2}\right)$$

so that for the mixed flow condition $\lambda_b/R_b \sim 1/M_\infty{}^2$. Hence for $M_\infty \gg 1$ (say $M_\infty > 10$) the condition of "no slip—complete accommodation" will certainly be satisfied. We further note that slip will not become an important factor until λ_∞/R_b is greater than $M_\infty{}^2/10$, (that is, when $\lambda_b/R_b > 0.1$).

While plausible arguments have been made thus far regarding the validity of a continuum analysis, some remarks should be made about the breakdown of this analysis. First of all we should discuss the boundary condition at infinity (i.e., the outer edge of the shock wave). In private discussions with M. Krook, Lecturer on Astronomy, Harvard University, it has been pointed out that in this region the Navier-Stokes equations should be valid, regardless of the mean free path, because the gradients of fluid properties approach zero. Now a breakdown in the Navier-Stokes equations occurs when gradients exist such that any fluid property changes by an appreciable fraction in a distance equal to the local mean free path. A region between the outer boundary of the shock and

the body surface will undoubtedly exist where the continuum equations will be invalid. Without a solution to the problem, one cannot say how large this region is. It is reasonable to state however that the errors involved in using a continuum analysis should be comparable to those in the calculation of a shock wave structure. Further it has been shown (7) that the Navier-Stokes equations give a good approximation to a shock wave structure at low Mach numbers; however no experimental results exist for hypersonic conditions. It is reasonable to assume that the departures from a continuum flow will not lead to first order effects up to the point where the shock and shock layer have merged.

Summing up our previous arguments we can conclude that our continuum equations are still applicable at least up to, and possibly somewhat beyond, the point where the shock wave and shock layer have all merged into one. Thus the Navier-Stokes equations (not the usual boundary layer or shock wave equations) with the usual free-stream boundary conditions and "no slip-complete accommodation" surface conditions can be applied up to the region where the flow begins to behave like a free molecule flow. It follows then that the Navier-Stokes equations should be valid for the "transition" region between ordinary continuum hypersonic aerodynamics and free molecule flow, and the solution of these equations or appropriately simplified forms may give results which go over smoothly to the free molecule answer for slip and accommodation coefficients of one. Such a conclusion also implies that, in contrast to previous thought, the accommodation coefficient for energy transfer in the transition region is not an important consideration, since from our crude analysis it must be of the order of unity.

Simplified Form of Navier-Stokes Equations in Stagnation Point Region for Transition Regime

An order of magnitude analysis has been carried out on the complete Navier-Stokes equations for the case where the shock wave and shock layer are indistinguishable in the neighborhood of a stagnation point on a smooth blunt convex body. The magnitude of the terms in the differential equations can be related to the parameter Δ/R_b, i.e., the ratio of the shock layer thickness to body radius. This ratio is taken to be small, as has been discussed, and in the present approximation terms of order Δ/R_b are neglected in comparison with those of order unity.

One other condition is imposed before arriving at the approximate equations, namely that a boundary layer type phenomenon occurs in a thin shear layer near the body surface. In other words, in this shear layer the flow must be governed by the ordinary boundary layer equations.

The coordinate system is shown on Fig. 1. Standard notation is used and for the sake of brevity the symbols are not defined.

After considerable reduction of the Navier-Stokes equations, the retention of the dominant terms leads to the following equations

x-momentum

$$\rho u u_x + \rho v u_y + \frac{\rho u v}{R_b} = -p_x + (\mu u_y)_y \qquad [10]$$

y-momentum

$$\rho v v_y = -p_y + \frac{4}{3}(\mu v_y)_y \qquad [11]$$

continuity

$$(\rho u x^j)_x + (\rho v x^j)_y = 0 \qquad [12]$$

$j = 0$ plane flow
$j = 1$ axisymmetric flow

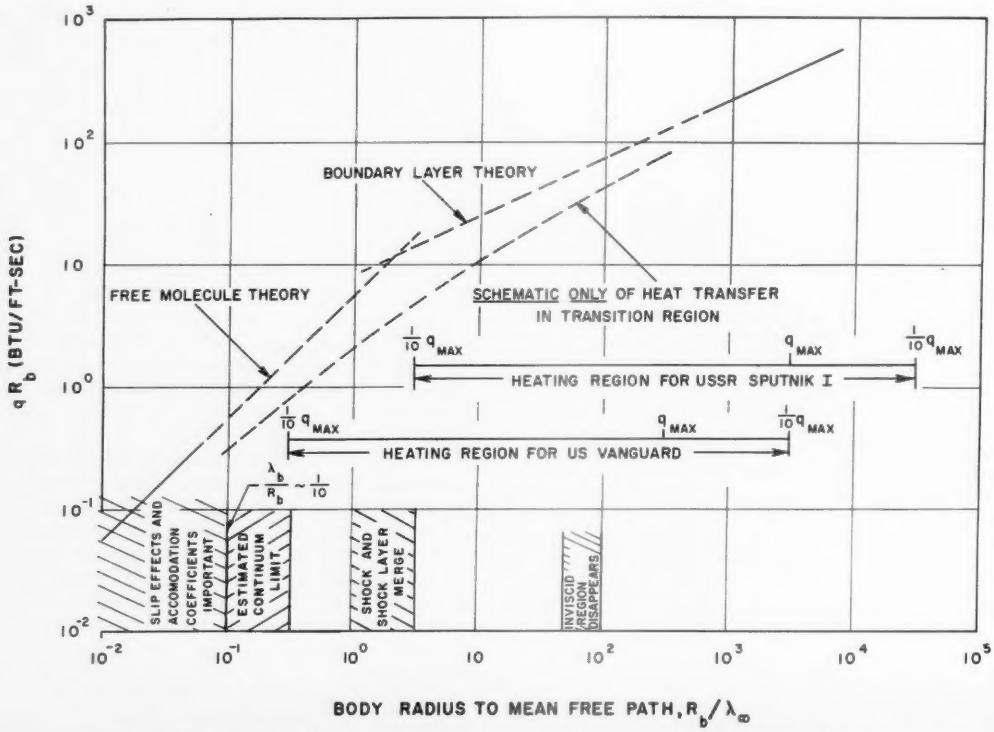

Fig. 2 Flow regimes for the stagnation region of a blunt body at the satellite velocity

energy

$$\rho u\left(h + \frac{v^2}{2}\right)_x + \rho v\left(h + \frac{v^2}{2}\right)_y =$$

$$\left(\frac{k}{c_p} h_y\right)_y + \left(\frac{4}{3}\mu\left(\frac{v^2}{2}\right)_y\right)_y \ldots [13]$$

The boundary conditions consistent with the order of these equations, are

at $y \to \infty$

$$u = U\frac{x}{R_b};\ v = U;\ h = h_\infty \ldots\ldots [14]$$

at $y = 0$

$$u = v = 0; \quad h = \text{wall enthalpy} = h_b \ldots\ldots [15]$$

Solutions of this system of equations should not only cover the condition where the boundary layer and shock wave are mixed but also the high Reynolds number situation where the shock, inviscid flow, and boundary layer are distinct regions.

It can be shown, as expected, that these continuum equations will give a surface heat transfer less than the "free molecule" result. Thus the surface heat transfer calculated from these equations and boundary conditions should pass continuously, with increasing mean free path, from the boundary layer theory toward the free molecule result.

Transition Concepts Applied to Satellite Re-entry

One of the more important problems of low density-high speed flight is associated with the re-entry of a satellite. It is therefore of interest to examine the flight regimes for a body traveling at the satellite velocity and indicate the significance of the results which have been presented.

In order to furnish reference curves for the discussion to follow, we will consider the heat transfer rate to the stagnation point of a sphere traveling at the satellite velocity. Two limiting heat transfer curves are shown on Fig. 2 as a function of the ratio of the body radius to mean free path in the free stream. One curve gives the results of boundary layer theory (6) while the other represents the free molecule heat transfer for an accommodation coefficient of unity. In (6) a simple formula is given for the stagnation point heat transfer rate through a boundary layer. For a body with a surface enthalpy small compared to the stagnation enthalpy the result is

$$q_{b.l.}R_b = 8.15\left(\frac{R_b}{\lambda_\infty}\right)^{1/2}\left(\frac{U}{U_{sat}}\right)^{3.15} \text{Btu/ft-sec} \ldots [16]$$

where U_{sat} denotes the satellite velocity. The free molecule heat transfer rate for an accommodation coefficient of unity is given by

$$q_{f.m.}R_b = 5.72\left(\frac{R_b}{\lambda_\infty}\right)\left(\frac{U}{U_{sat}}\right)^3 \text{Btu/ft-sec} \ldots [17]$$

The intersection of the extrapolation of these two heat transfer curves occurs at a value of $R_b/\lambda_\infty \approx 2$.

It is instructive now to indicate the various flow regimes, in terms of the ratio of the body radius to mean free path R_b/λ_∞. It should be emphasized that these estimates are crude and represent orders of magnitude only. In carrying out these estimates we have taken M_∞ equal to 25 and the density ratio equal to 0.1. The regimes indicated on Fig. 2 are defined as follows:

1 The boundary layer thickness becomes equal to the shock detachment distance eliminating the inviscid flow region. From Equations [4, 8] this occurs when

$$\frac{R_b}{\lambda_\infty} \sim \frac{M_\infty}{\sqrt{\epsilon}} \approx 75$$

2 The shock and boundary layer merge and become indistinguishable. From Equation [6]

$$\frac{R_b}{\lambda_\infty} \approx 1$$

3 The limit of continuum theory according to Equation [7] gives

$$\frac{R_b}{\lambda_\infty} > \epsilon \quad \text{or} \quad \frac{R_b}{\lambda_\infty} > \frac{1}{10}$$

4 A surface "slip" condition is not expected to become important until the ratio of surface mean free path to body radius is the order of $\frac{1}{10}$ (see, e.g., (4)). According to Equation [3] for a surface temperature of the order of the free-stream temperature this condition occurs when

$$\frac{R_b}{\lambda_\infty} \sim \frac{10}{M_\infty^2} \approx \frac{1}{60}$$

For a surface temperature of 2000 F then

$$\frac{R_b}{\lambda_\infty} \approx \frac{1}{10}$$

Finally the regions of important re-entry heating for the two satellites (USSR Sputnik and U. S. Vanguard) are indicated on Fig. 2. These regions were obtained from the results of (6), combined with additional calculations performed by James Hayes of the Avco Research Laboratory. It should be noted that for both satellites the critical heating occurs in a region where the continuum theory should apply and no "slip" occurs at the body surface. Of course noncontinuum theory will play an important role in determining the lifetime of a satellite in its orbit before re-entry.

Acknowledgment

The authors wish to thank Arthur Kantrowitz, who proposed this investigation, and James A. Fay, for his many valuable suggestions and criticisms.

References

1 Tsien, H. S., "Superaerodynamics, Mechanics of Rarefied Gases," *Journal of the Aeronautical Sciences*, vol. 13, 1946, pp. 653–664.

2 Siegel, K. M., "Boundaries of Fluid Mechanics," *Journal of the Aeronautical Sciences*, vol. 17, 1950, pp. 191–192.

3 Liepmann, H. W., and Roshko, A., "Elements of Gasdynamics," Wiley, New York, 1957.

4 Schaaf, S. A., and Chambré, P. L., "Flow of Rarefied Gases," Part G in vol. IV of "High Speed Aerodynamics and Jet Propulsion" Princeton University Press, Princeton, N. J. (to be published).

5 Fay, J. A., and Riddell, F. R., "Theory of Stagnation Point Heat Transfer in Dissociated Air," Research Report 1, Avco Research Laboratory, Everett, Mass., June 1956 (revised April 1957). (To be published in *Journal of the Aeronautical Sciences.*)

6 Kemp, N. H., and Riddell, F. R., "Re-entry Heat Transfer to Satellite Vehicles," Jet Propulsion, vol. 27, Feb. 1957, pp. 132–137, 147.

7 Sherman, F. S., "A Low-Density Wind-Tunnel Study of Shock-Wave Structure and Relaxation Phenomena in Gases," NACA TN 3298, July 1955.

Effect of Air Drag on Elliptic Satellite Orbits

ROBERT E. ROBERSON[1]

North American Aviation, Inc., Downey, Calif.

The eccentricity and characteristic radius of a close satellite orbit decrease with time because of atmospheric drag. Variation of parameters and the Krylov-Bogoliuboff approximation method are used to find simple approximate expressions for the decay of eccentricity with radius, the decay of radius with true anomaly and the growth of true anomaly with time. The special case of spiral orbits and the effect of asphericity and rotation of the earth's atmospheric shell are discussed.

Introduction

A PROBLEM of major concern in satellite engineering is the duration of the satellite on its orbit. Given an initial altitude and orbital eccentricity, how long a time or how many orbital revolutions does it take the satellite to descend to any other assigned altitude? A subsidiary question of importance to tracking, communication and various other operational problems is the way in which eccentricity decays with altitude, time or revolution number.

There are several reasons why the effect of air drag on satellite orbits is rather difficult to analyze. One is the present gross uncertainty as to atmospheric density at extreme altitudes. Another is the uncertainty about a correct drag law and drag coefficient for a body passing through a rarefied gas with extremely high velocity. Not least is the difficulty of solving the nonlinear differential equations of motion, a formidable computation problem even for a high speed digital computer if the descent is to be followed accurately through a large number of revolutions.

It is because of just these facts that an approximate analytic solution is useful if it is easy to apply and gives fair estimates of the true behavior. Parameter values can be changed easily as drag coefficients are better determined, changes in the density function can be encompassed quite readily, and the analytical form of the approximation provides considerable insight into the way in which air drag causes changes in the elements of the orbit.

The effect of air drag on satellite orbits has been discussed by Petersen (4)[2] and others.[3] Reference (4) summarizes some of the geometric and kinematic properties of circular orbits, surveys the literature on the density function for the upper atmosphere,[4] discusses the value of the drag coefficient most appropriate in the domain of free molecular flow, and derives the equations of motion of a satellite subject to air drag, interpreting the acceleration terms which enter these equations.

Three approximate radial decay results are given in (4). The first is based on energy considerations and has been used previously by Sänger and Ehricke, as Petersen observes. The second is a spiral approximate solution to the equations of motion, which is correctly recognized to correspond only to cases of extremely small eccentricity. The third is "a very approximate estimate" obtained by ignoring air drag near apogee and making a rough estimate of the energy extracted by air drag acting near perigee.

This paper is based on the simple drag model[5] and equations of motion presented in (4). Those equations are solved by a method of variation of parameters, approximations being made in the solution of the variation equations. The approximate results are valid for orbital eccentricity which is small, but much larger than that permitted by the spiral solution of that reference. It is shown here that the decay of radius is the same as that given by the approximate treatment from energy considerations.[6] Moreover, there is an additional result on decay of eccentricity which does not seem to have been presented before. Numerical results based on these approximate solutions are included only to compare them with "exact" digital computer solutions for a few numerical cases, thereby to show that the approximate method gives reasonably good answers.

Certain additional topics are discussed briefly in the last section of this paper: The class of spiral orbits found by Petersen (4) and the effect of oblateness and rotation of the earth on the orbits. However, the treatment is descriptive rather than analytical.

Approximate Solution

Basic Equations

With (4), it is assumed that the air drag force is always directed along the satellite negative velocity vector with a magnitude

$$\frac{1}{2} C_D A \rho(h) V^2 \qquad [1]$$

Here C_D is the so-called "drag coefficient," A is the area of the projection of the satellite on the plane normal to its velocity vector, ρ is the ambient atmospheric density as a function of the altitude h above the surface of the earth, and V is the satellite speed. Actually, C_D generally is a function of density and velocity and A depends upon vehicle attitude. However, the assumption that they are both constant over most of the descent path probably is reasonable in this first analysis. It also is assumed that no forces act on the satellite other than those of air drag and the attraction of a spherical earth, and that the atmosphere has a standard stable density which is a function only of the altitude above the surface of the earth.

Under these conditions, the satellite remains in a space-fixed plane, its position described by its radial distance r from the center of the earth and its angular advance β from an arbitrary reference line in the plane of the orbit. It is trivial to show that the equations of motion are

$$\ddot{r} - r\dot{\beta}^2 = -\frac{K}{r^2} - \frac{C_D A}{2m}\rho(h)\dot{r}\sqrt{\dot{r}^2 + r^2\dot{\beta}^2} \qquad [2]$$

Presented at the ARS Semi-Annual Meeting, San Francisco, Calif., June 10–13, 1957.

[1] Staff Specialist, Autonetics Division. Mem. ARS.

[2] Numbers in parentheses indicate References at end of paper.

[3] See, for example, the references given in (4).

[4] To this literature, I would add (1).

[5] The model is capable of considerable generalization without voiding the approach used here, although the details may become more tedious.

[6] This paper utilizes a formal approach through the equations of motion which superficially is quite different from the approach through conservation of energy. The reason why they give the same approximate result will become clear later.

$$r\ddot{\beta} + 2\dot{r}\dot{\beta} = -\frac{C_D A}{2m}\rho(h) r\dot{\beta}\sqrt{\dot{r}^2 + r^2\dot{\beta}^2} \quad \text{[3]}$$

Here K is the product of the mass of the earth by the gravitational constant. It is convenient to introduce auxiliary dimensionless variables

$$\xi = a/r \qquad \eta = Ka/(r^2\dot{\beta})^2 \quad \text{[4]}$$

where a is the equatorial radius of the earth, and to use β as the independent variable. (Primes denote differentiation with respect to this variable.) Also, define the parameter ν by

$$\nu = C_D A\ a/m \quad \text{[5]}$$

For the spherical earth, $h = r - a$ and

$$\rho(h) = \rho(a\xi^{-1} - a) \quad \text{[6]}$$

The basic equations, [2, 3], become

$$\xi'' + \xi = \eta \quad \text{[7]}$$

$$\eta'/\eta = \nu\frac{\rho(a\xi^{-1} - a)}{\xi}\sqrt{1 + (\xi'/\xi)^2} \quad \text{[8]}$$

Variation of Parameters

If there were no air drag, the satellite would follow the ellipse described by

$$\xi = \frac{a}{R}[1 + \epsilon\cos(\beta - \beta_P)] \quad \text{[9]}$$

$$\frac{d\xi}{d\beta} = -\frac{a}{R}\epsilon\sin(\beta - \beta_P) \quad \text{[10]}$$

$$\eta = \frac{a}{R} \quad \text{[11]}$$

where R is a characteristic radius of the orbit related to the radius of the perigee by $R = R_P(1 + \epsilon)$, and β_P is the value of β at the perigee.

The method of solution is based on the requirement that the form of the solution in the presence of air drag be the same as that of Equations [9–11] when R, ϵ and β_P are considered to be slowly varying functions of β. There is no loss of generality in choosing $\beta_P = 0$ when $\beta = 0$, the "initial instant." Denote initial values of R and ϵ by R_i and ϵ_i, respectively.

Bearing in mind that R, ϵ and β_P are to be treated as variables, differentiate Equation [11] and use the result together with Equations [9, 10] in Equation [8]. The result is

$$R' = -\frac{\nu R^2}{a}G(R, \epsilon, \beta - \beta_P) \quad \text{[12]}$$

where

$$G(R, \epsilon, \beta - \beta_P) = \frac{\sqrt{1 + \epsilon^2 + 2\epsilon\cos(\beta - \beta_P)}}{[1 + \epsilon\cos(\beta - \beta_P)]^2}\rho\left\{\frac{R}{1 + \epsilon\cos(\beta - \beta_P)} - a\right\} \quad \text{[13]}$$

Additional differential equations connect R, ϵ, and β_P because there must be consistency among Equations [9–11]. That is, the ξ' found by differentiating Equation [9] must equal that given by Equation [10]; also, because of Equation [7], the ξ'' found by differentiating Equation [10] must equal the difference $\eta - \xi$ formed in using Equations [9, 11]. These equations of consistency are

$$\epsilon'\cos(\beta - \beta_P) + \epsilon\beta_P'\sin(\beta - \beta_P) = \frac{R'}{R}[1 + \epsilon\cos(\beta - \beta_P)] \quad \text{[14]}$$

$$-\epsilon'\sin(\beta - \beta_P) + \epsilon\beta_P'\cos(\beta - \beta_P) = -\frac{R'}{R}\epsilon\sin(\beta - \beta_P) \quad \text{[15]}$$

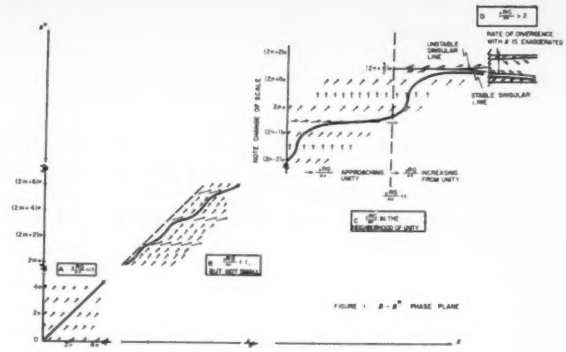

Fig. 1 β-β^* phase plane

from which

$$\epsilon' = -\nu\frac{R}{a}[\epsilon + \cos(\beta - \beta_P)]G(R, \epsilon, \beta - \beta_P) \quad \text{[16]}$$

$$\beta_P' = -\frac{\nu R}{\epsilon a}\sin(\beta - \beta_P)G(R, \epsilon, \beta - \beta_P) \quad \text{[17]}$$

Equations [12, 16, 17] form a basic set for the variation of orbital elements. To provide a guide to the approximations it is reasonable to make in solving these equations, it is useful to consider the topological nature of the solution trajectories in a certain phase plane.

An important preliminary question concerns the magnitude of $\nu G/\epsilon$. For any altitude where the lifetime of the satellite is more than a few days, and for any conceivably realistic satellite area-mass ratio, the product νG is very small, probably one or more orders of magnitude smaller than 10^{-6}. On the other hand, ϵ can be expected to exceed 10^{-3} or 10^{-4}. Therefore, the magnitude of $\nu G/\epsilon$ ordinarily is small enough that its square is negligible for the purposes of this approximate analysis. This chapter is limited to the case for which this is true.

Equation [17] can be rewritten as

$$\frac{d\beta^*}{d\beta} = 1 + \frac{\nu R}{\epsilon a}G(R, \epsilon, \beta^*)\sin\beta^* \quad \text{[18]}$$

where $\beta^* = \beta - \beta_P$. The solutions of this equation are to be examined as a family of trajectories in a $\beta\beta^*$-plane, in which β^* and β are the variables along the axes of ordinates and abscissas, respectively. The particular solution of interest is the one passing through (0, 0) in this phase plane. The several parts of Fig. 1 show the details of several portions of the phase plane which are discussed below in turn.

Because it is supposed that $\nu RG/a\epsilon \ll 1$ initially, Equation [18] shows that the slope of the phase trajectory is initially unity in the $\beta\beta^*$-plane. Because it passes through the origin, the solution appears as shown in part A of Fig. 1. It follows closely along $\beta = \beta^*$ for many periods, as long as $\nu RG/a\epsilon$ is quite small, without significant wiggles. This actually should be a good description of the β, β^* relationship over most of the satellite lifetime, in view of the very small eccentricity which must be reached before it becomes comparable to νG. Physically, this result means that β_P remains zero and that the perigee does not begin to rotate as long as the eccentricity is considerably greater than νG. (Note, however, that perigee rotation from the oblateness of the earth occurs independently of any effect from air drag.)

It is shown later that $\nu RG/a\epsilon$ grows with β. When this parameter has ceased to be small, β^* does not increase as rapidly as β, as shown in part B of Fig. 1. It is this range in which an approximate solution is especially difficult to obtain.

Physically, the perigee begins to rotate positively with a gradually increasing speed.

As $\nu RG/a\epsilon$ approaches and exceeds unity, the situation becomes simpler. Fig. 1,C, shows the behavior for this range of the parameter. The scale of β^* is such that $(2n - (1/2))\pi$ is the last position where $\sin \beta^* = -1$ before the occurrence of $\nu RG/a\epsilon = 1$. As this parameter approaches unity from below, the trajectories cross the $\sin \beta^* = -1$ lines at successively lower angles, so that the trajectory covers a large β range for each 2π increment of β^*. Finally, when $\nu RG/a\epsilon = 1$, two lines whose equations are

$$\sin \beta_0^* = -(\epsilon a/\nu RG) \quad [19]$$

spring into existence at $(2n + (3/2))\pi$ and gradually diverge as the parameter grows (Fig. 1,D). These are lines of zero rate of change of β^* with respect to β. Because they diverge slowly with β, they are essentially horizontal themselves in any small β neighborhood, and act as a horizontal barrier to the phase trajectory.

It can be shown that this qualitative description is correct by considering solutions of Equations [12, 16, 17] in the neighborhood of these singular lines. However, detailed examination of the case where $\nu RG/a\epsilon$ is of the order of unity or greater is not justified except perhaps for very special applications. The radial variation implied by the ϵ corresponding to this range of values would be very small—the order of a few meters for $h = 1000$ km. Such a variation is far overshadowed by eccentricity effects arising from the oblateness of the earth.

This fortifies the restriction imposed previously that only $\nu G/\epsilon$ considerably less than unity is to be considered. The fact that the behavior of the solution in the β, β^* phase plane does not change much until the eccentricity drops far below the range of practical interest, assures that this limitation does not exclude any cases of real importance.

Approximation of $G(R, \epsilon, \beta^*)$

With $d\beta^*/d\beta = 1$ holding very closely over the β range of interest, Equations [12, 16] can be rewritten

$$\frac{dR}{d\beta^*} = -\frac{\nu R^2}{a} G(R, \epsilon, \beta^*) \quad [20]$$

$$\frac{d\epsilon}{d\beta^*} = -\frac{\nu R}{a} (\epsilon + \cos \beta^*) G(R, \epsilon, \beta^*) \quad [21]$$

Successful approximate solution of these equations depends upon the linearization of the nonlinear function $G(R, \epsilon, \beta^*)$.

In simplifying the form of G, one is tempted to expand the density function in Equation [13] in a power series in ϵ, dropping all terms in ϵ of order higher than the first in the resulting expression for G. It is true that the argument of the ρ function can be approximated very closely when second order terms in ϵ are dropped. However, dropping similar terms when ρ is expanded in a Taylor series is equivalent to representing the density at all points of the orbit by the density at the perigee, plus a term for the radial rate of change of density. This procedure is not very accurate for much of the eccentricity range of interest because of the distinctly nonlinear behavior of density with altitude. Alternatively, one can take the point of view that ϵR, half of the maximum total variation of altitude as the orbit is traversed, is not very small relative to the altitude $h = R - a$, so that it should not be used as a small expansion parameter. For example, an eccentricity of $\epsilon = 10^{-2}$ is not large, yet it represents an altitude variation of almost ± 70 km at $h = 500$ km. To fail to handle the expansion of ρ with care may be to sacrifice immediately the possibility of using the results to obtain good numerical information.

A key step is now taken. It is assumed that in a restricted neighborhood of any particular value of ξ, the density function can be approximated by

$$\rho = e^{\alpha\xi + \delta} \quad [22]$$

where, in general, α and δ vary slowly with the ξ (altitude) level. It can be found from Reference (1) that Equation [22] is an excellent representation, with α and δ essentially constant above $R - a = 300$ km, approximately. This analysis treats α and δ as constant over the altitude ranges of interest.

Under these circumstances, one can show that

$$\rho \left\{\frac{R}{1 + \epsilon \cos \beta} - a\right\} = \rho(h) \exp \left\{\kappa\epsilon \cos \beta/(1 + \epsilon \cos \beta)^2\right\} \quad [23]$$

where

$$h = R - a \quad [24]$$

and

$$\kappa = -\frac{R}{\rho(h)}\frac{d\rho}{dh} \quad [25]$$

Then

$$G(R, \epsilon, \beta^*) = \rho(h)e^{\kappa\epsilon \cos \beta^*}[1 - \epsilon \cos \beta^* + 0(\epsilon^2)] \quad [26]$$

and to within terms of the order of ϵ^2, Equations [20, 21] take the forms

$$\frac{dR}{d\beta^*} = -\frac{\nu R^2}{a} \rho(h)e^{\kappa\epsilon \cos \beta^*} (1 - \epsilon \cos \beta^*) \quad [27]$$

$$\frac{d\epsilon}{d\beta^*} = -\frac{\nu R}{a} \rho(h)e^{\kappa\epsilon \cos \beta^*} [\cos \beta^* + \epsilon(1 - \cos \beta^*)] \quad [28]$$

Because the density is very small and $dR/d\beta^*$ and $d\epsilon/d\beta^*$ are correspondingly small, it suggests the applicability of the averaging method of Krylov and Bogolinboff [2]. Approximate differential equations for the behavior of the elements are obtained by averaging the original differential equations over a full period in β^*, removing all of the trigonometric terms in the right-hand sides of Equations [27, 28]. We use the fact (5) that

$$I_n(z) = \frac{1}{\pi}\int_0^{\pi} e^{z \cos \theta} \cos n\theta \, d\theta \quad [29]$$

where $I_n(z)$ is the usual notation for the Bessel function of the first kind for imaginary argument.

Upon averaging, Equations [27, 28] become

$$\frac{dR}{d\beta} = -\frac{\nu R^2}{a} \rho(h)[I_0(\kappa\epsilon) - \epsilon I_1(\kappa\epsilon) + 0(\epsilon^2)] \quad [30]$$

$$\frac{d\epsilon}{d\beta} = -\frac{\nu R}{a} \rho(h)\{I_1(\kappa\epsilon) + \epsilon[I_0(\kappa\epsilon) - I_1(\kappa\epsilon)] + 0(\epsilon^2)\} \quad [31]$$

Note that β has been used interchangeably with β^* in view of previous results. The importance of this representation becomes evident when it is recognized that κ can be of the order of 100 or larger. In this case, for eccentricities of $\epsilon = 0.01$ or larger, the power series expressions corresponding to the functions I_0 and I_1 could not be truncated with ϵ^2 or ϵ^3 terms without disaster. Yet that is precisely what would have been done in expanding G completely into a power series in ϵ.

It is important in the sequel to note that the dominant term in the right-hand side of Equation [30] is $I_0(\kappa\epsilon)$, while the dominant terms in Equation [31] are $I_1(\kappa\epsilon) + \epsilon I_0(\kappa\epsilon)$. The other terms are ignored in our approximate solution.

Solutions

Next, consider the solutions of Equations [30, 31]. Rather than trying to find ϵ directly as a function of β through

Equation [31], it is convenient to divide this equation by Equation [30] to obtain

$$\frac{d\epsilon}{dR} = \frac{\epsilon}{R} + \frac{I_1(\kappa\epsilon)}{RI_0(\kappa\epsilon)} \qquad [32]$$

which, in view of the definition of κ, can be rearranged as

$$\frac{d \ln (\epsilon\sqrt{\rho}/R)}{d \ln R} = \left[\frac{1}{\epsilon}\frac{I_1(\kappa\epsilon)}{I_0(\kappa\epsilon)} - \frac{\kappa}{2}\right] \qquad [33]$$

This can be rewritten as an integral equation

$$\frac{\epsilon R_i}{\epsilon_i R}\sqrt{\frac{\rho(R - a)}{\rho(R_i - a)}} = \exp\left\{\int_{R_i}^{R}\left[\frac{1}{\epsilon}\frac{I_1(\kappa\epsilon)}{I_0(\kappa\epsilon)} - \frac{\kappa}{2}\right]\frac{dR}{R}\right\} \qquad [34]$$

which can be used as the basis for an iterative solution.

Note first that for $\kappa\epsilon \ll 1$, $I_1(\kappa\epsilon) \approx \kappa\epsilon/2$ and $I_0(\kappa\epsilon) \approx 1$, so that the integral on the right-hand side of Equation [34] vanishes to within second order terms in small quantities. For this case, then

$$\epsilon(R) = \frac{\epsilon_i R}{R_i}\sqrt{\frac{\rho(R_i - a)}{\rho(R - a)}} \qquad [35]$$

which may be expected to be very good for ϵ of the order of 0.001 or smaller, with κ of the order of 100.

Now let the result of Equation [35] be used in the right-hand side of Equation [34] as the first step of an iteration process. The product $\kappa\epsilon$ is of the form

$$\kappa\epsilon = \frac{\alpha a\epsilon_i\sqrt{\rho_i}}{R_i}\,\frac{1}{\sqrt{\rho}} \qquad [36]$$

so that

$$\frac{1}{\kappa\epsilon}\frac{d(\kappa\epsilon)}{dR} = \frac{\kappa}{2R} \qquad [37]$$

and by introducing $\kappa\epsilon$ as the variable of integration into the integral in Equation [34] this equation can be written

$$\frac{\epsilon R_i}{\epsilon_i R}\sqrt{\frac{\rho(R - a)}{\rho(R_i - a)}} = \exp\left\{\phi(\kappa_i\epsilon_i) - \phi(\kappa\epsilon)\right\} = \frac{e^{\phi(\kappa_i\epsilon_i)}}{e^{\phi(\kappa\epsilon)}} \qquad [38]$$

Here

$$\phi(\kappa\epsilon) = \int_0^{\kappa\epsilon}\left[1 - \frac{2}{x}\frac{I_1(x)}{I_0(x)}\right]\frac{dx}{x} \qquad [39]$$

and

$$\kappa\epsilon = -\frac{\epsilon_i R^2}{R_i}\sqrt{\frac{\rho(R_i - a)}{[\rho(R - a)]^3}}\,\frac{d\rho(R - a)}{dR} \qquad [40]$$

The functions ϕ and e^{ϕ} are tabulated in Table 1 for a range of $\kappa\epsilon$ which should span all values of interest. Actually, even the very great eccentricity mentioned for Vanguard (apogee altitude 1000 miles, perigee altitude 100 miles) gives a value of $\kappa\epsilon$ no greater than about 12.

If desired, of course, the new value of ϵ obtained from Equation [38] can be used in the right-hand side of Equation [34] to carry the iteration a step further. However, the inherent limitations on the method and uncertainties as to parameter values probably are such that a higher order iteration cannot be justified.

In summary, $\epsilon(R)$ is calculated by using Equation 40 to find $\kappa\epsilon(R)$; then Table 1 to find $e^{\phi(\kappa\epsilon)}/e^{\phi(\kappa_i\epsilon_i)}$. From this result, Equation [38] permits a direct determination of $\epsilon(R)$. It is noteworthy that the result does not depend on ν, which is to say it is independent of the satellite area/mass ratio and the drag coefficient (subject only to the constancy of these quantities assumed previously). Thus it can be found once and for all from a knowledge of the atmospheric density function alone, given the initial altitude and eccentricity.

Table 1 Functions ϕ and e^{ϕ}

$\kappa\epsilon$	$\phi(\kappa\epsilon)$	$e^{\phi(\kappa\epsilon)}$	$\kappa\epsilon$	$\phi(\kappa\epsilon)$	$e^{\phi(\kappa\epsilon)}$
0	0	1.000	2.0	0.1926	1.212
0.1	0.0010	1.001	3.0	0.3446	1.411
0.2	0.0032	1.003	4.0	0.4921	1.636
0.3	0.0063	1.006	5.0	0.6276	1.873
0.4	0.0107	1.011			
0.5	0.0162	1.016	6.0	0.7501	2.117
0.6	0.0227	1.023	7.0	0.8606	2.365
0.7	0.0303	1.031	8.0	0.9611	2.615
0.8	0.0389	1.040	9.0	1.0531	2.867
0.9	0.0483	1.049	10.0	1.1376	3.119
1.0	0.0585	1.060	11.0	1.2156	3.372
1.1	0.0695	1.072	12.0	1.2881	3.626
1.2	0.0813	1.085	13.0	1.3561	3.881
1.3	0.0937	1.098	14.0	1.4201	4.138
1.4	0.1067	1.113	15.0	1.4801	4.393
1.5	0.1201	1.128	16.0	1.5366	4.649
1.6	0.1340	1.143			
1.7	0.1482	1.160			
1.8	0.1628	1.177			
1.9	0 1776	1.194			

Beyond $\kappa\epsilon$ = 16, the asymptotic relation $\phi \sim \ln \kappa\epsilon$ + const is closely valid

We return now to Equation [30] for R as a function of β, keeping only the dominant term on the right-hand side. Because $K = \kappa\epsilon$ is the function of R already found above, a direct integration gives

$$\nu\beta = a\int_R^{R_i}\frac{dR}{R^2\rho(R - a)I_0[\kappa\epsilon]} \qquad [41]$$

This integral is easy to evaluate numerically.

If $\kappa\epsilon \ll 1$, $I_0(K) \approx 1$ and the relative change in altitude per revolution becomes closely equal to

$$\left(\frac{\Delta h}{h}\right)/\text{revolution} = \frac{2\pi\nu R^2\rho(h)}{ah} \qquad [42]$$

which has the general form of Petersen's Equation [40]. It should be expected that this be the same result as obtained from a conservation of energy argument, for it is well known ((3), p. 238) that the Krylov-Bogolinboff averaging method is equivalent to a conservation of energy approach. However, the present result is a generalization which encompasses the effect of ϵ on the radial decay.

After $R(\beta)$ [strictly, $\beta(R)$] is found from Equation [41], the time behavior of the orbit is obtained by returning to the definition of η in Equation [4] and its behavior in terms of R in Equation [11]. From these

$$t = \int_0^{\beta}\sqrt{\frac{R^3(\beta)}{K}}\,d\beta \qquad [43]$$

From Equations [38, 41, 43] all the essential behavoir of an orbit having eccentricity $\nu RGa^{-1} \ll \epsilon \ll 1$ can be inferred semiquantitatively. Note that in both Equations [38, 42] it is natural to use R as the independent variable.

Evaluation

It is important to try to discover how close the approximate results given by Equations [38, 41] and $d\beta^*/d\beta = 1$ are relative to the exact results that would be obtained by solving Equations [12, 16, 17]. A comparison of results for two cases have been made which indicates that the approximate rela-

tions may be quite adequate for engineering purposes.[7]

Equations [12, 16, 17] were solved as a coupled set numerically[8] to give an "exact" solution for a few parameter values. The value[9] of ν was taken as 5×10^6 cm^3/gm and $\rho(h)$ was taken as the upper bound of the estimates of (1). Initial conditions $\beta_i = 0$ and $R_i - a = 400$ km, the latter chosen because it is low enough that changes can soon be seen in the dependent variables, yet high enough that the total lifetime occupies a reasonably large number of revolutions (15,000 to 20,000 radians), thereby setting a rather stiff task for the approximate method. The two values $\epsilon_i = 0.001$ and $\epsilon_i = 0.01$ were considered.

First, it was found that β^* remained equal to β to within less than one part in one million over the β-range considered, thereby fortifying the assumption $\beta^* \equiv \beta$.

Fig. 2 shows the results for $\epsilon_i = 0.001$, both ϵ/ϵ_i and β plotted as functions of R. The solid curve is the exact solution for $\beta(R)$, the dashed curve is the exact solution for $\epsilon(R)/\epsilon_i$, and the small open circles are the values obtained by the approximate method of this paper. As might be expected for such a small ϵ_i, the approximate method gives excellent results, departing only a few per cent from the true values for the smaller altitudes where the satellite is about to fall to earth within a few revolutions.

Fig. 3 is the same as Fig. 2 except that the initial eccentricity is much larger, $\epsilon_i = 0.01$. The agreement between approximate and exact solutions for $\epsilon(R)$ is quite good, as shown by the open circles in relation to the dashed curve. The crosses near these dots show the approximate result that would have been obtained ignoring the departure from unity of the right-hand side of Equation [38].

Unfortunately, the agreement for $\beta(R)$ is not as good. However, the approximate method is not so far in error as to be completely useless. It is of considerable interest to note the importance of retaining the $I_0(\kappa\epsilon)$ term in Equation [41]. Without it, the approximate $\beta(R)$ relationship would be that shown by the open triangles in Fig. 3.

Other Topics

Spiral Orbits

The analytical development above is predicated on the existence of an elliptical first approximation to the motion. It can happen that such an elliptical approximation does not exist, as can be seen physically as follows.

Suppose that at some instant the satellite has a velocity vector with a small component directed toward the earth. Normally, this condition represents the return from an apogee position. The satellite gathers speed as it continues inward toward the earth and eventually reaches perigee with a higher total velocity than it had at the previous apogee. However, if the inward velocity component is very small, corresponding to an orbit which has very little eccentricity, the velocity gain between apogee and perigee is very small. The satellite falls such a short distance toward the earth in reaching perigee that its velocity increases very slowly. In the presence of air drag, the velocity loss from drag may exceed the normal gain from the fall toward the earth, and in this case the perigee is never reached. The path is a spiral rather than an ellipse with decreasing size.

To find the change in radius for a spiral orbit, it is most convenient to return to Equations [7, 8] and seek their solution by iteration. As initial values, use $\xi_i = a/R_i$ and $\eta_i = a/R_i$, but leave open for the moment the choice of ξ_i'. Denote the order of the iteration by superscripts in parentheses and begin with

$$\xi^{(0)}(\beta) = \xi_i;\ \xi^{(0)\prime}(\beta) = 0;\ \eta^{(0)}(\beta) = \eta_i \qquad [44]$$

From Equation [8]

$$\eta^{(1)}(\beta) = \frac{a}{R_i} \exp\, [\nu\rho(R_i - a)\beta] \qquad [45]$$

This used in Equation [7] gives

$$\xi^{(1)}(\beta) = \frac{a}{R} \exp\, [\nu\rho(R_i - a)\beta] \qquad [46]$$

after choosing the coefficients of the solution of the complementary equation equal to zero on the ground that any other choice allows an elliptical approximation to $\xi(\beta)$, contrary to assumption.

From this result it is seen that no freedom remains to choose ξ_i'; one simply must accept the value

$$\xi_i' = \nu a\rho(R_i - a)/R_i \qquad [47]$$

implied by Equation [46].

In terms of the original physical variables, this spiral solution is

$$r(\beta) = R_i e^{-\nu\rho(R_i - a)\beta} \qquad [48]$$

with β closely equal to

$$\beta = \sqrt{\frac{K}{R_i^3}}\, t \qquad [49]$$

This corresponds to the spiral solution given as Petersen's Equation [57], although it has been obtained by a somewhat different argument.

Because this class of spiral orbits corresponds to such an exceedingly small radial velocity, the transition from an elliptic to a spiral orbit must occur for a minescule value of eccentricity. Therefore, spiral orbits are of interest only if the initial eccentricity itself is very small or if the radial distance becomes so small that the satellite is ready to fall precipitously toward the earth. Such small initial eccentricities are extremely improbable, especially in view of the equivalent eccentricity which is induced by the oblateness of the earth (a topic treated by the author elsewhere). Therefore, one concludes that the class of spiral orbits is without practical importance.

Effect of Aspherical Atmospheric Shell

The analysis above has presumed a spherical earth and a spherical atmospheric shell, characterized by our representing altitude as simply $h = r - a$. Actually the earth departs significantly from a sphere, and one may expect the atmospheric shell to be similarly oblate. Let us consider what effect it might have on the analysis to take account of this property.

The oblateness of the earth really has two important effects on the air drag problem. Even neglecting the asphericity of the atmospheric shell, oblateness is important because it generally contributes to the eccentricity of the orbit. I have shown elsewhere that the effective geometric eccentricity of the orbit is compounded of the dynamical eccentricity used in the analysis above and terms proportional to the ellipticity of the earth. If this fact is ignored in establishing the satellite orbit, then the geometric eccentricity is nonzero even if one succeeds in achieving a dynamical eccentricity which just corresponds to a circular orbit.

The second effect arises through the oblateness of the atmospheric shell, and is the one considered below. To get a simple picture of the effect, assume that the density is constant over shells having the same ellipticity as the surface of

[7] It is emphasized that these calculations do not purport to describe the actual behavior of an orbit because of the uncertainty as to a correct value of ν and a correct density function. However, using approximate values in these cases does permit results to be compared which are calculated in two different ways.

[8] By IBM-701 computer.

[9] This large value of ν should give no cause for alarm, for $\nu\rho$ in the neighborhood of 400 km is of the order of 5×10^{-7}. This ν value is conservatively large, and more realistic, smaller values will further improve the approximation method.

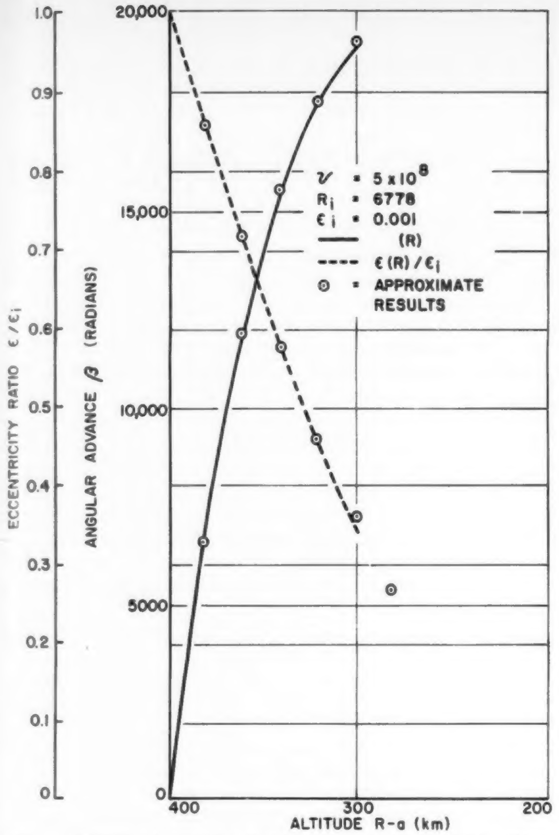

Fig. 2 **Change of eccentricity and angular advance with altitude**

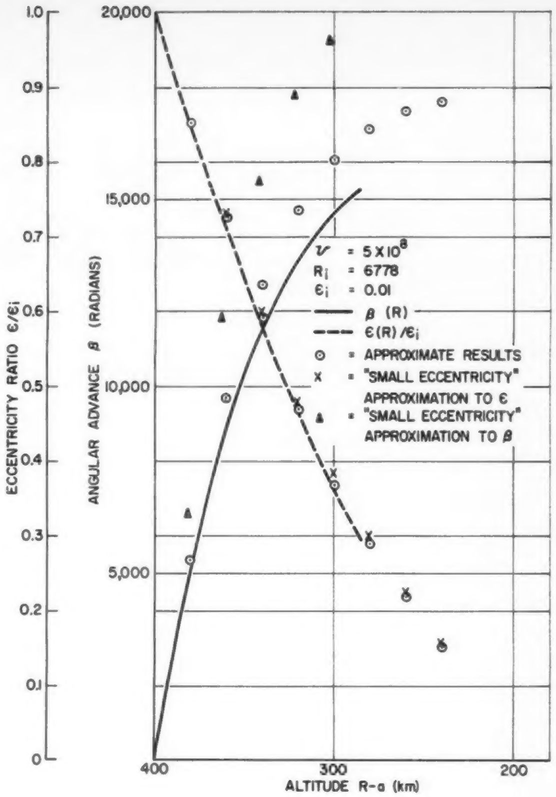

Fig. 3 **Change of eccentricity and angular advance with altitude**

the earth. In this case, one should use in the density function an effective altitude given by

$$h = \frac{R}{1 + \epsilon \cos \beta} - \frac{a}{\sqrt{1 + 2\epsilon^* \sin^2 \lambda}} \quad [50]$$

where

$$2\epsilon^* = (a^2/b^2 - 1) \sin^2 \gamma \quad [51]$$

b = polar radius of the earth
γ = dihedral angle between the plane of the orbit and the earth's equatorial plane, with $0 \leq \gamma \leq \pi$; ($\gamma > \pi/2$ corresponds to retrograde orbits)
λ = geocentric latitude of the satellite

If β_P denotes the angle from the ascending node of the orbit to the perigee (at which $\beta = 0$), positive in the direction of satellite motion, then

$$\sin \lambda = \sin \gamma \sin (\beta + \beta_P) \quad [52]$$

Therefore, the analog of Equation [23] for the case at hand is

$$\rho = \exp\left\{\alpha\left[\frac{1}{1 - \frac{1}{\sqrt{1 + 2\epsilon^* \sin^2 \lambda}} + \frac{R/a}{1 + \epsilon \cos \beta}}\right] + \delta\right\}$$

$$= \rho(R - a) \exp\left\{\kappa\left[\epsilon \cos \beta - \frac{a\epsilon^*}{R} \sin^2 \gamma \sin^2(\beta + \beta_P)\right] + 0(\epsilon^2, \epsilon\epsilon^*, \epsilon^{*2})\right\}$$

$$\approx \rho(R - a)e^{-(a\epsilon^* \sin^2 \gamma)/2R} \exp\left\{\kappa\left[\epsilon \cos \beta + \frac{a\epsilon^*}{2R} \sin^2 \gamma \cos 2(\beta + \beta_P)\right]\right\} \quad [53]$$

Also, to the same order of approximation

$$G(R, \epsilon, \beta^*) = [\rho(R - a)e^{-(a\epsilon^* \sin^2 \gamma)/2R} (1 - \epsilon \cos \beta)] \times \exp\left\{\kappa\epsilon \cos \beta + \frac{\kappa a\epsilon^*}{2R} \sin^2 \gamma \cos 2\beta_P \cos 2\beta\right\} \times \left[1 - \frac{\kappa a\epsilon^*}{2R} \sin^2 \gamma \sin 2\beta_P \sin 2\beta + 0(\epsilon^{*2})\right] \quad [54]$$

Here, the last square bracket is a convergent power series representation of

$$\exp\left\{\frac{\kappa a\epsilon^*}{2R} \sin^2 \gamma \sin 2\beta_P \sin 2\beta\right\}$$

In the Krylov and Bogolinboff averaging procedure, all of the terms involving ϵ^* and its powers in this square bracket will vanish because these terms are odd functions in β, so they can be discarded at once and G can be represented simply as

$$G = \rho(R - a)e^{-(a\epsilon^* \sin^2 \gamma)/2R} (1 - \epsilon \cos \beta) \times \exp\left\{\kappa\epsilon \cos \beta + \frac{\kappa a\epsilon^*}{2R} \sin^2 \gamma \cos 2\beta_P \cos 2\beta\right\} \quad [55]$$

The author is not aware of any result for this expression corresponding to Equation [29] which can be used to repre-

sent the averaged G-functions in terms of tabulated functions of $\kappa\epsilon$ and $\kappa\epsilon^*$. However, the fact that $\epsilon^* \approx 0.0033 \sin^2 \gamma$ implies that, especially for orbits which are not too close to meridian orbits, the expansion

$$e^{\bar{\epsilon} \cos 2\beta} \approx 1 + \bar{\epsilon} \cos 2\beta \dots\dots [56]$$

where

$$\bar{\epsilon} = \frac{\kappa a \epsilon^*}{2R} \sin^2 \gamma \cos 2\beta_P \dots\dots [57]$$

is likely to be a tolerably good representation. Thus, the analogs of Equations [30, 31] are

$$\frac{dR}{d\beta} = \frac{\nu R^2}{a} \rho(R - a) e^{-(a\epsilon^* \sin^2 \gamma)/2R} \times [I_0(\kappa\epsilon) - \epsilon I_1(\kappa\epsilon) + \bar{\epsilon} I_2(\kappa\epsilon)] \dots [58]$$

$$\frac{d\epsilon}{d\beta} = -\frac{\nu R}{a} \rho(R - a) e^{-(a\epsilon^* \sin^2 \gamma)/2R} \times \left\{I_1(\kappa\epsilon) + \epsilon[I_0(\kappa\epsilon) - I_1(\kappa\epsilon)] + \frac{1}{2}\bar{\epsilon} [I_1(\kappa\epsilon) + I_3(\kappa\epsilon)]\right\} \dots [59]$$

Which terms are dominant in Equations [58 and 59] depends on the relative magnitudes of ϵ and $\bar{\epsilon}$. Consider two special cases: $\kappa\epsilon \ll \bar{\epsilon} < 1$ and $\kappa\epsilon \gg \bar{\epsilon}$.

If

$$\frac{d\epsilon}{dR} \approx \frac{\epsilon}{R}\left[1 + \frac{\kappa}{2}\left(1 + \frac{\bar{\epsilon}}{2}\right)\right. \dots\dots [60]$$

whence

$$\frac{\epsilon}{\epsilon_i} = \frac{R}{R_i} \sqrt{\frac{\rho(R_i - a)}{\rho(R - a)}} \exp \left\{\frac{1}{2} a\epsilon^* \sin^2 \gamma \cos 2\beta_P \int_{R_i}^{R} \left(\frac{\rho'}{2\rho}\right)^2 dR\right\} \dots\dots [61]$$

Thus, the result for the spherical earth and small eccentricity is just modified by the exponential function of R which can be evaluated numerically without much difficulty.

The magnitude of the exponential function is generally close to unity, but there is one case in which the change is significant. Consider Equation [61] for values of R extremely close to R_i, so that

$$\frac{\epsilon}{\epsilon_i} \approx 1 - \left[1 + \frac{\alpha a}{2R_i}\left(1 + \frac{\alpha a^2}{4R_i^2} \epsilon^* \sin^2 \gamma \cos 2\beta_P\right)\right] \times \left(\frac{R_i - R}{R_i}\right) \dots\dots [62]$$

Suppose now that

$$\left|\frac{\alpha a^2}{4R_i^2} \epsilon^* \sin^2 \gamma \cos 2\beta_P\right| > 1$$

as it may for lower altitudes (where ρ'/ρ is large) and orbits for which $\sin \gamma$ and $|\cos 2\beta_P|$ are sufficiently close to unity. If the perigee is near the equator (β_P near 0 or π), the coefficient of $(R_i - R)/R$ is positive and the eccentricity decays as altitude decreases. (This is the case in which the perigee occurs in denser regions of the atmosphere, in as much as a fixed R corresponds to lower altitude near the equator.) On the other hand, if the perigee is above 45° N latitude or below 45° S latitude, so that $\cos 2\beta_P < 0$, the coefficient of $(R_i - R)/R_i$ is negative and the eccentricity increases instead of decreases. This is a new qualitative effect which is not obtained when the earth is considered spherical.

If $\bar{\epsilon} \ll \kappa\epsilon$, the dominant terms in Equation [58, 59] are the same as in the case treated earlier in which ellipticity is ignored.

These considerations indicate that as ϵ decreases, the effect of the oblateness of the atmospheric shell increases, but that it does not change the relative values of ϵ much even for small ϵ. However, in some cases an additional eccentricity is induced rather than the eccentricity monotonically decaying with altitude.

Effect of Earth's Rotation

It has been assumed previously that the drag force acts toward the negative velocity vector of the satellite, considered relative to inertial space. Actually, one should consider the velocity relative to the air mass producing the drag. If the atmosphere at satellite altitude partakes of the earth's rotation, another component of drag force exists normal to the plane of the orbit.

Relative to a rotating atmosphere, the component of drag in the plane of the orbit can be treated exactly as in the second section, except that the force has a small oscillatory component as the satellite traverses its orbit. For $\gamma < \pi/2$, the force is slightly less at the extreme excursions of latitude than near the equator, for the relative velocity component in the plane of the orbit is slightly smaller at these points. Conversely, for $\gamma > \pi/2$, the drag force is slightly greater at the extreme latitudes.

A similar oscillatory force exists because of the ellipticity of the atmospheric shell, as discussed in the previous section. Over an oblate earth, the density at a constant radial distance is less at high latitudes than near the equator. It follows that the effect in the orbital plane of the earth's rotation may be analyzed in a manner very similar to the analysis of the earth's oblateness effect. Moreover, for retrograde orbits these effects tend to compensate. The effect of a rotating atmosphere can be expected to be small, for the maximum difference between relative and absolute velocities is only about 5 per cent of the absolute velocity if the atmospheric shell rotates as a rigid body with the angular speed of the earth. This almost certainly is not the case, and the atmosphere at altitudes of interest is likely to have a much lower velocity than the earth's surface.

The component of drag force normal to the plane of the orbit is another matter. It cannot be treated within the analytical framework of this paper: One must return to a complete set of equations of motion in which the possibility of motion out of the plane of the orbit is admitted. Although the analysis of this "cross-drag" has not been attempted, it is expected that this effect will result in some rotation of the plane of the orbit and that it may have some influence on the orbital inclination. However, it is conjectured that any such effect is likely to be small enough to ignore in most applications.

References

1 Kallman, H. K., "Physical Properties of the Upper Atmosphere," Report RM-841, The Rand Corp., Santa Monica, Calif., May 1952.

2 Krylov, N. M., and Bogoliuboff, N., "Introduction to Nonlinear Mechanics," Princeton University Press, Princeton, N. J., 1943.

3 Minorsky, N., "Nonlinear Mechanics," J. W. Edwards, Ann Arbor, 1947.

4 Petersen, N. V., "Lifetimes of Satellites in Near-Circular and Elliptic Orbits," Jet Propulsion, vol. 26, 1956.

5 Watson, G. N., "Bessel Functions," Cambridge University Press, revised edition, 1944.

An Experimental Investigation of The Flow Over Simple Two-Dimensional and Axial Symmetric Bodies at Hypersonic Speeds[1]

I. E. VAS,[2] S. M. BOGDONOFF[3] and A. G. HAMMITT[4]

Gas Dynamics Laboratory, Forrestal Research Center, Princeton University, Princeton, N. J.

A study of the inviscid shock shape and pressure distribution about thick two-dimensional and axial symmetric bodies was conducted in the Princeton University Helium Hypersonic Tunnel. Details were obtained for flat and semicircular leading edges for Mach numbers between 11 and 19. From the Schlieren pictures, the shock shape, detachment distance and sonic point on the shock were found. Similar pressure distributions were obtained for corresponding two-dimensional and axial symmetric bodies.

Nomenclature

a, b = defined by $y/t = a(x/t)^b$

C_p = $\dfrac{p - p_1}{\dfrac{\gamma}{2} p_1 M_1^2}$

$C_{p_{max}}$ = $\dfrac{p_2 - p_1}{\dfrac{\gamma}{2} p_1 M_1^2}$

d = cylinder leading edge thickness, inches

k = density ratio across a normal shock

M = Mach number

p = static pressure, psia

R = radius of curvature

Re = Reynolds number

s = surface distance measured from the center line stagnation point on the body

t = plate leading edge thickness, inches

x, y = shock coordinates measured from the shock apex, inches

γ = ratio of specific heats

δ = detachment distance, inches

Δp = $p - p_1$

θ_b = angle between the tangent to the body surface and the free stream direction

ρ = density

Subscripts

0 = stagnation conditions

1 = free stream conditions

b = body

s = shock

t = leading edge thickness (applied to Reynolds number)

T = conditions behind a normal shock

Introduction

At high Mach numbers, dissociation and ionization of the air may have a considerable effect upon the aerodynamic characteristics of a body. As aerodynamic heating may cause serious problems at these speeds, the removal of heat near the front of the body must be considered. For this purpose, a blunt body would present certain aerodynamic advantages. The study of the conditions on this body at simulated flight conditions at these Mach numbers would be extremely difficult. However, the perfect gas aerodynamics of such bodies may be investigated as part of the over-all problem. Helium is the ideal gas to be used as its liquefaction temperature is about $2\frac{1}{2}$ R at 0.0015 atm and its specific heat is approximately constant over a wide range of pressures and temperatures.

Newton has postulated that when discrete particles strike a surface the normal momentum component is eliminated and the tangential momentum component remains unchanged. The loss in the normal momentum causes an increase in the pressure. The value of the pressure coefficient predicted is

$$C_p = 2 \sin^2 \theta_b$$

where θ_b is the angle between the free stream flow direction and the body surface. This analysis holds only for $\gamma \rightarrow 1$ and $M \rightarrow \infty$ for which case the shock lies on the body surface. For $\gamma \rightarrow 1$ and $M \rightarrow \infty$ the pressure coefficient at the stagnation point, $C_{p_{max}}$, is equal to 2. For $\gamma = 5/3$ and $M = 15$ the maximum pressure coefficient is 1.75. By accounting for the strong leading edge shock, one has

$$\frac{C_p}{C_{p_{max}}} = \sin^2 \theta_b$$

which can be used to predict the pressures on blunt bodies (1–4).[5] For blunt leading edges, the inviscid pressure on a surface parallel to the free stream has been predicted in (5–7) for two-dimensional and axial symmetric bodies. There seems to be some discrepancy between the values obtained from experiment and the predicted values.

The shape of the shock, distance of the shock from the stagnation point and the sonic point on the shock have also received considerable attention (8–15). Reasonable agreement is obtained between the predicted values of the detachment distance between theory and experiment (16–19). Several experimental investigations have been made to determine the pressure distribution on hemisphere cylinders at supersonic speeds and low hypersonic speeds (2, 3, 4, 20). No experimental data are available of the pressures on the surface parallel to the free stream direction of a blunt flat plate or cylinder with the leading edge perpendicular to the free stream direction. There also seems to be a lack of such information for the case of the flat plate with a hemicylindrical leading edge at hypersonic speeds, although some data (18) are presented for this type leading edge at a Mach number of [illegible]9.

Received June 20, 1957.

[1] The present study is part of a program of research on hypersonic flow under Contract No. AF33 (616)-2547 to Wright Air Development Center, U. S. Air Force.

[2] Research Associate.

[3] Professor; Head, Gas Dynamics Laboratory.

[4] Senior Research Associate.

[5] Numbers in parentheses indicate References at end of paper.

In some previous work performed at the Gas Dynamics Laboratory of Princeton University (21–23), the flow about flat plates was studied with the leading edge thickness varying from 0.13×10^{-3} in. to 44×10^{-3} in.; however, no details were sought near the leading edge. It is the purpose of the present paper to obtain the details near the leading edge of both two-dimensional and axial symmetric blunt bodies with square and rounded leading edges. The shape of the shock about the body, detachment distance, and sonic point are measured and compared to predicted values. The pressure distributions on these representative models are also presented.

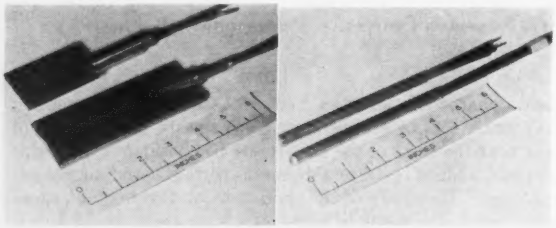

Fig. 1 The pressure models

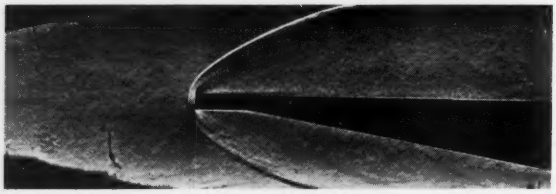

(a) Flat leading edge plate, $M = 13.7$

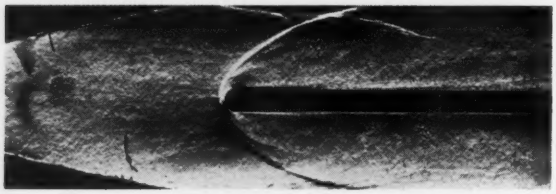

(b) Hemicylindrical leading edge plate, $M = 13.8$

(c) Flat leading edge cylinder, $M = 14.5$

(d) Hemisphere leading edge cylinder, $M = 12.7$

Fig. 2 Schlieren photographs of the bodies

Experimental Facilities

The experimental work was carried out in the Princeton University Helium Hypersonic Tunnel. The details of the tunnel have been given previously (24), so only a résumé shall be presented here. An axially symmetric nozzle with an initial taper of $5\frac{1}{2}$ deg, joined to a $3\frac{1}{4}$-in.-diam cylindrical section was used. The sides of the nozzle were milled parallel to each other and windows installed. Disturbances caused by the window-nozzle junction do not affect the flow in the test region of the tunnel, as the wave angle formed at these high Mach numbers is small. By changing the throat diameter, it was possible to change the Mach number. The Mach number range was 11 to 19 with stagnation pressures from 700 to 1500 psia. Because of the conical design, a Mach number gradient existed along the center line of the nozzle. With the larger throat diameter, the Mach number range was 11 to 14 with a gradient of 0.5 Mach number per inch; and with the smaller throat diameter, the Mach number varied from 16 to 19, with a gradient of 0.7 Mach number per inch. An attempt to correct for the pressure gradient in the tunnel was made and is explained later.

Test Program

General

A test program was set up to study in some detail the flow about thick two-dimensional and axial symmetric bodies with square and round leading edges. A single representative model was used for each case with pressure orifices located on the face and on the surface parallel to the free stream. The models are shown in Fig. 1. Several dummy models were employed in the shock shape study for the determination of the detachment distance and sonic point on the shock. Schlieren photographs and static pressure distributions were obtained at Mach numbers between 11 and 19 at stagnation pressures between 700 and 1500 psia.

Shock Shape Studies

Schlieren photographs were obtained for thick two-dimensional and axial symmetric bodies. For the flat plates, the leading edge thickness varied from 0.043 to 0.200 in. and for the axially symmetric bodies, from 0.063 to 0.5 in. A set of Schlieren photographs for the bodies is shown in Fig. 2. No boundary layer is noticed on either the two-dimensional or axial symmetric bodies. On thin flat plates ($Re_t < 4000$) the edge of the boundary layer was well defined (21 and 22). From the photographs, the position of the shock with reference to the body center line was measured on an optical comparator. The distance of the shock from the body on the body center line and the sonic point on the shock were also measured on the comparator. In the study of the shape of the shock about a flat plate with a square leading edge (21, 22) it was shown that the shape depended on both the geometric inviscid parameter x/t and on the viscous parameter (leading edge Reynolds number) Re_t for small values of Re_t, but only upon the geometric inviscid parameter for $Re_t > 4000$. The leading edge Reynolds numbers for the present tests are about ten to fifty times larger than the above value.

When the shock coordinates are nondimensionalized by the leading edge thickness and plotted on log-log paper, a straight line results. For the same body shape, the shock is independent of the leading edge thickness and Mach number. As this is true, only a representative shock shape is shown in Fig. 3 for the four body configurations at a Mach number about 13. As these shocks form approximately straight lines on this plot, an equation of the form

$$\frac{y}{t} = a\left(\frac{x}{t}\right)^b$$

may be fitted to them. The values of a and b remain ap-

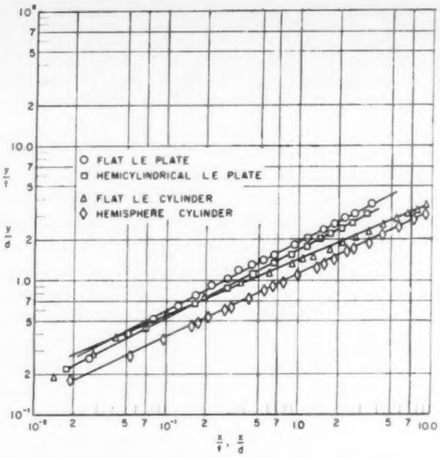

Fig. 3 Shock shape of the four configurations

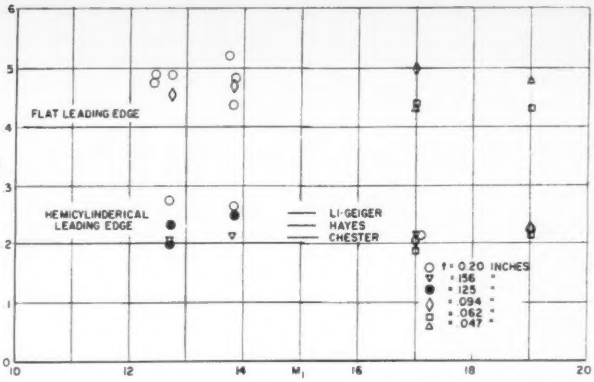

Fig. 4 (a) Detachment distance for the plate vs. M_1

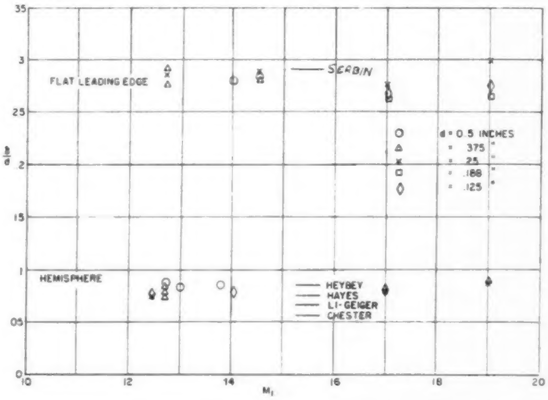

Fig. 4 (b) Detachment distance for the cylinder vs. M_1

proximately constant for the entire range of Mach number and leading edge thickness. There is no effect of the leading edge Reynolds number on the shape of the shock. The shock shape obtained from the Schlieren photographs for the four configurations may be written as

$$\frac{y}{t} = 2.0\left(\frac{x}{t}\right)^{0.49} \quad \text{(for a flat plate with a square leading edge)}$$

$$\frac{y}{t} = 1.75\left(\frac{x}{t}\right)^{0.50} \quad \text{(for a flat plate with a round leading edge)}$$

$$\frac{y}{d} = 1.4\left(\frac{x}{d}\right)^{0.42} \quad \text{(for a cylinder with square leading edges)}$$

$$\frac{y}{d} = 1.1\left(\frac{x}{d}\right)^{0.45} \quad \text{(for a hemisphere cylinder)}$$

As y/t depended only upon x/t for all values of Re_t, the viscous parameter did not enter into the relation, so one might assume that the phenomenon was primarily inviscid.

The detachment distance δ was measured from the Schlieren photographs for all bodies except the smaller ones. As this distance decreases, the inaccuracy of the measurements increases. In Fig. 4, the detachment distance nondimensionalized by the leading edge thickness is shown as a function of the free stream Mach number. There is a certain amount of scatter in the points, but the average values are as follows for $12 < M_1 < 19$

$\delta/t = 0.48$ (for the flat leading edge plate)
$\delta/t = 0.24$ (for the round leading edge plate)
$\delta/d = 0.28$ (for the flat leading edge cylinder)
$\delta/d = 0.08$ (for the hemisphere cylinder)

The sonic point on the shock was also obtained from the shock shape. In Fig. 5 the shock is sketched about the body for the four configurations. The sonic point and distance between the shock and body are illustrated.

Pressure Distribution Studies

Pressure distribution studies were made on a representative model for each of the configurations. The shock shapes found previously indicated that, for all the leading edges measured, the shape of the shock depended entirely upon the geometry. The pressures were obtained on one of the larger models used previously in the shock shape studies. Detail pressure distributions were made with each of the configurations at Mach numbers between 11 and 14, and at a stagnation pressure of 1000 psia. Pressures on the hemisphere cylinder were obtained to Mach 19 at a stagnation pressure of 1500 psia.

Due to the gradient in the tunnel, the static and total pressures are not constant along the tunnel center line. In an attempt to minimize the discrepancy that might be caused by this change in Mach number compared to a constant Mach number test, the static pressure p_1 and total pressure p_T are assumed to be variables in the pressure coefficient ratio $C_p/C_{p\max}$. This ratio is plotted against the distance parameter s/t where s is the surface distance measured from the midpoint of the body leading edge. The pressure coefficient, C_p, is the difference between the measured pressure, p, and the static pressure p_1 (which would have existed at that point if no model were present), divided by the dynamic pressure; $C_{p\max}$ is the difference between the free stream total head pressure p_T, and p_1, divided by the dynamic pressure. For each configuration, two plots are made of $c_p/c_{p\max}$, one near the leading edge where the pressure coefficient ratio is close to unity, and one on the afterbody, where the pressure coefficient approaches zero. On the latter plot, the approximate value of zero pressure in the tunnel is indicated. By this means, the details of the measured pressures near the leading edge and after the shoulder can be observed clearly. In Fig. 6 the pressure distributions are shown for the four configurations at the various Mach numbers. In Fig. 6 (d) separation on the rear part of the plate at $M_1 = 13.9$ causes the pressure coefficient to increase.

Discussion

Shock Shapes—Flat Plates

In some previous work (21 and 22), interferograms were obtained of the flow about a plate with a flat leading edge varying

in thickness from 0.17×10^{-3} to 59.5×10^{-3} in. From the interferograms of the thicker plates, a low pressure region was indicated immediately behind the corner From the Schlieren photograph of the two-dimensional bodies, Figs. 2(a), 2(b), it is possible to locate the shock clearly. The dark region at the corner of the plate is due to optical distortion through the high gradients that exist at that point. No details of the boundary layer on the plate are visible because of the low density region that exists near the surface of the plate.

Several analytical investigations have been made in an attempt to determine the shock shape, detachment distance and sonic point on the shock for a body with a round leading edge.[6] In the analysis of Hayes (10), the shock layer is assumed to be thin, so the radius of curvature of the shock is approximately that of the body. Between the shock and the body, incompressible, constant density flow is assumed. Expressions have been obtained for the detachment distance for a plate with a hemicylindrical leading edge. Another solution has been obtained for the detachment distance (13) which is similar to that of Hayes. The shock is assumed to be parabolic and compressibility has been included in the calculations. Chester has determined the flow characteristics assuming a parabolic shock and calculated a body shape which is "nearly parabolic" (11). An exact solution is reached for $\gamma \rightarrow 1$ and $M \rightarrow \infty$ followed by a perturbation in $(\gamma - 1)/(\gamma + 1)$ and M^{-2}.

From the present series of tests of a plate with a flat leading edge, the shock can be approximated by a parabola of the form

$$\left(\frac{y}{t}\right)^2 = 4.4\left(\frac{x}{t}\right)$$

For helium, ($\gamma = 5/3$) at a Mach number of about 15, the angle that the shock makes with the free stream for sonic flow behind the shock is $63\frac{1}{4}$ deg. The sonic point on the shock is at $y/t = 0.97$ and lies above the body sonic point. The detachment distance is about 0.48. A sketch of body and shock showing the sonic point and detachment distance is shown in Fig. 5 (a).

A parabolic shock is also formed around a blunt two-dimensional body with a rounded leading edge The shock shape is of the form

$$\left(\frac{y}{t}\right)^2 = 3.06\left(\frac{x}{t}\right)$$

The radius of curvature of the shock is 3.06 times that of the body or $R_s/t = 1.53$ and the detachment distance $\delta/t = 0.24$. The sonic point is at $y/t = 0.66$.

The detachment distance as predicted in (10) for a hemicylindrical plate is

$$\delta = \frac{kR}{\sqrt{1 - 2k}} \sinh^{-1} \sqrt{\frac{1 - 2k}{2k}}$$

where k is the density ratio across the normal shock. In this reference, it is suggested that the radius of curvature of the shock R_s be used instead of the radius of curvature of the body R.

$$R_s = R + \delta$$

By this method, $\delta/t = 0.23$. If, however, R_s is obtained from the shock itself defined by the above equation, then the detachment distance is about $0.48t$. In (11) the radius of curvature of the shock on the axis of symmetry was calculated to be twice that of the body curvature. This value is less than the present one. The detachment distance predicted by this method is $0.21t$ which is reasonably close to the value of about $0.24t$ obtained experimentally. From (11) the sonic point on the shock is at $y/R_s = 0.5$ or $y/t = 0.5$ as the radius of curvature of the shock is twice that of the body. The sonic point on the shock is calculated to be outboard of the sonic point on the body. This value is again less than the experimental value, but has the same tendency. In Fig. 5 (b), the shock form, detachment distance and sonic point are noted.

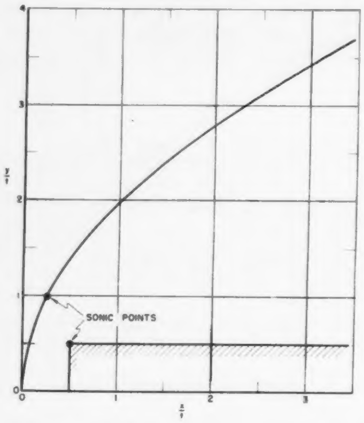

Fig. 5 (a) Shock about the flat leading edge plate

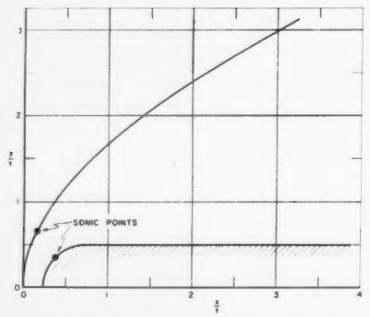

Fig. 5 (b) Shock about the hemicylindrical leading edge plate

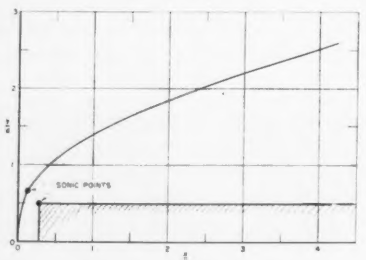

Fig. 5 (c) Shock about the flat leading edge cylinder

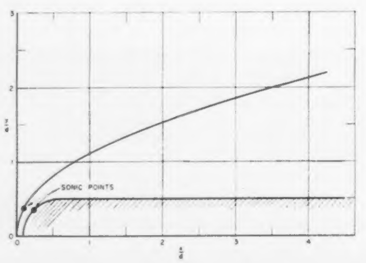

Fig. 5 (d) Shock about the hemisphere cylinder

[6] For blunt two-dimensional bodies a solution for the detachment distance and the y coordinate of the shock sonic point has been obtained (9). It is assumed that the shock is hyperbolic and asymptotic to the free stream Mach lines, and that the shock location is determined by continuity.

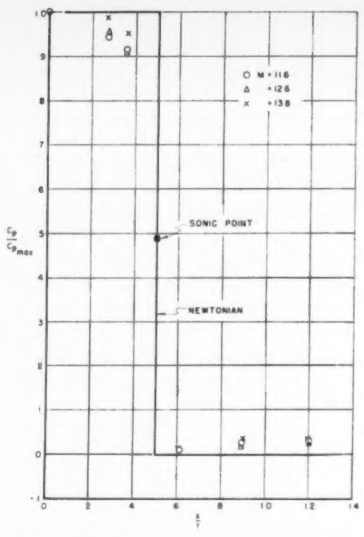

Fig. 6 (a) **Pressure coefficient on the face of the flat leading edge plate**

Shock Shapes—Axial Symmetric

The shock for the flat leading edge cylinder can be approximated by the curve

$$\left(\frac{y}{d}\right)^{2.4} = 2.23\left(\frac{x}{d}\right)$$

This equation holds for the measurements made to determine the shock shape for $x/d > 0$. If the radius of curvature were calculated using this equation, the value at the x-axis would be infinity. The sonic point is located at $y/d = 0.67$ and the detachment distance is at $\delta/d = 0.28$. A sketch of the shock with the detachment distance and sonic point is shown in Fig. 5 (c). The sonic point on the shock is outboard of the body sonic point.[7]

A considerable amount of experimental data is available on hemisphere cylinders or spheres at lower Mach numbers (3, 16 and 17). Reasonable correlations have been made with air ($\gamma = 1.4$) and argon ($\gamma = 1.67$) with some of the theories. For the present sets of tests, the shock may be defined as

$$\left(\frac{y}{d}\right)^{2.22} = 1.25\left(\frac{x}{d}\right)$$

Again, the radius of curvature of the shock on the axis of symmetry is infinity. In an attempt to determine the radius of curvature, an equation of the form

$$\frac{x}{d} = A_1\left(\frac{y}{d}\right)^2 + A_2\left(\frac{y}{d}\right)^4 + A_3\left(\frac{y}{d}\right)^6 \ldots$$

was assumed and the coefficients evaluated. Using two terms

$$\frac{x}{d} = 0.709\left(\frac{y}{d}\right)^2 + 0.106\left(\frac{y}{d}\right)^4$$

and with three terms

$$\frac{x}{d} = 0.697\left(\frac{y}{d}\right)^2 + 0.175\left(\frac{y}{d}\right)^4 - 0.074\left(\frac{y}{d}\right)^6$$

Omitting the higher order terms, this equation can be re-

[7] For a flat faced cylinder, Serbin (14) obtained a value for the detachment distance of 0.29d which is nearly equal to the experimentally determined value. The detachment distance predicted by Hayes is approximately twice the measured value.

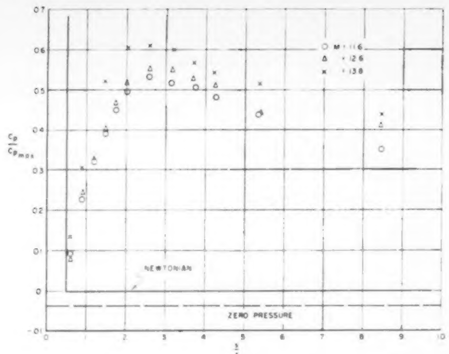

Fig. 6 (b) **Pressure coefficient on the surface of the flat leading edge plate parallel to the free stream direction**

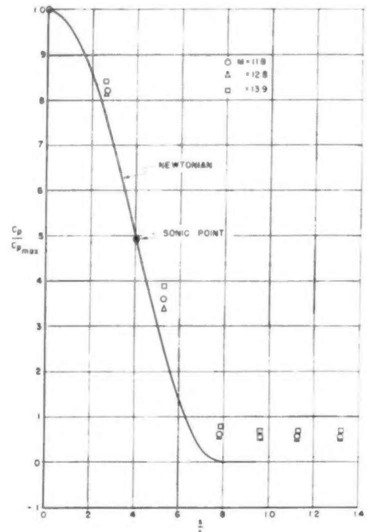

Fig. 6 (c) **Pressure coefficient on the hemicylindrical section of the plate**

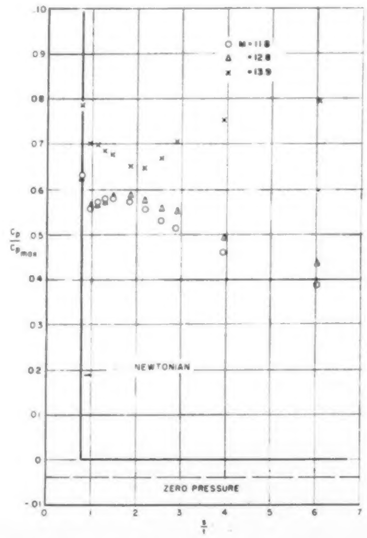

Fig. 6 (d) **Pressure coefficient on the surface of the hemicylindrical leading edge plate parallel to the free stream direction**

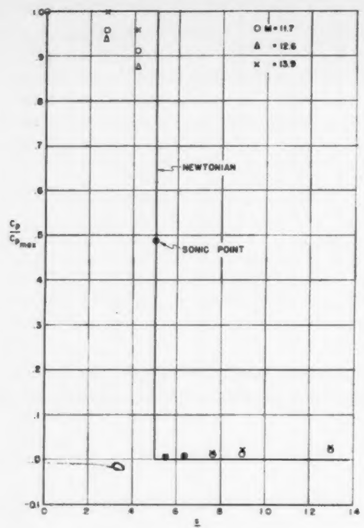

Fig. 6 (e) Pressure coefficient on the face of the flat leading edge cylinder

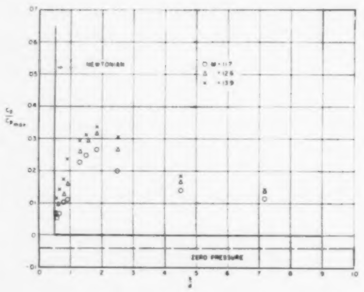

Fig. 6 (f) Pressure coefficient on the surface of the flat leading edge cylinder parallel to the free stream direction

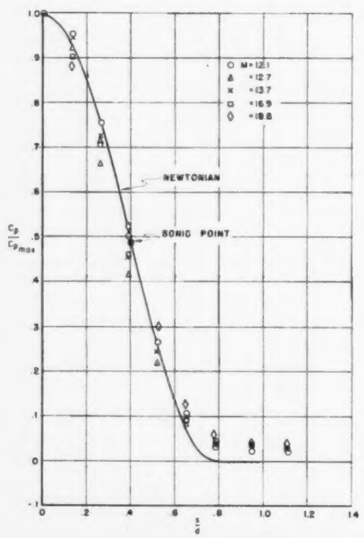

Fig. 6 (g) Pressure coefficient on the hemisphere section of the cylinder

written in the form

$$\left(\frac{y}{d}\right)^2 = 1.435\left(\frac{x}{d}\right)$$

The radius of curvature of the shock on axis is about 1.4 times that of the body.

The detachment distance was equal to $0.08d$ and the sonic point located at $y/d = 0.37$. It is noticed that the radius of curvature of the shock is approximately equal to the radius of curvature of the body plus the detachment distance. Several of the theories give values for the detachment distance with reasonable accuracy as are shown in Fig. 4. In (12), the detachment distance was calculated to be 0.067 times the radius of curvature of the body and the radius of curvature of the shock about 1.25 times that of the body. It should be pointed out that many of the theories predict the value of the detachment distance for $\gamma \rightarrow 1$ and $k \rightarrow 0$. In helium the value of γ is large compared to unity and k is large compared to zero. The results obtained from the theories can only give an indication as to the magnitude of this distance.

It has been suggested (9) that the characteristic features of the flow in the subsonic region behind the strong shock are dependent upon the choking phenomenon that occurs at the minimum area between the body sonic point and shock. A relationship has also been shown to exist between the sonic point on the shock and body sonic point, and that any changes in the body ahead of the body sonic point would have negligible effect on the shock sonic point. For the two-dimensional bodies, the ratio of the y-coordinate of the shock sonic point to the y-coordinate of the body sonic point is about constant, but this is not true for the case of the axially symmetric bodies. The value of the detachment distance calculated by this method is about a third higher than the measured values.

Pressure Distribution Study

It has been shown experimentally that the pressure on a plate with a flat leading edge depends mainly on the leading edge Reynolds number Re_t for thin leading edges or on the geometric parameter s/t for thick leading edges with the inviscid effects predominating for $Re_t > 4000$ (21 to 23). Detailed pressures were obtained for $s/t > 5$ for a plate with a flat leading edge. In the present tests, pressure distributions are presented for $s/t < 10$ for the inviscid model.

On the face of the plate with the flat leading edge the pressure has a maximum value in the center of the plate and decreases as the corner is approached. The pressure at the sonic point is about one half the total pressure behind the normal shock and is noted on the pressure curves. The pressure measured at the nearest point behind the corner drops to within 10 per cent of the static pressure in the tunnel and then increases to about $C_p/C_{p_{\max}} = 0.06$, at $s/t = 2\frac{1}{2}$. The pressure continuously decreases for $s/t > 2\frac{1}{2}$. The pressure coefficient

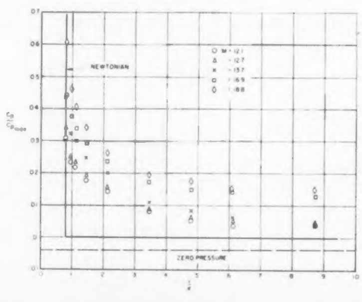

Fig. 6 (h) Pressure coefficient on the surface of the hemisphere leading edge cylinder parallel to the leading edge

increases with Mach number on the plate surface parallel to the free stream though there is no consistent variation of this on the plate face which is normal to the flow direction. It has been shown that for $\gamma = 5/3$, a 90 deg expansion increases the Mach number to infinity with the pressure going to zero (22). The expansion waves around the corner strike the sonic line and return as compressions resulting in the pressure rise after the corner. The remaining part of the expansion fan hits the shock and returns as expansion waves causing the decrease in the pressure on the plate.

For the case of a plate with a hemicylindrical leading edge, the pressures on the cylindrical section are reasonably well predicted by the Newtonian approximation corrected for shock losses. However, near the junction of the cylinder section with the flat section, measured pressures are considerably higher than the predicted ones. For $\theta_b = 0$, (the plate parallel to the initial flow direction), the predicted value of the pressure coefficient is zero.

From the previous work it was shown that the viscous effects are unimportant for $Re_t > 4000$. The pressures on the plate with the flat leading edge were obtained from two models with leading edge Reynolds numbers 37×10^3 ($t = 0.0438$ in.) and 105×10^3 ($t = 0.124$ in.). For the hemicylindrical leading edges, the leading edge Reynolds numbers were 37×10^3 ($t = 0.0438$ in.) and 170×10^3 ($t = 0.20$ in.). Good agreement is obtained between the same type model for the variations of Re_t. These pressures, made at a Mach number of 12.7, are presented as the incremental pressure ratio $\Delta p/p_1$ (Fig. 7). On this plot, the pressure decays as the -0.5 power of s/t. The measured pressures for the two different leading edges are approximately equal for $s/t > 3$.

Several experimental investigations have been made on axially symmetric bodies with round and square leading edges at various Mach numbers (2, 3, and 4). For the square leading edges, Oliver has shown that at $M = 5.8$ in air, the pressure on the face is relatively constant and starts to drop off at about $0.35\, s/d$. No pressure measurements were made after the corner. The pressure after the shoulder on a flat leading edged cylinder behaves in a manner similar to the flat leading edge plate. The expansion followed by compression waves returning from the sonic line and expansion waves from the shock wave cause the low pressure immediately after the corner, the increase in pressure and final pressure decay. The pressure coefficient has a maximum value of about 0.3 at $s/d = 2$.

For the hemisphere cylinder, it has been shown that the pressure on the curved section is well predicted by the Newtonian pressures for Mach numbers between 2.0 and 6.8 in air. The pressures obtained in helium for Mach numbers between 11 and 19 on the hemisphere section can also be predicted reasonably well by the Newtonian approximation, but the measured pressures diverge from the predicted ones near the junction of the hemisphere with the cylinder. The pressures on the cylindrical section approached the ambient pressure but were always greater than it. On the cylindrical section, the pressure coefficient increases with Mach number though there is no consistent variation of pressure coefficient with Mach number on the spherical portion of the body. The pressures on the cylindrical section of the hemisphere cylinder are lower than those on the flat leading edged cylinder for $s/d > 1$.

On the surface parallel to the free stream, the pressures on the axial symmetric bodies are less than those on the two-dimensional bodies for both the flat and rounded leading edges. For the flat leading edge, the peak value of the pressure coefficient for the plate is twice that measured on the cylinder. For the round leading edges, the pressures on the plate after the junction were about two to three times those on the cylinder for the same vales of s/t.

Conclusions

1 A parabolic shock is formed about plates with flat and hemicylindrical leading edges for $x/t < 10$. For cylindrical bodies, a "nearly" parabolic shock is formed for $x/d < 10$.

2 The value of the detachment distance for the two-dimensional and axial symmetric bodies with a rounded leading edge is within the order of magnitude of the predicted values.

3 The sonic point on the shock depends both upon the body sonic point and body shape ahead of the sonic point.

4 On the body surface parallel to the free stream direction, an increase in Mach number causes an increase in the pressure coefficient ratio for both two-dimensional and axial symmetric bodies.

5 For the same type of leading edge, the pressure coefficient ratio on the surface parallel to the flow direction is higher for a two-dimensional body than for an axial symmetric body.

6 On the flat and hemicylindrical plates at the same free stream Mach number, the pressure coefficient ratios are equal for $s/t > 2\frac{1}{2}$.

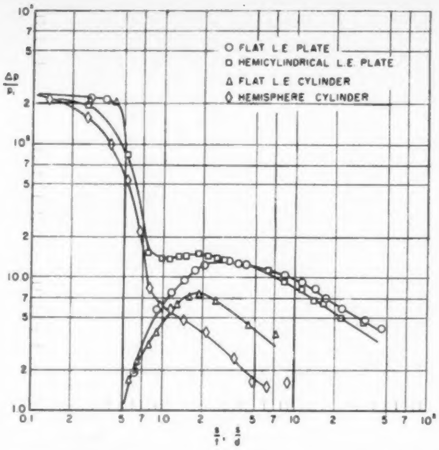

Fig. 7 Incremental pressure ratio vs. dimensionless distance for the four configurations at $M = 12.7$

References

1 Lees, L., "Hypersonic Flow," IAS Preprint 554, June 1955.

2 Oliver, R. E., "An Experimental Investigation of Flow Over Simple Blunt Bodies at a Nominal Mach Number of 5.8," GALCIT Memorandum 26, June 1, 1955.

3 Stine, H., and Wanlass, K., "Theoretical and Experimental Investigation of Aerodynamic-Heating and Isothermal Heat-Transfer Parameters on a Hemispherical Nose With Laminar Boundary Layer at Supersonic Mach Numbers," NACA TN 3344, Dec. 1954.

4 Crawford, D., and McCauley, W., "Investigation of the Laminar Aerodynamic Heat-Transfer Characteristics of a Hemisphere-Cylinder in the Langley 11-inch Hypersonic Tunnel at a Mach Number of 6.8," NACA TN 3706, July 1956.

5 Sakurai, A., "On the Propagation and Structure of the Blast Wave 1," *Journal of the Physical Society of Japan*, vol. 8, no. 5, Oct. 1953.

6 Cheng, H., and Pallone, A., "Inviscid Leading Edge Effect in Hypersonic Flow," *Journal of the Aeronautical Sciences*, vol. 23, no. 7, July 1956.

7 Lees, L., and Kubota, T., "Inviscid Hypersonic Flow Over Blunt Nosed Slender Bodies," *Journal of the Aeronautical Sciences*, vol. 24, no. 3, March 1957.

8 Maslen, S., and Moekel, W., "Inviscid Hypersonic Flow Past Blunt Bodies," IAS Preprint 665, Jan. 1957.

9 Moeckel, W., "An Approximate Method for Predicting Form and Location of Detached Shock Waves Ahead of Plane or Axially Symmetric Bodies," NACA TN 1921, July 1949.

10 Hayes, W., "Some Aspects of Hypersonic Flow," The Ramo-Wooldridge Corp., Jan. 4, 1955.

11 Chester, W., "Supersonic Flow Past a Bluff Body with a

Detached Shock. Part 1: Two-Dimensional Body," *Journal of Fluid Mechanics*, vol. 1, part IV, Oct. 1956.

12 Chester, W., "Supersonic Flow Past a Bluff Body with a Detached Shock. Part II: Axisymmetrical Body," *Journal of Fluid Mechanics*, vol. 1, part V, Nov. 1956.

13 Li, T., and Gerger, R., "Stagnation Point of a Blunt Body in Hypersonic Flow," *Journal of the Aeronautical Sciences*, vol. 24, no. 1, Jan. 1957.

14 Serbin, H., "Hypersonic, Non-Viscous Flow Around a Circular Disc Normal to the Stream," Project Rand Research Memorandum RM 1713, May 1956.

15 Serbin, H., "Hypersonic Non-Viscous Flow Around a Sphere," Project Rand Research Memorandum RM 1772, August 1956.

16 Heybey, W., "Shock Distances in Front of Symmetrical Bodies," NAVORD Report 3594, Dec. 1953.

17 Schwartz, R., and Eckerman, J., "Shock Location in Front of a Sphere as a Measure of Real Gas Effects," NAVORD Report 3904, Feb. 1955.

18 Moeckel, W., "Experimental Investigation of Supersonic Flow With Detached Shock Waves for Mach Numbers Between 1.8 and 2.9," NACA RME 50D05, July 1950.

19 Kim, C., "Experimental Studies of Supersonic Flow Past a Circular Cylinder," *Journal of the Physical Society of Japan*, vol. 11, no. 4, April 1956.

20 Machell, R., and O'Bryand, W., "An Experimental Investigation of the Flow Over Blunt-Nosed Cones at a Mach Number of 5.8," GALCIT Hypersonic Research Project Memorandum 32, June 1956.

21 Hammitt, A. G., Vas, I. E., and Bogdonoff, S. M., "Leading Edge Effects on the Flow Over a Flat Plate at Hypersonic Speeds," Princeton University Aeronautical Engineering Report 326, Sept. 1955. (Also published as WADC TN 55-537.)

22 Hammitt, A. G., and Bogdonoff, S. M., "Hypersonic Studies of the Leading Edge Effect on the Flow Over a Flat Plate," JET PROPULSION, vol. 26, no. 4, April 1956.

23 Vas, I.E., "An Experimental Investigation of the Pressure on a Thin Flat Plate at Hypersonic Speeds," Princeton University Aeronautical Engineering Report 377, March 1957. (Also published as WADC TN 57-104.)

24 Bogdonoff, S. M., and Hammitt, A. G., "The Princeton Helium Hypersonic Tunnel and Preliminary Results above M = 11," Princeton University Aeronautical Engineering Report 260, June 1954. (Also published as WADC TN 54-124.)

Analysis of Regenerative Cooling in Rocket Thrust Chambers

LEO E. DEAN[1] and LUCIAN A. SHURLEY[1]

Aerojet-General Corp., Sacramento, Calif.

In order to obtain a realistic value of heat flux and temperature distribution within the walls of a rocket thrust chamber recourse must be taken to experimental and empirical techniques. This paper discusses the experimentally determined heat transfer data obtained on JP-4 and RFNA under conditions simulating those occurring during thrust chamber operation. An electrical analogy technique is used to determine the temperature and heat flux distribution because of the irregular shape of the coolant passages. Using the experimental data for film coefficients and a two-dimensional electrical analog, the heat flux and temperature distribution within the walls of a tubular chamber cooled with JP-4 and within the walls of a drilled passage thrust chamber cooled with RFNA are obtained.

Nomenclature

G	= mass velocity, lb/in.²-sec
h_f	= heat transfer coefficient
K_m	= metal thermal conductivity
L_f	= length of paper representing h_f
L_f'	= length of contoured paper representing h_f
L_{f_g}	= length of paper representing gas film
L'_{f_l}	= length of contoured paper representing liquid film
Nu	= Nusselt number
p	= perimeter of section for which the heat flux is calculated
P	= absolute pressure, psia
Pr	= Prandtl number
Q/A	= heat flux, Btu/in.²-sec
$(Q/A)_{conv}$	= predicted heat flux for convection at the same wall and bulk temperature that exists at $(Q/A)_{ul}$
$(Q/A)_{ul}$	= heat flux at the upper limit of nucleate boiling
r	= radius of curvature
Re	= Reynolds number
R_p	= paper ratio = $\dfrac{\text{resistance}/\square\text{of paper representing } h_f}{\text{resistance}/\square\text{of paper representing metal}}$
S	= scale factor size of model/size of prototype
ΔT	= temperature difference

Introduction

THE problems of high coolant velocity, boiling, deposition of carbon and other impurities, high temperature and velocity of combustion gases, and odd geometry make a precise analytical treatment of heat transfer in regeneratively cooled rocket engines very difficult or impossible. Therefore, in order to obtain realistic values of heat flux and temperature distribution within the walls of a rocket thrust chamber recourse must be taken to experimental and empirical techniques.

Rocket thrust chambers designed for long duration firings must be cooled to protect the walls from the high temperature, high velocity combustion gases. This is usually accomplished by passing one of the propellants through coolant passages located within the walls of the thrust chamber. At the high heat fluxes and temperatures encountered in rocket thrust chambers the propellants may become corrosive, decompose, or deposit impurities on the heating surface, thereby reducing their cooling effectiveness. It is impossible to predict, with any degree of certainty, the propellant heat transfer characteristics under these conditions. To properly analyze the heat transfer conditions in this region of high heat flux and temperature, it is necessary to base the analysis upon experimentally determined heat transfer data.

The use of one-dimensional heat conduction equations will give erroneous results when applied to the irregular geometric configurations which are sometimes encountered in thrust chamber designs. The method proposed to solve the two-dimensional heat transfer conduction problems involved (1)[2] is an electrical analogy technique.

By making use of the experimentally determined liquid film heat transfer coefficients and the electrical analogy method

Presented at the ARS Semi-Annual Meeting, San Francisco, Calif., June 10–13, 1957.

[1] Development Engineer, Liquid Rocket Plant.

[2] Numbers in parentheses indicate References at end of paper.

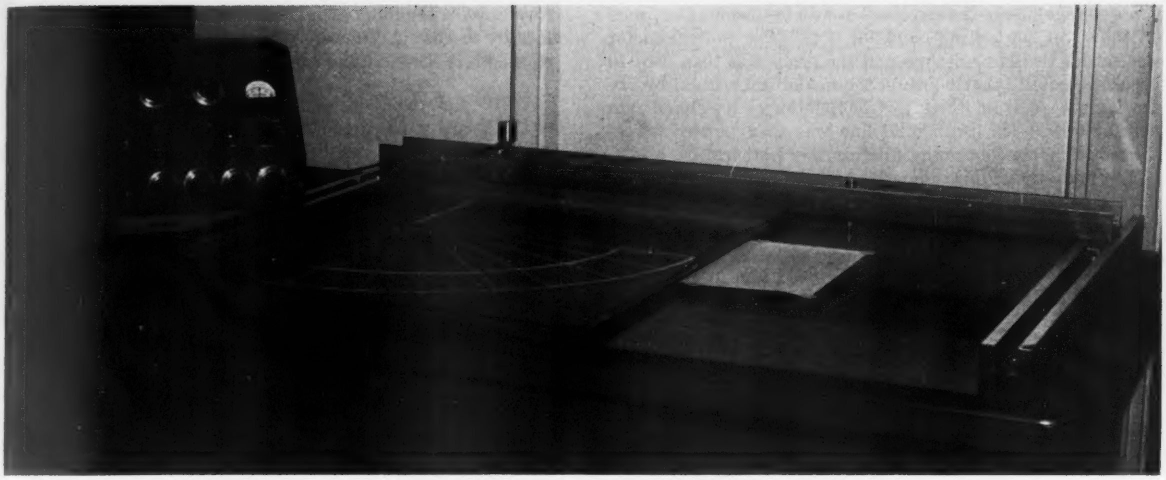

Fig. 1 Electrical analogy test equipment

for solving two-dimensional heat transfer problems, the heat flux and temperature distribution within the walls of the combustion chamber may be quite accurately determined. In this paper a heat transfer analysis is made to determine the heat flux and temperature distribution within the walls of tubular and drilled passage thrust chambers which are cooled with JP-4 (2) and RFNA (3), respectively.

Solution of Two-Dimensional Heat Transfer Problems

General Considerations

The use of simplified conduction equations will give erroneous results when applied to the solution of the heat transfer conditions which occur when irregular coolant passage geometries are involved. It has been shown in (1) that two-dimensional steady state heat transfer problems involving irregular geometries may be easily solved by the use of electrically conductive paper. The basic assumptions used in analyzing heat conduction problems by this method are:

1 The similarities between electrical flow and heat flow are applicable to the problems under consideration.

2 Two-dimensional heat flow predominates.

3 The metal thermal conductivity is independent of temperature.

4 The various film coefficients are correctly represented even though geometric similarity is not achieved.

Electrical Analog

The test installation used at Aerojet to solve these heat transfer problems is shown in Fig. 1. The base of the plotter is made from $\frac{1}{2}$ in. Masonite; fastened to this base are two steel bars which serve as guides for the pantograph tracer. The pantograph tracer consists of an aluminum U beam; located inside the U beam is another slider which holds the voltage probe and the marker. The marker will contact the paper only when force is applied. A weight is fastened to the brass voltage probe so that a uniform pressure may be applied to the conductive paper surface at all times.

A schematic of the power source and voltage measuring device is shown in Fig. 2. Power is supplied by a 6-volt lantern battery. Four 10-turn 200-ohm, 2-watt potentiometers are connected in parallel with the battery. By reading the dials on the potentiometers, the per cent of battery voltage may be determined. Leads from these potentiometers are connected to the model. The per cent of battery voltage is proportional to the temperatures imposed as boundary conditions on the model. A 1000-ohm 10-turn potentiometer is used for accurate measurement of the per cent of battery voltage. Zero deflections on the microammeter indicate when the value read on the dial of the 1000-ohm helipot is the per cent voltage the probe is measuring. Since there is no current flow in the measuring circuit, the resistance of the lines will not affect the electrical measurement. Although not shown in the schematic, a potentiometer circuit has been installed in the measuring circuit which enables the resistance of the teledeltos paper to be determined.

The electrically conductive paper was glued to a piece of $\frac{1}{4}$ in. Masonite. This backing offers the necessary rigidity required by the model. Rubber cement was used as the bonding material because it provided a good bond and did not react with the paper. It was clean to use and is easily removed from the Masonite after the test.

Silver dots, made from electrically conductive silver paint, were used as the connecting medium at the boundary surfaces. A series of dots rather than bands were applied as the boundary connection in order to eliminate heat transfer along the boundary surface even though the exact size and spacing of these dots did not materially affect the isothermal lines. Dots of approximately $\frac{1}{16}$ in. diam and $\frac{1}{8}$ in. between the centers were used throughout these tests.

To impress constant temperature (voltage) boundary conditions on the model, electrical terminals were provided by painting bands of silver paint along the boundaries. The gas temperature was impressed on a $\frac{1}{2}$ in. silver band on the model's gas film and the liquid bulk temperature was impressed on a silvered area located within the coolant passages.

Voltage to the various terminals was adjusted by means of a variable potential source. The probe was placed in contact with each terminal in turn and the voltage adjusted by a variable resistor to a predetermined value. The form on which the plotting is to be done is fixed under pantograph tracer. The usual procedure in plotting was first to measure tempera-

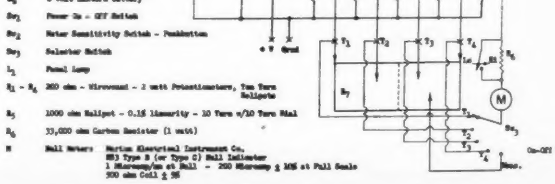

Fig. 2 Electrical analogy voltage measuring circuit

ture (voltage) along the combustion wall by placing the probe on the silver connecting bands or dots. The potentiometer was set for the value desired and the probe was then used to bracket carefully that point on the model test section by observing the point at which the microammeter registered zero current flow. The isothermal line was then plotted across the model before continuing with another isotherm.

To obtain the required length of teledeltos paper which will represent the film heat transfer coefficients, the following formula was used

$$L_f = \frac{K_m S}{h_f R_p} \qquad [1]$$

where

R_p = paper ratio =

$$\frac{\text{resistance}/\square^{3} \text{ of paper representing } h_f}{\text{resistance}/\square \text{of paper representing metal}}$$

In the case of applying a film to a curved surface, the L_f calculated from Equation [1] should be applied to the surface as shown in Fig. 3 in order that one-dimensional heat transfer in the boundary layer may be simulated.

It is possible to calculate a length of paper having the same resistance as the film but fitting the contour of the curved surface by the use of Equation [2a or 2b]. (Derivation of these equations is shown in the Appendix.)

convex surface:

$$\frac{L_f}{r} = \ln (r + L') - \ln r \qquad [2a]$$

convex surface:

$$\frac{L_f}{r} = \ln r - \ln (r - L') \qquad [2b]$$

where L_f is the length of paper calculated by Equation [1] and L' is the length of contoured paper.

In representing film coefficients by a curved piece of paper, slits must be cut in the paper to ensure that one-dimensional flow occurs in the simulated film resistance.

Once the isothermal lines are determined, the heat flow lines are then determined graphically. In the graphical analysis, the heat flow lines are drawn perpendicular to the isothermal lines. The space between two heat flow lines constitutes a heat flow tube. The amount of heat flowing in a heat flow tube can then be calculated and consequently the localized value of heat flux can then be determined.

[3] The term ohms/square is the resistance of a unit square of the electrically conductive paper which remains constant regardless of the size of the square. The resistance is measured between silver strips located on opposite sides of the square.

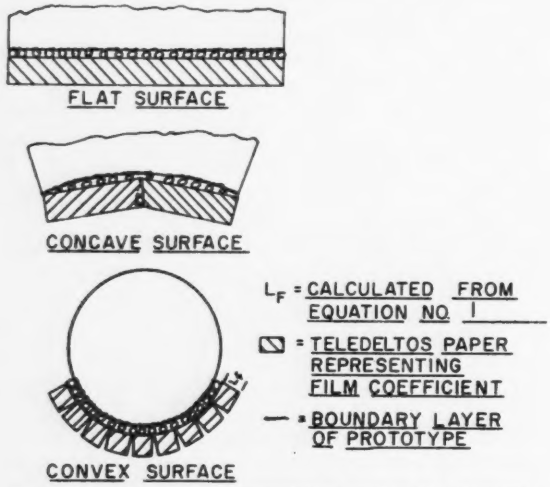

Fig. 3 Boundary layer representation used on the electrical analogy test

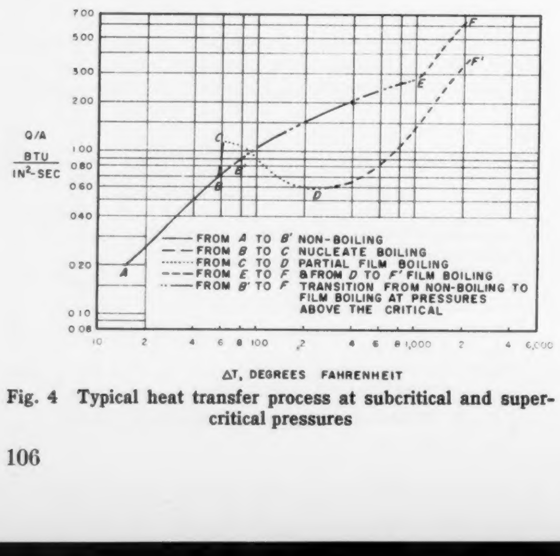

Fig. 4 Typical heat transfer process at subcritical and supercritical pressures

Liquid Film Heat Transfer Coefficients

General Discussion

Rocket thrust chambers designed for long duration firings must be cool to protect the walls from the high temperature, high velocity combustion gases. This is usually accomplished by passing one of the propellants through passages located within the walls of the thrust chamber. At the high heat fluxes and temperatures encountered in thrust chamber operations the propellants may become corrosive, decompose, or deposit impurities upon the heating surface thereby reducing the cooling effectiveness. It is impossible to calculate, with any degree of certainty, the propellant heat transfer characteristics under these conditions. Experimental test techniques have been developed which enable the heat transfer characteristics of various coolants to be evaluated at conditions simulating those encountered during thrust chamber operations.

Shown in Fig. 4 is the heat transfer process which would be predicted for a pure nonreacting liquid like liquid nitrogen (4).

In the nonboiling region A-B, the thermal resistance to heat transfer remains essentially constant. The heat transfer process will remain in the nonboiling region providing the wall surface temperature remains below its saturation or critical temperature. At increased rates of heat transfer, the mode of heat transfer will be influenced by the pressure imposed upon the coolant.

At subcritical pressures, nucleate boiling (B-C) will occur at the heated surface when the wall surface temperature slightly exceeds the saturation temperature of the coolant. The increased turbulence caused by the fast-moving bubbles greatly reduces the thermal resistance to heat transfer. In this region it is possible to increase the rate of heat transfer with only a slight increase in the heating surface temperature. As the rate of heat transfer is further increased (B) the bubbles start to coalesce and form a high resistance vapor film. If the thermal resistance offered by this vapor is high enough, the temperature of the wall may exceed its melting point, or the working pressure may exceed the stress limit of the wall at these high temperatures.

At supercritical pressure, the nonboiling condition exists at heating surface temperatures below the critical (A-B). Beyond this point, a gradual transition to a stable film boiling boundary layer begins (B'E). A stable film boiling region exists from E to F.

The upper limit of heat flux occurs when the heating surface temperature reaches its melting point or the stress limit of the heating surface is exceeded at these elevated temperatures.

The heat transfer conditions described are what might be expected when a pure, nonreactive and stable liquid is used as a coolant. Unfortunately, a rocket propellant may not always meet these requirements. At low rates of heat transfer, the heat transfer coefficients may be estimated quite adequately by either theoretical equations or empirical equations based upon heat transfer measurements of other liquids.

Since it is impossible to predict the heat transfer characteristics of rocket propellants in the nucleate and film boiling region, rocket designers are forced to base their heat transfer calculations upon experimentally determined heat transfer coefficients.

Rocket Propellants

Jet Fuel (JP-4)

The heat transfer characteristics of jet fuels have been obtained on JP-3 and JP-4. If JP-4 was used as a regenerative coolant at a pressure below its critical pressure, the heat transfer process would have been in the nonboiling region provided the wall temperature was below the saturation temperature of JP-4. The nonboiling heat transfer coefficient for JP-4 may be estimated by

$$Nu = 0.0214\,Re^{0.8}Pr^{0.4} \qquad [3]$$

If the heat transfer rates were sufficiently high the heat would have been transferred in the nucleate boiling region. The heating surface wall temperature remained essentially constant in this region. The upper limit of nucleate boiling could be estimated from

$$\frac{(Q/A)_{ul}}{(Q/A)_{\text{conv}}} = \frac{1.11 \times 10^4}{PG} \qquad [4]$$

In regenerative cooling of rocket thrust chamber with JP-4 the cooling is usually carried out under pressures which exceed the critical pressure of the coolant. In this case the heat transfer process would proceed as follows: A nonboiling condition exists up to a heat flux at which the wall in contact with the fuel reaches the critical temperature of the fuel. The film boiling data obtained on this hydrocarbon mixture may be compared with the film boiling data obtained for liquid nitrogen as follows:

1 With liquid nitrogen, there was a gradual transition into film boiling, whereas in the case of JP-4, there was an abrupt transition.

2 With liquid nitrogen there was a constant film cooling heat transfer coefficient which was less than the nonboiling heat transfer coefficient. With JP-4, the heat transfer coefficient did not remain constant in the film-boiling region.

3 The upper limit of heat flux was obtained when the temperature of the heating tube reached a point where the metal was not able to withstand the external pressure of the system. Whether the film boiling heat transfer obtained on JP-4 would have followed the same trend as the liquid nitrogen at increased pressures is not known.

The trend of JP-4 heat transfer data at supercritical pressures is shown in Fig. 5. The solid line is the experimentally determined heat transfer data obtained from (2). The dashed line is the extrapolated heat transfer data used in the analysis of the heat transfer occurring in the tubular thrust chamber. It is felt that the errors introduced extrapolating the nonboiling heat transfer data in the range shown will be small. The errors introduced by extrapolating the 500-psia data to higher pressures are not known and further experimental work is warranted.

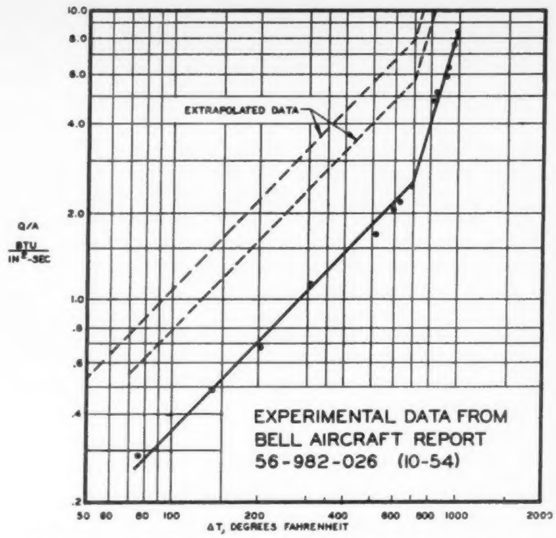

Fig. 5 Heat transfer characteristics of JP-4 at 500 psia

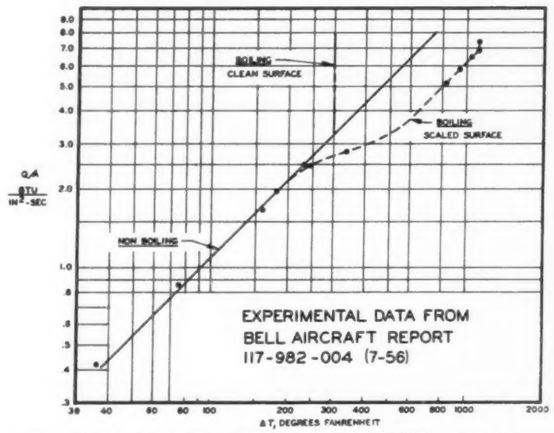

Fig. 6 Heat transfer characteristics of RFNA at 700 psia

Nitric Acid

Heat transfer tests conducted on nitric acid showed that the nonboiling heat transfer coefficient could be estimated by [3].

$$Nu = 0.027Re^{0.8}Pr^{0.4} \qquad [5]$$

In the case of WFNA (6), nucleate boiling occurred at a surface temperature 50 to 100 F above the saturation temperature of the acid. As the heat flux increased, the temperature increased slightly. A light scale was formed on the heating surface. At the upper limit of nucleate boiling, burnout occurred. In the case of red fuming nitric acid, containing only traces of impurities, and no HF inhibitor, a similar trend of data was observed. RFNA[4] containing only traces of impurities and 0.4 per cent HF deposited a large quantity of salt scale[5] on the heating surface, thus decreasing its effective heat transfer coefficient.[6] The trend of heat transfer data

[4] RFNA HNO_3—82%, NO_2—14%, H_2O—2.5%, HF—0.6%.

[5] The scale is composed of mainly iron, nickel and chromium salts.

[6] Refers to the calculated heat transfer coefficient based upon the temperature drop from the fluid bulk temperature to the metal surface temperature.

that can be expected for RFNA at 700 psia is shown in Fig. 6.

The heat transfer condition may be estimated in the nonboiling region by Equation [5] up to a ΔT of 225 F. Scale then forms on the heated surface and the effective heat transfer coefficient decreases. With the absence of experimental heat transfer data the rocket engine designer would be apt to conduct heat transfer calculation assuming nucleate boiling on a clean surface, which would lead to erroneous results.

The effect of this scale in reducing the effective heat transfer coefficient at high rates of heat transfer can be seen in the following data taken from (3). At a heat flux of 7 Btu/in.^{2}-sec, the temperature drop across the liquid film was found to be only 239 F whereas the temperature drop across the scale was estimated to be 816 F. If the heat transfer coefficient for a clean surface had been 0.0292 Btu/in.^{2}-sec, the presence of scale reduced the effective heat transfer coefficient 77 per cent to 0.0066 Btu/in.^{2}-sec.

Application to Thrust Chambers

By making use of the experimentally determined liquid film heat transfer coefficients and the electrical analogy method for solving two-dimensional heat transfer problems, the heat and temperature distribution within the walls of the combustion chamber may be determined.

The heat transfer condition existing in a 0.030-in. wall tubular aluminum thrust chamber being cooled with JP-4 was investigated. The nonboiling liquid film heat transfer coefficient which was calculated according to Equation [3] was found to be 0.0082 Btu/in.^{2}-sec-°F. Using the same weight flow of fuel, the nonboiling heat transfer coefficient existing in the finned tube was found to be 0.017 Btu/in.^{2}-sec-°F. Details of the boundary conditions used in this investigation are shown in Table 1.

Table 1 Boundary conditions for the tubular thrust chamber

	Unfinned tube	Finned tube
Gas film heat transfer coefficient, Btu/in.^{2}-sec-°F	0.00085	0.00085
Liquid film heat transfer coefficient, Btu/in.^{2}-sec-°F	0.00823	0.0173
Thermal conductivity of aluminum (Btu/in.-sec-°F)	0.00207	0.00207
Coolant temperature, °F	150	150
Combustion temperature, °F	5230	5230
Scale factor	20/1	20/1
R_p	1	1
L_{f_g}, inches	6.9	6.9
L_{f_l}, inches	0.7	0.34
L'_{f_l}, inches	0.54	0.30

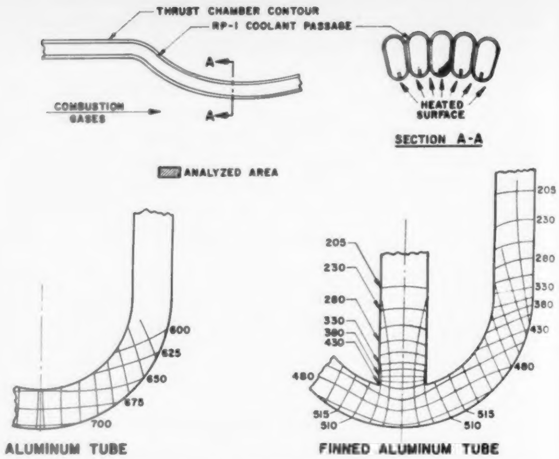

Fig. 7 Temperature distribution within the walls of a tubular thrust chamber

Shown in Fig. 7 are the isothermal profiles obtained from the electrical analogy test technique. These profiles represent a quarter section of a tube, which makes up the throat section of a thrust chamber. The hot combustion gases are assumed to have equal effectiveness over the total surface area exposed to the hot gases.

In the case of the unfinned tube the gas side wall temperature was around 700 F with an inside wall temperature of 650 F. A maximum heat transfer rate of 3.7 Btu/in.^{2}-sec was obtained on the liquid side. Because the isothermal lines were essentially straight and parallel, the heat flux of 3.7 Btu/in.^{2}-sec was obtained on the gas side. In the case of the finned tube, where the JP-4 becomes a more effective coolant, the gas-side temperature is only 510 F and a liquid side wall temperature of 445 F was obtained. Accompanying this reduced wall temperature was an increase in the rate of heat transfer. The maximum heat flux into the coolant passage was found to be 5.5 Btu/in.^{2}-sec. As can be seen from Fig. 5, this high rate of heat transfer can be easily absorbed by the coolant.

It is noted that the nonboiling heat transfer condition was present in the coolant passage. This is indicated by the fact that the coolant side wall temperature was below the critical temperature of JP-4 and consequently below the heat flux where film boiling may be expected.

The heat transfer conditions existing in a 0.165-in. drilled passage thrust chamber which is cooled with RFNA were investigated. The results of this investigation are shown in Fig. 8. These sections represent a radial section cut from the thrust chamber. Hot gases are flowing past the bottom sur-

Table 2 Boundary conditions for the drilled passage thrust chamber

	Nonboiling stainless steel	Nonboiling aluminum	Boiling aluminum clean surface	Boiling aluminum scaled surface
Gas film heat transfer coefficient, Btu/in.^{2}-sec-°F	0.0020	0.0020	0.0020	0.0020
Liquid film heat transfer coefficient, Btu/in.^{2}-sec-°F	0.011	0.011	0.011 and 375	0.011 and 0.0060
Thermal conductivity of metal, Btu/in.-sec-°F	0.00035	0.0025	0.0025	0.0025
Coolant temperature, °F	75	75	75	75
Combustion temperature, °F	4500	4500	4500	4500
Scale factor	20/1	20/1	20/1	20/1
R_p	1	7.5	7.5	1
L_{f_g}, inches	3.5	3.3	3.35	3.38
L_{f_l}, inches	0.529	0.506^-	0.506^-	1.545 to 1.639

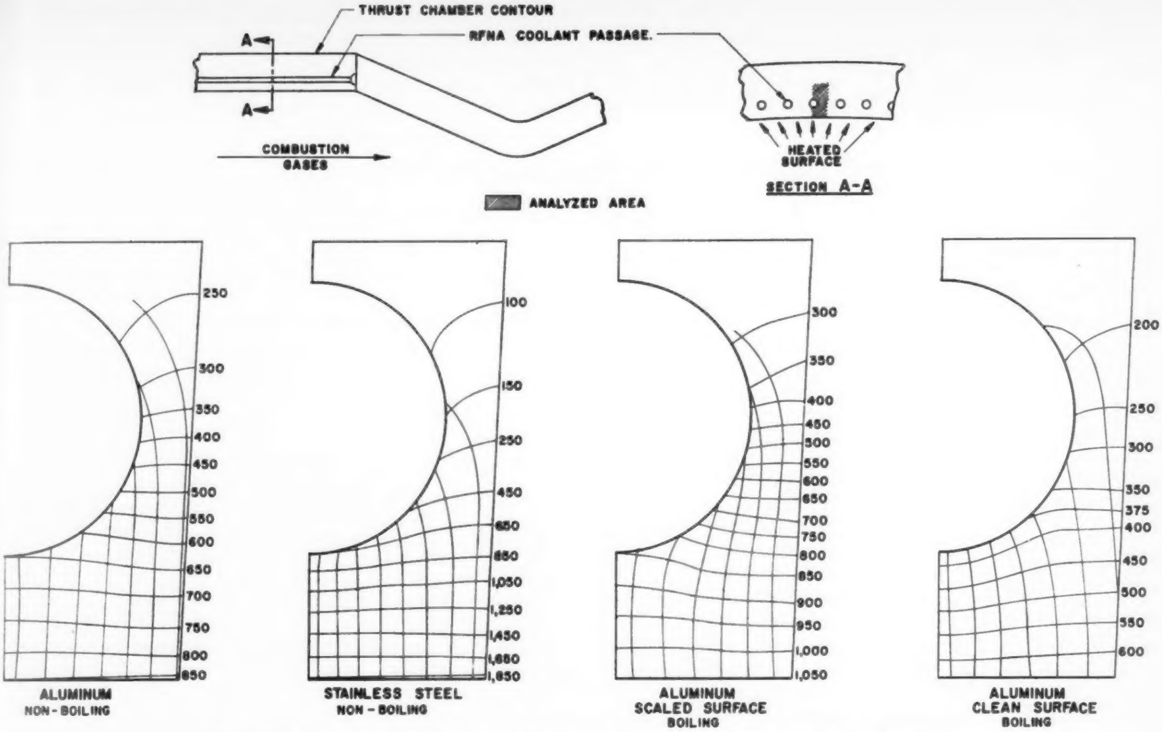

Fig. 8 Temperature distribution within the walls of a drilled passage thrust chamber

face and RFNA is flowing through drilled passage. The boundary conditions used in this analysis are shown in Table 2. The nonboiling liquid film heat transfer coefficient was calculated by Equation [5]. The heat transfer conditions in the boiling region were estimated from the data shown in Fig. 6.

A comparison between the heat transfer conditions existing in an aluminum chamber and those existing in a stainless steel thrust chamber is shown in Fig. 8. The results of this comparison are summarized in Table 3.

Table 3 Heat transfer conditions in aluminum and stainless steel thrust chambers

	Aluminum	Stainless steel
Gas side wall temperature, °F	850	1850
Liquid side wall temperature, °F	650	650
Q/A gas side, Btu/in.^{2}-sec	7.1	5.4
Q/A liquid side, Btu/in.^{2}-sec	6.5	6.6

As would be expected, the use of a lower thermal conductivity material, such as stainless steel, gives decreased rates of heat transfer across the combustion wall and increased wall temperatures. The shape of the isothermal lines, curving away from the coolant passage of the aluminum section, indicates that the aluminum adjacent to the passage tends to aid in the cooling process, whereas with the stainless steel section the isothermal lines tend to curve around the coolant passage causing heat to flow into the coolant rather than around the passage.

In actual practice, the heat transfer condition shown here is not possible because as soon as the coolant side wall temperature reaches the saturation temperature of the coolant, boiling will occur.

Also shown in Fig. 8 are the heat transfer conditions encountered when heat is transferred in the nucleate boiling region. In the absence of experimental data, the most logical means of estimating heat transfer conditions in the nucleate boiling region is to assume that the coolant wall temperature remains at a constant temperature slightly in excess of the saturation temperature of the liquid, in this case, 380 F. This was accomplished in this analysis by imposing a constant temperature along the coolant where the heat flux is in excess of 3.3 Btu/in.^{2}-sec. Based upon experimental data of (3), there is a considerable reduction in the heat transfer coefficient due to scale formation. As determined from Fig. 6, the heat transfer coefficient was equal to 0.0060 Btu/in.^{2}-sec-°F at heat fluxes above 3.3 Btu-in.^{2}-sec. This condition was analyzed by applying coefficients on the liquid side varying between 0.011 and 0.006 Btu/in.^{2}-sec-°F.

A comparison of the heat transfer conditions encountered with a scaled and unscaled surface is shown in Table 4.

Table 4 Heat transfer conditions encountered with a scaled and unscaled surface

	Clean surface	Scaled surface
Gas side wall temperature, °F	650	1050
Liquid side wall temperature, °F	380	850
Gas side heat flux, Btu/in.^{2}-sec	7.35	6.95
Liquid side heat flux, Btu/in.^{2}-sec	10	4.8

Nucleate boiling on a clean surface offered very little resistance to the flow of heat, resulting in extremely high heat transfer rates. Considerable resistance to the flow of heat was offered by the nucleate boiling on a scaled surface. The isothermal lines tended to bend away from the coolant pas-

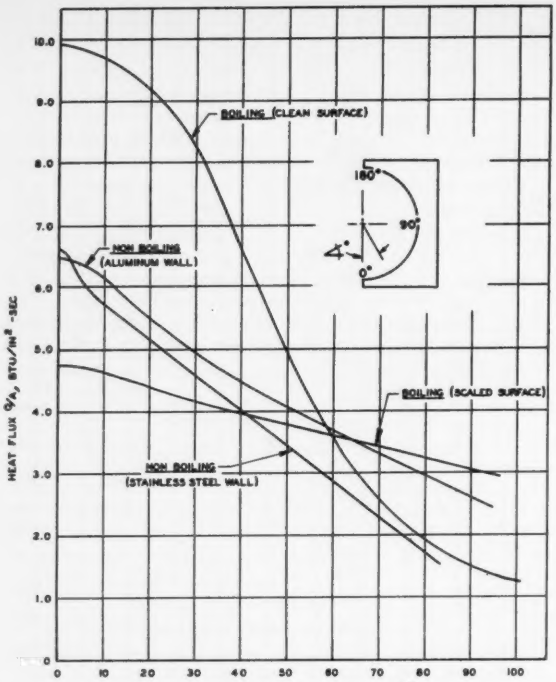

Fig. 9 Heat flux distribution around the coolant passage

sage, thereby resulting in low heat fluxes at the coolant passage and an extremely high combustion wall temperature.

Shown in Fig. 9 is a plot of the heat flux distribution around the coolant passage for the various coolant characteristics considered. The extremely high heat fluxes occurring with boiling on a clean surface is above the maximum heat flux the coolant is capable of absorbing. This condition could cause failure during thrust chamber operation.

The lowest heat flux obtained at the coolant passage occurred with boiling on a scaled surface. This heat transfer condition is also critical due to the high wall temperature, which exceeds 1000 F. The application of an aluminum oxide coating to the combustion wall would help alleviate these severe heat transfer conditions. As can be seen from this analysis, an extremely high heat transfer coefficient may be detrimental to the cooling of a drilled passage thrust chamber. With irregular geometric configurations, a two-dimensional heat transfer analysis based upon experimentally determined heat transfer coefficients is a necessity to insure a satisfactory solution.

Appendix: Derivation of Equations [2a and 2b]

Consider a segment of a cylinder of radius r and height $\tau = b$, the thickness of the conducting paper. Then if

$$R = \rho \frac{L}{A}$$

where

R = resistance to electric flow
ρ = resistivity of the paper
L = length of paper calculated by Equation [1]
A = area of paper to flow of current = $2\pi r\tau\ \alpha/360$
α = included angle of cylindrical segment of curved surface

Then the mean area to flow of the contoured paper should be similar to the area of flow of the model calculated by Equation [1]. That is, the film obtained from Equation [1] has the same flow area as the model curved surface, but the contoured paper must be adjusted in length to L' and area Am, to give the same flow resistance.

flow area on curved surface:

$$A_2 = 2\pi r\tau \frac{\alpha}{360}$$

which is also the flow area of the film calculated from Equation [1].

The mean flow area of the film from

$$Am = \frac{A_1 - A_2}{\ln \dfrac{A_1}{A_2}} = \frac{2\pi(r + L')\tau \dfrac{\alpha}{360} - 2\pi r\tau \dfrac{\alpha}{360}}{\ln \dfrac{2\pi(r + L')\tau \dfrac{\alpha}{360}}{2\pi r\tau \dfrac{\alpha}{360}}}$$

If resistances are to be equal

$$\rho \frac{L}{A} = \rho \frac{L'}{Am}$$

where L is the length of film paper from Equation [1].

$$\frac{\rho L}{2\pi r\tau \dfrac{\alpha}{360}} = \frac{\rho L' \ln \dfrac{2\pi(r + L')\tau \dfrac{\alpha}{360}}{2\pi r\tau \dfrac{\alpha}{360}}}{2\pi(r + L')\tau \dfrac{\alpha}{360} - 2\pi r\tau \dfrac{\alpha}{360}}$$

$$\frac{L}{r} = \frac{L' \ln \dfrac{(r + L')}{r}}{(r + L) - r}$$

$$\frac{L}{r} = \ln (r + L') - \ln r$$

Having L from Equation [1] and radius of curved surface r, the length of contoured paper L' giving the same resistance as L can be calculated. Then the single contoured piece can be cut out and placed on the model with more ease than the strips as shown in Fig. 3. It may be that L' will be too large for practical application and strips will have to be used, but this method may be applied in many cases.

If the contoured paper film is to be applied to the concave side of the curved surface, by a similar proof it can be shown that

$$\frac{L}{r} = \ln r - \ln (r - L')$$

References

1 Dean, L. E., "The Solution of Two-Dimensional Steady State Heat Transfer Problems by the Use of Electrically Conductive Paper," ARS Preprint 246–55, Nov. 1955.

2 Beighley, C. M., and Dean, L. E., "A Study of Heat Transfer to JP-4 Jet Fuel," Jet Propulsion, vol. 24, 1954, p. 180.

3 Dean, L. E., "Heat Transfer Characteristics of RFNA," Bell Aircraft Report 117-982-004, July 1956.

4 Dean, L. E., and Thompson, L. M., "Study of Heat Transfer to Liquid Nitrogen," ASME Preprint 1152-56, July 1956.

5 Hatcher, J. B., "High Flux Heat Transfer and Coke Deposition of JP-3 Fuel Mixture," Progress Report 20-157, Jet Propulsion Laboratory, Pasadena, Calif.

6 Ashley, E., "Heat Transfer Measurements for WFNA," Bell Aircraft Corp. Report 56-982-016, 1953.

Analysis of an Inertial Guidance System

D. B. DUNCAN[1]

Autonetics, A Division of North American Aviation, Inc., Downey, Calif.

The characteristics of an inertial navigation system for a simplified guidance problem are described. Error equations relating component performance to guidance accuracy are derived. These equations exhibit the 84 min period oscillations which typify inertial systems.

Introduction

INERTIAL guidance is a relatively new method and means of navigation of very general application which is quite distinct in principle from older forms, such as celestial navigation, dead reckoning, piloting and radio systems. The significance of this new navigation technique is now generally recognized.

Several recent papers (1, 2, 3, 4)[2] have discussed the general characteristics of inertial guidance. The present paper is an extension of such work to include performance analysis.

A simplified guidance problem is considered, namely, navigation on a spherical nonrotating body. This has been done primarily so that significant features can be emphasized without the mathematical complexity associated with the more general problem. The general characteristics of this system, as well as the results of the analysis, are, however, only slightly modified when extended to a more realistic guidance problem.

Rectangular Coordinates on a Flat Earth

As a first and greatly oversimplified example of inertial guidance, consider the problem of locating a cart on the top of a level table such as that shown in Fig. 1.

The cart is initially at rest at some known position. A force is applied starting it along some path on the table. Its position at any time can be determined by measuring and doubly integrating the applied acceleration. This is the basic concept behind an inertial guidance system.

A mechanization of even this simple problem would bring out many of the significant features. First, and perhaps most important of these, is that acceleration is a vector quantity. Each accelerometer can sense only one component of the total vector acceleration. Therefore, each instrument must not only be accurate itself, but must be maintained in a precisely known orientation. A second fact is that no accelerometer can distinguish between acceleration and gravity. Thus if the output of one of the acclerometers is to give the x-position, then the accelerometer must be aligned along the x-axis at all times. Misorientation will cause it to sense the y-component of either acceleration or gravity.

For this example the inertial system could be conveniently split into three subsystems:

1 The accelerometers which sense x and y components of the acceleration of the cart. These instruments, in principle at least, can be identical to the many varieties of commercial accelerometers currently available. Quantitative analysis shows, however, that the accuracy requirements imposed on these instruments require precision beyond that now generally available. An earlier paper indicates some of the practical problems involved in acceleration measurement in inertial guidance (5). No attempt will be made in this paper to amplify that discussion.

2 A stable platform which controls the orientation of the accelerometers so that each senses only the correct component of acceleration. The most straightforward way of mechanizing such a stable platform is to use an assemblage of gyroscopes arranged so as to maintain each axis angularly fixed in inertial space (6). Again, these instruments are, or can be, identical in principle to standard gyroscopes, but must satisfy much more stringent accuracy requirements.

3 A computer which doubly integrates the outputs of the two accelerometers to determine position. (In some cases, however, the accelerometers are designed to perform one or both steps of integration within the instrument.) The computer can be mechanized using either analog or digital techniques, or a combination thereof.

The operation of an inertial autonavigator for more realistic guidance problems is remarkably similar to this example. The navigator can still be split into the same three subsystems, and the functions of each subsystem, conceptionally at least, remain almost identical.

Rectangular Coordinates in a Spherical Non-Rotating Body

When the size of the "table top" becomes of the order of miles or hundreds of miles, the system outlined above would develop prohibitively large errors.

As the distance from the center increases, the accelerometers which remain parallel to their initial orientation will sense a lateral component of gravity proportional to the sine of the angle traveled. The double integral of this input would produce a large and increasing error. For reasonable navigation, some method of correcting for this lateral gravity component must be found. If the distance traveled from the center of the coordinate system is not too large, a simple method can be

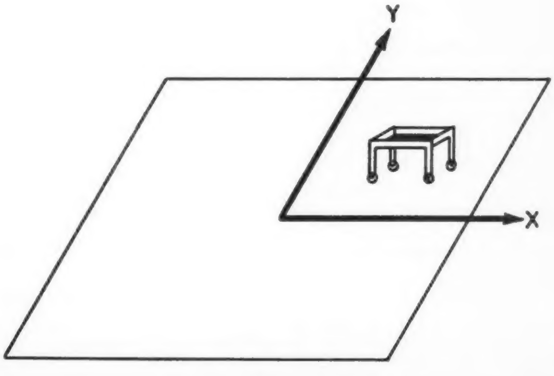

Fig. 1 Table configuration

Received July 31, 1957.

[1] Manager, Advanced Engineering.

[2] Numbers in parentheses indicate References at end of paper.

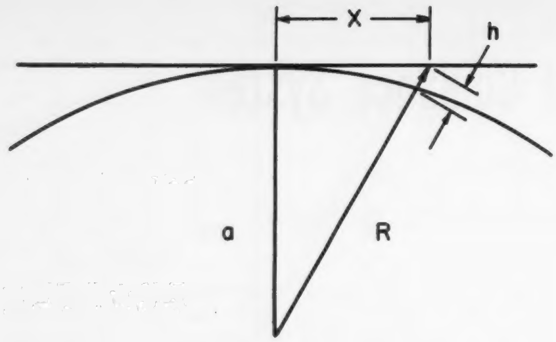

Fig. 2 Rectangular coordinate system

used; the computer determines these corrections as functions of x and y. Referring to Fig. 2, where

a = radius of the earth (assumed to be spherical)
R = distance of the vehicle from the center of the earth
h = altitude of the vehicle above the surface of the earth
x, y = rectangular coordinates on the "table" whose origin is at the point where the table is tangent to the earth
g_0 = gravitational acceleration at the surface of the earth
g = gravitational acceleration at the location of the vehicle
g_x, g_y = x and y components of the gravitational acceleration

Expressions for these lateral components of gravity are

$$\left.\begin{aligned} g_x &= \frac{g_0\, a^2 x}{(a+h)^3} \\ g_y &= \frac{g_0 a^2 y}{(a+h)^3} \end{aligned}\right\} \qquad [1]$$

The accelerations sensed by the x and y accelerometers become in this case

$$\left.\begin{aligned} A_x &= \ddot{x} + g_x \\ A_y &= \ddot{y} + g_y \end{aligned}\right\} \qquad [2]$$

A simple case which illustrates the principles occurs when departures from the origin are sufficiently small to neglect the factor (h/a). Under these conditions the expressions for the accelerations become

$$\left.\begin{aligned} A_x &= \ddot{x} + \frac{g_0}{a}\, x \\ A_y &= \ddot{y} + \frac{g_0}{a}\, y \end{aligned}\right\} \qquad [3]$$

The gravity corrections are therefore simple linear functions of x and y. The system can be mechanized in essentially the same manner as that considered before if the value of the gravity correction is computed and fed back as a correction on the accelerometer. A transducer is required to convert the computed value to an equivalent force on the accelerometer. A block diagram for the system in this case is shown in Fig. 3.

The acceleration of the platform with respect to inertial space in the x and y directions is sensed by accelerometers mounted on a stable platform and doubly integrated to give position as an output. The gravity correction term is computed as a function of the output and introduced as a feedback or bias on the accelerometer.

The situation described above where motion is confined to lie in the "table" or xy-plane is, of course, highly artificial. In the more general case, position would be defined by the three coordinates (x, y, z) and the corresponding expressions for acceleration become

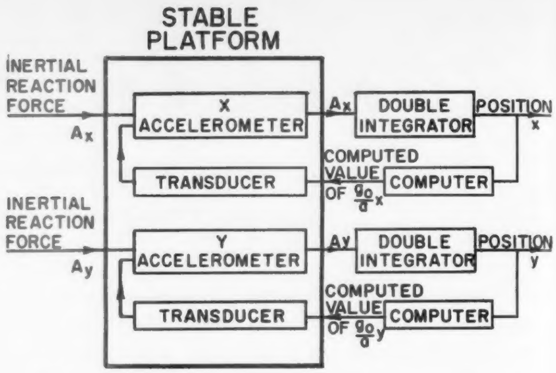

Fig. 3 System block diagram (rectangular coordinates)

$$\left.\begin{aligned} A_x &= \ddot{x} + g_x \\ A_y &= \ddot{y} + g_y \\ A_z &= \ddot{z} + g_z \end{aligned}\right\} \qquad [4]$$

For small values of x, y and z, linear approximations to the gravity correction terms can be made, and these expressions reduce to

$$\left.\begin{aligned} A_x &= \ddot{x} + \frac{g_0}{a}\, x \\ A_y &= \ddot{y} + \frac{g_0}{a}\, y \\ A_z &= \ddot{z} + g_0\left(1 - 2\,\frac{z}{a}\right) \end{aligned}\right\} \qquad [5]$$

A mechanization of these equations would be identical in form to that given in Fig. 3.

Cylindrical Coordinates

As the distance from center of the coordinate system shown in Fig. 2 becomes comparable with the radius of the earth, the size of the gravity correction becomes of the order of 1 g. Accurate mechanization of such a large acceleration correction term places stringent requirements on the computer and the transducer used to convert the computed value to an equivalent acceleration. While these problems are technologically solvable, it is generally more reasonable to rotate the platform so as to keep the accelerometers normal to the local gravity vector. For a general path this requires rotation about two axes. Often, however, the path of the vehicle may lie approximately in a straight line. In this case, only rotation about a single axis is required to keep the gravity correction terms small. A coordinate system of this type is shown in Fig. 4.

The XYZ axes are fixed in the body and hence in inertial space. The Y axis is chosen perpendicular to a reference great circle lying close to the desired path of the vehicle. The plane containing the XZ axes is referred to as the guidance plane. The orientation of the XZ axes in this plane can be arbitrarily chosen, but once defined remain fixed. The position of the vehicle is defined by coordinates corresponding to those of an ordinary cylindrical coordinate system: (a) a range angle, θ; (b) lateral distance from the guidance plane, y; and (c) distance from the polar axis of the coordinate system, ρ.

The x, y, z axes, referred to as true position coordinates, differ from the XYZ system by the rotation θ about the Y-axis, and correspond to the desired platform orientation. As the vehicle progresses around the guidance plane, the platform is rotated through the angle θ so as to remain locally level. As the vehicle departs laterally from the guidance plane, the gravity correction is computed in exactly the same manner as that considered previously for the flat coordinate system. As

mentioned earlier, effects due to the rotation of the earth and ellipticity are being ignored. While these are important, they do not change the essential nature of the problem.

The angular velocity of the coordinate system with respect to inertial space is given by

$$\bar{\omega}_i = \bar{1}_y \dot{\theta} \qquad [6]$$

and the vector position of the vehicle is given by

$$\bar{R} = \bar{1}_y y + \bar{1}_z \rho \qquad [7]$$

Where $\bar{1}_y$ is being used to define a unit vector along the y-axis. Using this expression, accelerations along the x, y, and z axes become

$$\left.\begin{aligned} A_x &= \rho\ddot{\theta} + 2\dot{\rho}\dot{\theta} \\ A_y &= \ddot{y} + g_y \\ A_z &= \ddot{\rho} - \rho\dot{\theta}^2 + g_z \end{aligned}\right\} \qquad [8]$$

The development can be carried on from this point with complete generality. Since, however, the purpose of this paper is to illustrate the principles involved, assume that the motion is restricted to the surface of the earth and that departure from the guidance plane is sufficiently small to ignore terms containing the factor $(y/a)^2$. Under these conditions the acceleration expressions become

$$\left.\begin{aligned} A_x &= a\ddot{\theta} \\ A_y &= \ddot{y} + \frac{g_0}{a} y \\ A_z &= g_0 - a\dot{\theta}^2 - \frac{y}{a}\ddot{y} - \frac{\dot{y}^2}{a} \end{aligned}\right\} \qquad [9]$$

Only the equations for range and lateral accelerations are of direct concern, since only two coordinates are required to define position for the restricted motion being considered.

Thus the output of the x or range accelerometer is to be doubly integrated and divided by the radius of the earth to give the range angle θ. The first integral, $\dot{\theta}$, can be used to give a signal for torquing the gyroscope controlling about the y axis to obtain the required angular rate with respect to inertial space about that axis. The output of the y or lateral accelerometer is doubly integrated to give the lateral position y. As before, however, a horizontal component of gravity must be computed and fed back to the y accelerometer as a correction term. A block diagram of the system is shown in Fig. 5.

Other methods of achieving the required θ rotation are available. For example, the gyros could remain inertially fixed while one or both accelerometers could be mounted on a separate platform which is driven through the angle θ by a mechanical drive. The logical extension of such a method leads to the "five-gimballed platforms" discussed by Wrigley (7).

Error Analysis

Homogeneous Equations

The guidance system illustrated in Fig. 5 can be used to determine position for the rather idealistic situation which is being considered. Any actual system, however, will not give exactly correct values of position. As a first step in deriving the errors in such a system, consider the equations which these errors must satisfy, ignoring for the moment the sources of these errors.

Five basic error parameters are needed which can be defined in the following way:

1 Errors in position, $\Delta\theta$ and Δy. The outputs of the range and lateral channels should indicate the true position of the vehicle, (θ, y). Defining $\Delta\theta$ and Δy as the differences in position of the vehicle as indicated by the guidance system and true position, these outputs are actually $\theta - \Delta\theta$ and $y - \Delta y$.

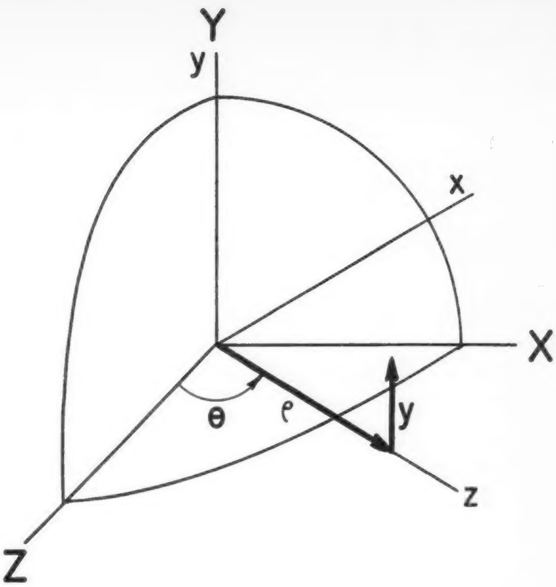

Fig. 4 Cylindrical coordinate system

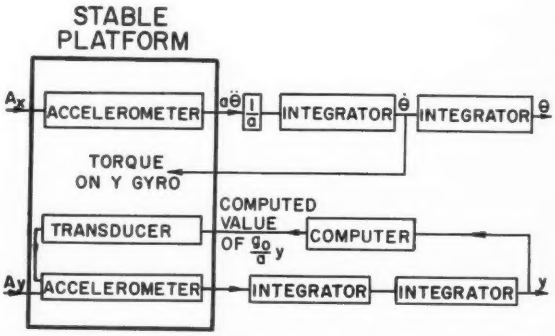

Fig. 5 System block diagram (cylindrical coordinates)

2 Platform error angles, ϕ_x, ϕ_y, ϕ_z. The stable platform should be oriented along the x, y, z axes as shown in Fig. 4. Again there will actually be errors. Define the x_p, y_p, z_p axes corresponding to actual platform orientation. The transformation between x, y, z and x_p, y_p, z_p coordinates can be defined by means of three Eulerian angles. Since these two coordinate systems differ from each other by small angles, the resulting transformation has the following characteristics:

(a) The transformation can be defined by giving three angles (ϕ_x, ϕ_y, ϕ_z) corresponding to the rotations positive in the usual sense about the xyz axes required to go from the xyz coordinate system to the x_p, y_p, z_p coordinates.

(b) The transformation is independent of the order of these rotations.

(c) The angles ϕ_x, ϕ_y, ϕ_z may be regarded as components of a vector $\bar{\phi}$.

The equation described by propagation of errors in the autonavigator can now be derived. The inertial reaction force in the x_p direction which will be sensed by the range accelerometer is given by

$$A_{x_p} = A_x + \phi_z A_y - \phi_y A_z = a\ddot{\theta} + \phi_z A_y - \phi_y A_z \qquad [10]$$

and the acceleration in the y_p direction by

$$A_{y_p} = A_y - \phi_z A_x + \phi_x A_z = \ddot{y} + \frac{g_0}{a} y - \phi_z A_x + \phi_x A_z \qquad [11]$$

Assuming for the moment that the components are per-

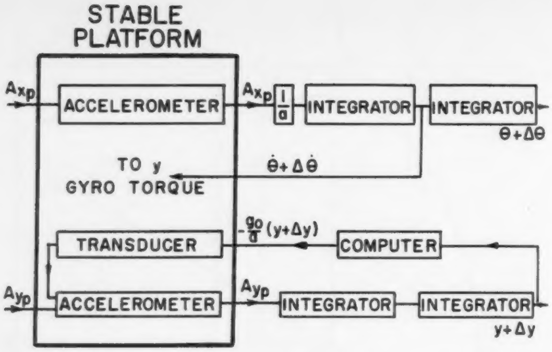

Fig. 6 System block diagram including error parameters

Fig. 7 Accelerometer

fectly mechanized, a block diagram of the system including the error parameters is given in Fig. 6.

From the block diagram, two of the error equations can be obtained immediately

$$\left.\begin{aligned} &\frac{1}{a}\int_0^t\int_0^\tau [a\ddot{\theta} + \phi_z A_y - \phi_y A_z]d\tau' d\tau = \theta + \Delta\theta \\ &\int_0^t\int_0^\tau [\ddot{y} + \frac{g_0}{a}\, y - \phi_z A_x + \phi_x A_z - \frac{g_0}{a} \times \\ &\qquad\qquad (y + \Delta y)]d\tau' d\tau = y + \Delta y \end{aligned}\right\} \quad [12]$$

The other three equations are obtained by equating two expressions for the angular velocities of the platform. One expression for these angular velocities, which follows directly from the definition of the ϕ angles, is

$$\overline{\omega_p} = \overline{\omega_c} + \dot{\overline{\phi}} \quad [13]$$

where $\overline{\omega_p}$ is the angular velocity of the platform with respect to inertial space and $\overline{\omega_c}$ is the angular velocity of the xyz coordinate system with respect to inertial space. The second expression for angular velocity of the platform is obtained from the system block diagram which shows that the only angular rate applied to the platform is about the y_p-axis and equal in magnitude to the integral of the output of the range mechanization which may be used to produce this rotation. The second equation for the angular velocity of the platform becomes

$$\overline{\omega_p} = \overline{1}_{y_p}(\dot{\theta} + \Delta\dot{\theta}) \quad [14]$$

Expressing $\overline{1}_{y_p}$ in the xyz coordinate system, this equation becomes

$$\overline{\omega_p} = (-\phi_z\overline{1}_x + \overline{1}_y + \phi_x\overline{1}_z)(\dot{\theta} + \Delta\dot{\theta}) \quad [15]$$

The resulting error equations can be simplified by introducing ψ angles defined as

$$\left.\begin{aligned} \psi_x &= \phi_x \\ \psi_y &= \phi_y - \Delta\theta \\ \psi_z &= \phi_z \end{aligned}\right\} \quad [16]$$

These correspond to platform misalignment from the position $\theta - \Delta\theta$, as defined by the computer rather than true position θ. Since platform torques are based upon computer position rather than true position, the ψ angles more properly measure performance of the platform components. For more complicated coordinate systems a similar transformation can be carried out and is essential to obtaining manageable equations. Substituting these relationships, the error equations become

$$a\Delta\ddot{\theta} + \frac{A_z}{a}(a\Delta\theta) = \psi_z A_y - \psi_y A_z \quad [17]$$

$$\Delta\ddot{y} + \frac{g_0}{a}\Delta y = -\psi_z A_x + \psi_x A_z \quad [18]$$

$$\dot{\psi}_x + \dot{\theta}\psi_z = 0 \quad [19]$$

$$\dot{\psi}_y = 0 \quad [20]$$

$$\dot{\psi}_z + \dot{\theta}\psi_x = 0 \quad [21]$$

Note that the ψ equations can be solved independently, which immediately implies that the behavior of the platform as defined by ψ angles is independent of any position errors.

Introduction of Mechanization Errors

In the previous section, five differential equations for the basic error parameters were derived. Since perfect components were assumed, there are no driving functions. The solution will therefore give the propagation of initial errors in an otherwise perfect guidance system. It is now necessary to replace the idealized components with reasonable approximations to the actual instruments. Again, since the purpose of the report is to describe the principles of inertial navigation, only a limited number of the important component errors will be considered. For the analysis of any actual system, the list would be much more extensive.

1 *Acceleration errors.* Until this point it has been assumed that the accelerometer gave a perfectly accurate measure of the inertial reaction force acting along the sensitive axis of the instrument. For any actual instrument, this could not be the case. A reasonable approximation to many instruments is indicated in Fig. 7. There are two errors in the output: a bias error δA independent of the imposed acceleration and a scale factor error ka which depends linearly on acceleration.

2 *Stabilization errors.* In deriving the error equation, the angular velocity of the platform with respect to inertial space was assumed to be exactly determined by the control torques applied to the gyroscopes controlling about the xyz axes. For the particular case considered, these rates were 0, $\dot{\theta} + \Delta\dot{\theta}$, and 0. Actually there will be uncertainty torques acting on the gyroscopes which will produce platform drift. Defining the drift rate of a particular gyroscope as being ϵ, the drift rate of the platform about xyz axes becomes ϵ_x, $\dot{\theta} + \Delta\dot{\theta} + \epsilon_y$, and ϵ_z.

3 *Initial errors.* In addition to component errors, there will be errors in initial position $\Delta\theta_0$, Δy_0; errors in initial velocity $\Delta\dot{\theta}_0$, $\Delta\dot{y}_0$; and errors in initial platform orientation ψ_{x0}, ψ_{y0}, and ψ_{z0}.

When mechanization errors of the accelerometer are included the output of the range accelerometer instead of being given by Equation [10] becomes equal to

$$(1 + k_x)A_{xp} + \delta A_x = (1 + k_x)(a\ddot{\theta} + \phi_z A_y - \phi_y A_z) + \delta A_x \quad [22]$$

and the output of the lateral accelerometer by

$$(1 + k_y)A_{yp} + \delta A_y = (1 + k_y)\left(\ddot{y} + \frac{g_0}{a}\, y - \phi_z A_x + \phi_x A_z\right) + \delta A_y \quad [23]$$

It is straightforward to repeat the process which led to the position error equations which now become

$$a\Delta\ddot{\theta} + \frac{A_z}{a}\, a\Delta\theta = \psi_z A_y - \psi_y A_z + k_x A_x + \delta A_x \quad [24]$$

$$\Delta\ddot{y} + \frac{g_0}{a}\Delta y = -\psi_z A_x + \psi_x A_z + k_y A_y + \delta A_y \quad [25]$$

In deriving the platform error equations, it is only necessary to replace Equation [14] by the expression

$$\overline{\omega_p} = \overline{1}_{xp}\epsilon_x + \overline{1}_{yp}(\dot{\theta} + \Delta\dot{\theta} + \epsilon_y) + \overline{1}_{zp}\epsilon_z$$

This can again be equated to Equation [17] and the platform error equations become

$$\dot{\psi}_x + \dot{\theta}\psi_z = \epsilon_x \ldots\ldots\ldots\ldots\ldots\ldots [26]$$

$$\dot{\psi}_y = \epsilon_y \ldots\ldots\ldots\ldots\ldots\ldots\ldots [27]$$

$$\dot{\psi}_z - \dot{\theta}\psi_x = \epsilon_z \ldots\ldots\ldots\ldots\ldots\ldots [28]$$

These are the complete error equations; their solution with the proper initial conditions defines the behavior of an inertial guidance system for the restricted case considered here.

Solution of Error Equations

The most significant characteristic of errors in inertial navigation can be seen from Equations [24 and 25]. These show that the position errors satisfy the equation of an undamped harmonic oscillator of period $T = 2\pi(a/g)^{1/2} = 84.4$ min, assuming values of a and g at the earth's equator. This is the so-called Schuler period, named after its discoverer who explained its significance for acceleration-sensitive inertial systems operated on the earth (8). All of the physical intuition which has been developed from considerations of simple pendulums immediately applies. For example, an impulse driving function would give rise to undamped sinusoidal oscillations.

The only difficulty in obtaining a complete solution to these equations rests in assumptions on the path of the vehicle and the form of the driving functions. The following set of assumptions form a reasonable approximation to many cases of interest and lead to simple exact solutions.

1 All mechanization errors are constant.

2 Motion is in a straight line along the guidance plane. Velocity is constant except for a rapid change at $t = 0$, and is small in comparison to $(ag_0)^{1/2}$ or satellite velocity. This assumption is equivalent to

$$A_x = v\delta(t)$$

$$A_y = 0$$

$$\dot{\theta} = v / a \ll (g_0/a)^{1/2}$$

Defining ω as $(g_0/a)^{1/2}$, $\Delta x = a\Delta\theta$, $\Delta\dot{x} = a\Delta\dot{\theta}$, the solution to the error equation is

$$\Delta x = \Delta x_0 \cos \omega t + \frac{\Delta\dot{x}_0}{\omega}\sin \omega t + a\epsilon_y\left(t - \frac{1}{\omega}\sin \omega t\right) + a\psi_{y0}(1 - \cos \omega t) + k_x\frac{v}{\omega}\sin \omega t + \frac{\delta A_x}{\omega^2}(1 - \cos \omega t) \ldots [29]$$

$$\Delta y = \Delta y_0 \cos \omega t + \frac{\Delta\dot{y}_0}{\omega}\sin \omega t + a\epsilon_z\left(\frac{a}{v}\sin\frac{vt}{a} - \frac{1}{\omega}\sin \omega t\right) - v\epsilon_z\left[\frac{a^2}{v^2}\left(1 - \cos\frac{vt}{a}\right) - \frac{1}{\omega^2}(1 - \cos \omega t)\right] + a\psi_{z0}\left(\cos\frac{vt}{a} - \cos \omega t\right) + a\psi_{x0}\sin\frac{vt}{a} + \frac{\delta A_y}{\omega^2}(1 - \cos \omega t) \ldots [30]$$

$$\phi_x = \psi_x = \psi_{x0}\cos\frac{vt}{a} - \psi_{z0}\sin\frac{vt}{a} + \frac{a\epsilon_x}{v}\sin\frac{vt}{a} - \frac{a\epsilon_z}{v}\left(1 - \cos\frac{vt}{a}\right) \ldots [31]$$

$$\psi_y = \psi_{y0} + \epsilon_y t \ldots\ldots\ldots\ldots\ldots\ldots [32]$$

$$\phi_z = \psi_z = \psi_{z0}\cos\frac{vt}{a} + \psi_{x0}\sin\frac{vt}{a} + \frac{a\epsilon_z}{v}\sin\frac{vt}{a} + \frac{a\epsilon_x}{v}\left(1 - \cos\frac{vt}{a}\right) \ldots [33]$$

$$\phi_y = \frac{\Delta x_0}{a}\cos \omega t + \left(\frac{\Delta\dot{x}_0}{a\omega} - \frac{\epsilon_y}{\omega}\right)\sin \omega t + \psi_{y0}\cos \omega t + k_x\frac{v}{a\omega}\sin \omega t + \frac{\delta A_x}{g}(1 - \cos \omega t) \ldots [34]$$

It is straightforward to obtain the error from any particular source by substitution in these equations. The general characteristics of some of these errors are probably of more interest than the exact form.

1 *Position errors.* In general the position errors are sinusoidal in form with oscillations having the characteristic 84 min period. Acceleration impulse errors lead to oscillations about zero; acceleration bias errors give rise to oscillations about an offset position error equal to the product of the radius of the earth and the ratio of the acceleration error to the acceleration of gravity; gyro drift produces an error increasing with time which oscillates about a value equal to the product of the radius of the earth and the angle through which the gyro has drifted.

The extreme precision required of both accelerometers and gyroscopes is made apparent by the presence of the large quantity a, the radius of the earth, as a factor. It should be noted, however, that the error is always less, and for large times very much less, than an error of the form $1/2\ (\delta A)t^2$ which might have been expected.

2 *Platform alignment errors.* For some applications, platform error angles are of considerable interest in themselves. It should be noted that gyro drift produces oscillatory platform errors rather than ones which increase continuously with time as might be expected.

The extension of this analysis to include other important sources of error can be made using these same techniques. In some cases the results are quite obvious. For example, a bias error δC in the first integrator produces oscillatory errors of exactly the same form as the acceleration bias error δA. It has been stated that a system involving the double integration of acceleration, such as that considered here, is subject to position errors increasing parabolically with time from computer bias errors and that the mechanical complexity of a "five-gimbal" system is required if high accuracy over long time is to be achieved. This conclusion was apparently reached based upon a system in which the integrators for each channel were repeated, once to determine the feedback terms and again for indicating position. The above analysis and confirming system results show that it is not true for the case considered here.

Conclusion

As might be expected, the sources of error in inertial guidance are seen to be exclusively of dynamical or of trigonometrical nature, as distinguished from such sources of error as refraction of radiant energy, distortion of magnetic fields, etc. This fact leads to the supposition—borne out so far by experiment—that improvements in inertial instruments, in accuracy of initial alignments, etc., will pay off directly in enhanced guidance accuracy, without any foreseeable limit. In general, the gyroscope presents the more formidable problem, since defects thereof can result in cumulative position error; defects associated with accelerometers and integrators can usually be caused to result merely in bounded errors, due to the oscillatory nature of the error functions. In general, also, the nature of errors, in a properly designed inertial guidance system using the same basic components, is largely independent of the particular mode of mechanization or system of coordinates used. A similar analysis to that given here can

be carried out for any practical coordinate system including effects of earth rotation and ellipticity with only additional algebraic complications. The results are essentially the same.

In using these results, statistical averages are often important. In some cases RMS time averages of the trigonometric functions are often used. More exact solutions of the error equations can also be obtained by considering the error sources to be stochastic variables and obtaining by noise theory expressions for ensemble averages.

References

1 Clemens, John E., "Mechanics in Navigation," in "The Sciences in Navigation" (Symposium of papers presented at the Seventh Annual National Meeting of the Institute of Navigation, June 28–29, 1951, New York), Institute of Navigation, University of California, 1951, p. 13.

2 Slater, J. M., Duncan, D. B., "Inertial Navigation," *Aeronautical Engineering Review*, vol. 15, no. 1, Jan. 1956, p. 344.

3 Slater, J. M., "Choice of Coordinate Systems in Inertial Navigation," *Navigation*, vol. 5, no. 2, June 1956.

4 Wrigley, W., "Schuler Tuning Characteristics on Navigational Instruments," *Navigation*, vol. 2, no. 8, Dec. 1950, pp. 282–290.

5 Slater, J. M. "Measurement and Integration of Acceleration in Inertial Navigation," ASME Preprint 56-A-160, Nov. 1956.

6 Draper, C. S., Wrigley, W., Grohe, L. R., "The Floating Integrating Gyro and its Application to Geometrical Stabilization Problems on Moving Bases," *Aeronautical Engineering Review*, vol. 15, no. 6, June 1956, p. 46.

7 Wrigley, W., Woodbury, R. B., Hovorka, J., "Inertial Guidance," Institute of Aeronautical Sciences, Reprint 698, Jan. 1957.

8 Schuler, M., "Die Storing Von Pendel und Kreiselapparaten durch die Beschleunigung der Fahrzeuges," *Physikalische Zeitschrift*, vol. 24, 1923, p. 344.

Technical Notes

Bore-Surface Temperature Variation During Rapid Firing of a 40-mm Gun

W. H. GIEDT[1] AND D. L. RALL[2]

Detroit Controls, Redwood City, Calif.

Experimental bore-surface and inwall temperature measurements at five locations along a 40-mm gun barrel during a burst firing of eight rounds are presented. Values for heat transfer from the propellant gases to the barrel were calculated as described in a previous paper (1).[3] Results indicate that heat flow into the barrel is essentially complete about 120 millisec after ignition, and heat flow out before the firing of the subsequent round is negligible. The total heat transfer per round decreases with each succeeding round in a burst. An approximate analysis is made, the results of which describe this decrease in terms of a simple power function. Use of this power function to estimate the minimum surface temperature between rounds is also demonstrated.

Introduction

During rapid fire of an automatic gun, heating of the barrel by hot propellant gases is a very severe problem. It is well known that an extended burst will cause the bore-surface temperature to reach the melting point of the gun metal, and severe erosion will occur. In addition to this effect, distortion of the barrel, structural weakening of the gun components and the danger of auto-ignition of ammunition ("cook-off") may result. Although consideration is given to these effects in gun design, incomplete knowledge of heat transfer phenomena makes it almost impossible to proceed with complete confidence.

The recent development of surface thermocouples (1–2), has provided a very useful tool for studying this problem.

Received Aug. 5, 1957.

[1] Senior Research Engineer, Research Department, Detroit Controls Div. of American Standard. Associate Professor of Mechanical Engineering, University of California, Berkeley.

[2] Research Engineer, Research Department, Detroit Controls Div. of American Standard.

[3] Numbers in parentheses indicate References at end of paper.

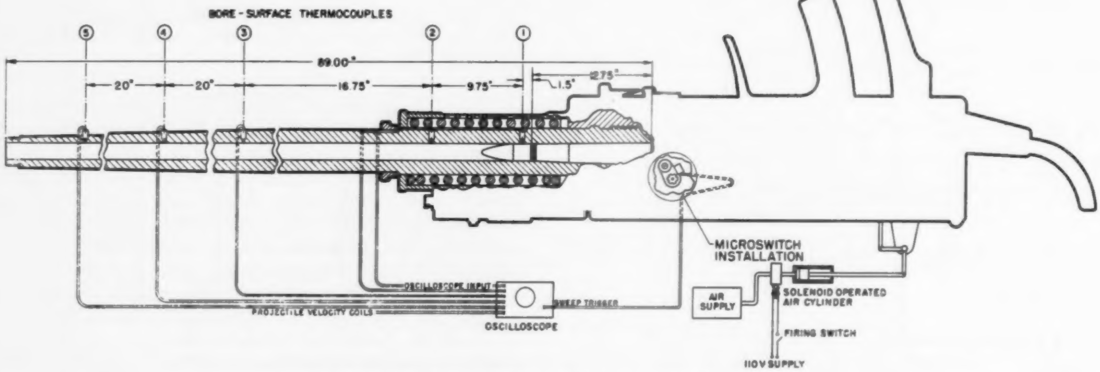

Fig. 1 Instrumentation of 40-mm automatic gun

Editor's Note: This section of Jet Propulsion is open to short manuscripts describing new developments or offering comments on papers previously published. Such manuscripts are published without editorial review, usually within two months of the date of receipt. Requirements as to style are the same as for regular contributions (see masthead page of this issue).

Such devices were utilized in the work described herein[4] to measure the bore-surface temperature variation during burst firings in a 40-mm rifled-barrel gun. The nature of the heat transfer variation was then investigated, using these records in conjunction with simultaneous inwall (barrel) temperature records.

Experimental Equipment and Procedure

40-mm Automatic Gun Instrumentation

A standard antiaircraft gun was instrumented, as shown in Fig. 1, with five bore-surface thermocouples along the barrel. These units indicate the temperature variation at the interface between a thin plated layer of nickel and the barrel steel at a distance of approximately 0.0002 in. below the bore surface. To supplement bore-surface temperature measurements, an inwall thermocouple was installed a depth of 0.038 in. from the bore surface and displaced 90 deg circumferentially from the No. 3 surface thermocouple. The junction was formed by percussion-welding an insulated 0.020-in.-diam constantan wire to the bottom of a small hole drilled radially into the barrel. A thin layer of insulation on the wire was provided by oxidizing it in a low temperature flame.

The outputs of the five surface thermocouples were indicated by a Maryland Electronics Corporation six-channel oscillograph and recorded by a 35-mm strip-film drum camera. The output from the inwall thermocouple was registered on a Sanborn recorder. Velocities were determined by using magnetized projectiles together with two appropriately spaced magnetic pick-up coils.

Experimental Results

Bore-surface temperature records were obtained during an 8-round burst (890-gm projectiles with a 293-gm charge of SPDN 7184 propellant, fired at the rate of 115 rounds per min). Inwall temperatures were also recorded 0.038 in. from the bore surface at the No. 3 thermocouple location.

An approximate transcription of these bore-surface and inwall temperature variations at the No. 3 location, showing the maximum and minimum values, is presented in Fig. 2. Although a general increasing trend is apparent, a rather large variation in maximum temperature occurred, a fact that can be attributed to differences in the burning of individual rounds. The minimum between-round bore-surface and inwall temperatures, on the other hand, rise consistently, since they depend on the total heat transferred to the barrel with each round, which is not so markedly influenced by variations from round to round as is the peak temperature.

Fig. 3 shows the distribution of the maximum and minimum bore-surface temperatures along the barrel measured during the firing. Attention is called to the results for Round No. 1 to emphasize the extent of burning variation that can occur. It appears that burning was retarded initially, resulting in a maximum bore-surface temperature of only 430 C at the No. 1 thermocouple location (as compared to around 900 C for successive rounds), and higher temperatures at the No. 2 and 3 locations. It is interesting that in spite of the apparent combustion variation, the muzzle velocity was only slightly lower than for the other rounds. Fig. 2 also emphasizes the significantly higher surface temperatures reached in the region near the origin of rifling. This is the primary reason for the high erosion rates observed in this area.

Thermal Properties Based on Comparative Study of Bore-Surface and Inwall Temperature Measurements

It is generally permissible, in heat transfer calculations, to consider a gun barrel as a semi-infinite solid and to neglect heat conduction parallel to the bore surface. Temperature variation with time at planes of the order of several hundredths of an inch from the surface can be satisfactorily approximated by assuming that the heat transfer from the propellant gas occurs instantaneously as a pulse of heat, Q (3). With average values for the thermal constants assumed, the temperature variation is given for this case by

$$T = \frac{Q}{\sqrt{\pi \rho c k t}} e^{-x^2/4\alpha t} \qquad [1]$$

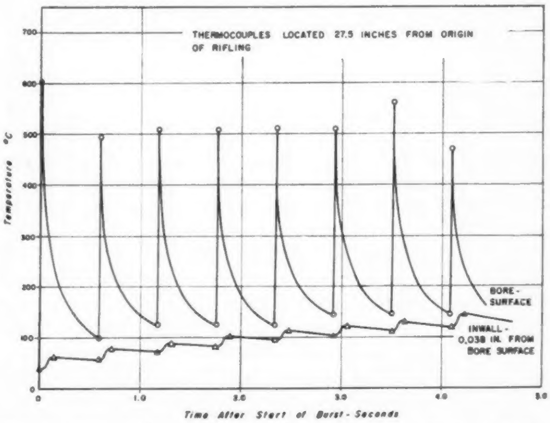

Fig. 2 Bore-surface and inwall temperature variations during 8-round burst in a 40-mm gun (maximum and minimum temperatures indicated)

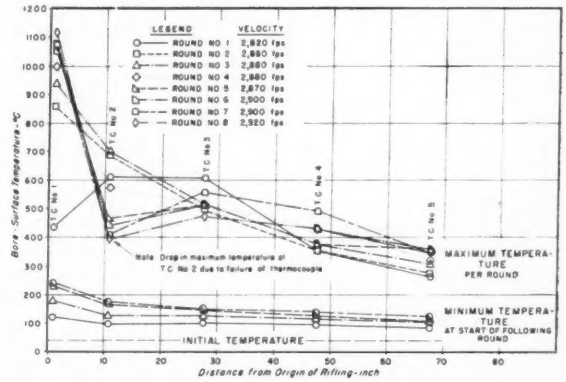

Fig. 3 Maximum and minimum bore-surface temperature distribution along a rifled 40-mm barrel during an 8-round burst

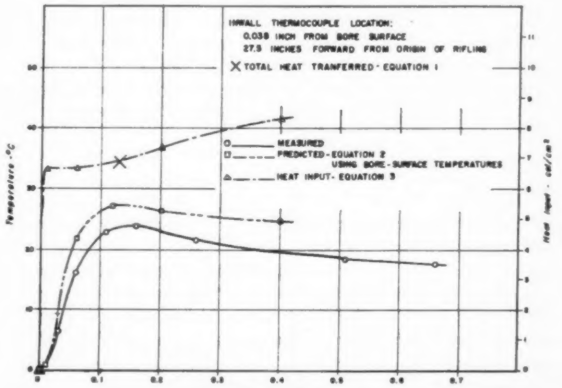

Fig. 4 Inwall temperature variation vs. time during first round of an 8-round burst in a 40-mm gun

[4] Performed for the Bureau of Ordnance of the U. S. Department of the Navy under Task II of Contract NOrd 12102. Their interest in and approval of its presentation are gratefully acknowledged.

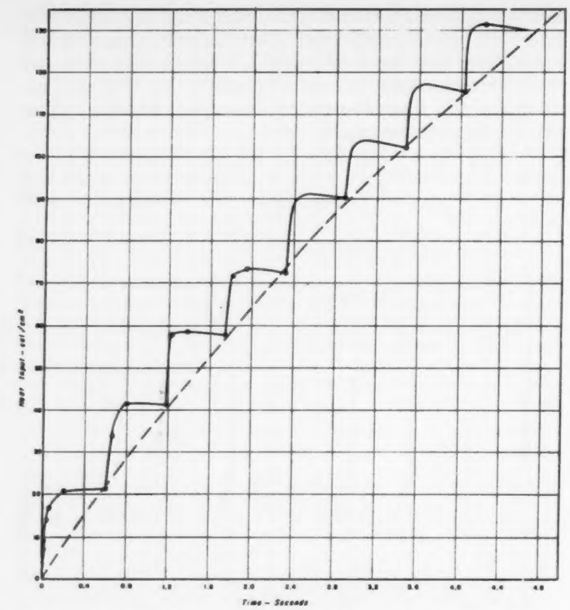

Fig. 5 Heat transfer to a 40-mm gun barrel $1^1/_2$ in. from origin of rifling during an 8-round burst

Note that if the temperature T at any time t and distance from the bore surface x is measured, this equation can be used to calculate the total heat transfer Q (per unit area) assuming average values for the density (ρ), specific heat (c), thermal conductivity (k), and thermal diffusivity (α).

A more precise expression for the temperature variation with time and distance is (3)

$$T(x, t) = \frac{x}{2\sqrt{\pi\alpha}} \int_0^t \frac{\phi(\lambda) e^{-x^2/4\alpha(t-\lambda)}\, d\lambda}{(t - \lambda)^{3/2}} \qquad [2]$$

where the function $\phi(\lambda)$ represents the temperature variation with time at the bore surface, λ being the time variable of integration. This equation is applicable for all values of x. By differentiation of Equation [2] with respect to x and integration with respect to time at $x = 0$, the heat transfer up to any time t is found to be (1)

$$Q(t) = \frac{k}{\sqrt{\pi\alpha}} \int_0^t \frac{\phi(\lambda)d\lambda}{(t - \lambda)^{1/2}} \qquad [3]$$

In using any of the above equations, it is necessary to know the appropriate values of the thermal conductivity (k) and diffusivity (α). Fortunately, an effective value of α can be determined from a measured inwall temperature record and Equation [1]. Differentiating this equation with respect to time and equating the result to zero gives the time at which the temperature at any distance x reaches a maximum as

$$t_{T = \max} = \frac{x^2}{2\alpha} \qquad [4]$$

By using this expression, a value for $\alpha = 0.0352$ cm²/sec was determined.

A check on the validity of this result was possible by using it in Equation [2] along with the measured surface-temperature history to predict the temperature variation at the location of the inwall thermocouple. This result is compared in Fig. 4 with the experimental curve. The agreement was regarded as reasonably satisfactory, being within about 10 per cent at the maximum temperature point. Slight adjustments in the value of α did not yield improved results, suggesting that variations with temperature or possibly other factors may be involved.

For calculation of the total heat transfer to the barrel, an average value of k (0.0500 cal/sec-cm-C) was determined from the above value of α, using values of $\rho = 7.85$ gm/cm³ and $c = 0.181$ cal/gm-C (4) . Substituting these values and the experimental data at the time of maximum inwall temperature in Equation [1] gave

$$Q = 6.8 \text{ cal/cm}^2 \quad \text{(at No. 3 thermocouple location)}$$

An alternative calculation using Equation [3], and substituting the experimental surface temperature variation, yielded a value of

$$Q = 6.9 \text{ cal/cm}^2$$

It is significant to note that the effective value of thermal conductivity determined and nominally confirmed by the above calculations is only of the order of 60 per cent of that indicated for the barrel metal in the literature (4). This difference may be due to material variations but is more likely attributable to the altered metal layer which is eventually formed at the bore surface by the combined chemical and thermal effects of the hot propellant gases.

Heat Transfer During Rapid Fire

To investigate the nature of the surface heat transfer variation with time during a burst firing, measured temperatures at the No. 1 thermocouple location ($1\frac{1}{2}$ in. from the origin of rifling) were substituted in Equation [3] and the integration carried out numerically. Average values of k and α (0.050 cal/sec-cm-C and 0.0352 cm²/sec, respectively), determined as described above, were used. The results have been plotted in Fig. 5, where it is shown that heat from the propellant gas flows to the barrel for a period of from 0.1 to 0.2 sec after a round has been fired. The heat rate decreases very rapidly, however, so that most of the transfer occurs soon after the firing. Thus, the curve has the appearance of a series of steps. The amount of heat transfer per round can be clearly observed to decrease with each successive round in the burst, and after the second round some reverse flow actually occurs.

Prediction of Minimum Surface Temperature

Since it may be of interest to know what the bore- and combustion-chamber surface temperatures will be near the beginning of any round in a burst (to estimate danger of cook-off), consideration was given to using the information in Fig. 5 to predict values for these temperatures. It was first noted that if the bore-surface temperature variation $\phi(t)$ is unknown and $Q(t)$ is known, expression [3] may be regarded as an Abel integral equation. Its solution (5)is

$$\phi(t) = \frac{\sin \nu\pi}{\pi} \frac{d}{dt} \int_0^t \frac{Q(\lambda)}{(t - \lambda)^{1-\nu}}\, d\lambda \quad (0 < \nu < 1) \qquad [5]$$

where ν is the exponent of $(t - \lambda)$ in the denominator of the integrand of Equation [3]. With interest focused on the surface temperature just before the firing of each round, the possibility of approximating $Q(t)$ by a simple power function of t was investigated. Because of the decreasing heat transfer per round in a burst, an expression of the form

$$Q(t) = Ct^n \qquad [6]$$

with $n < 1$, was found to give a curve passing through the points on the actual curve corresponding to the firing of each round (the dashed curve in Fig. 5). The surface temperature variation resulting from a heat input in accordance with Equation [6] might therefore be expected to coincide with the actual surface temperature just prior to the firing of each round.

If the expression for Q given by [6] is substituted in [5] and the integrand expanded in a series, integration yields

$$\phi(t) = \frac{C}{k}\sqrt{\frac{\alpha}{\pi}}\left(n + \frac{1}{2}\right)t^{n-1/2} \times \left[2 - \frac{2n}{3} + \frac{(n^2 - n)}{5} - \frac{(n^3 - 3n^2 + 2n)}{21} + \ldots\right] \ldots [7]$$

For values of $n < 1$, this series converges rapidly. Use of only the four terms indicated was estimated to give an error of less than 3 per cent.

The applicable values of C and n were determined from a log-log plot of heat transferred per round vs. round number. The equation of the curve through the experimental points for the No. 1 thermocouple location was found to be

$$Q(t) = KN^n \ldots\ldots\ldots\ldots [8]$$

where K is the heat transferred during the first round (23 cal/cm²), N the round number, and the exponent $n = 0.837$. If R denotes the rate of fire, $N = Rt$, and Equation [8] becomes

$$Q(t) = KR^n t^n = 23R^{0.837}t^{0.837} = Ct^n \ldots\ldots [9]$$

The rise in bore-surface temperature is then

$$T_s = \phi(t) = 24.4\frac{\sqrt{\alpha}}{k}R^{0.837}t^{0.837} \ldots\ldots [10]$$

The bore-surface temperature at the No. 1 thermocouple location at the end of the 8-round burst, as calculated from Equation [10] was approximately 15 per cent higher than the experimentally observed value. In view of the assumptions involved, this sort of agreement may be regarded as satisfactory.

In applying Equation [10] to other locations along the barrel, the appropriate value for the heat input during the first round (K) must of course be used. Exponent n (Equation [8]) would, however, be expected to depend primarily on the thermal properties of the barrel and should be reasonably constant for a given gun. A limited check on this hypothesis was obtained by substituting the value of K = 8.3 cal/cm² determined for the No. 3 thermocouple location in Equation [10], using the value of n found for the No. 1 location. This yielded a value of 140 C at the end of the 8-round burst, which compares very favorably with the measured value of 136 C. An additional check was made using the bore-surface and in-wall temperature data given in (2) for a 5-round burst in a 0.50 caliber machine gun. Agreement between predicted and observed results was also within 15 per cent.

References

1 Giedt, W. H., "The Determination of Transient Temperatures and Heat Transfer at a Gas-Metal Interface Applied to a 40-mm Gun Barrel," JET PROPULSION, vol. 25, April 1955, p. 158.

2 Willman, B. T., et al., "Measurement of Gun Barrel Temperature," *Instruments and Automation*, vol. 28, Jan. 1955, p. 106.

3 Carslaw, H. S., and Jaeger, J. C., "Conduction of Heat in Solids," Clarendon Press, Oxford, 1947.

4 "Metals Handbook," ASM, Cleveland, Ohio.

5 Pipes, Louis A., "Applied Mathematics for Engineers and Physicists," McGraw-Hill, New York, 1946, p. 555.

Effect of Radical Recombination Kinetics on Specific Impulse of High Temperature Systems

KENNETH A. WILDE[1]

Rohm & Haas Company, Huntsville, Ala.

Received June 21, 1957.

[1] Research Chemist, Redstone Arsenal Research Division.

The effect of extent of completion of a radical recombination reaction on the specific impulse of a simple system has been considered. The *kinetic* impulse between the two conventional limiting conditions of frozen and equilibrium flow has been obtained as a function of recombination rate constant, chamber pressure and motor diameter. The most recent data (obtained from shock tube measurements up to 2800 K) on recombination rate constants are used. These values are smaller by a factor of 10²–10³ than those previously considered in this connection. For the best value of the rate constant, 20–80 per cent of the difference between frozen and equilibrium flow is realized, depending on the motor size and chamber pressure.

IN CONVENTIONAL propellant thermochemical calculations, specific impulses are cited for both frozen and equilibrium flow. These are the two limiting conditions, corresponding to zero and infinite reaction rates, respectively, in the nozzle expansion. Chemical rate constants are, of course, never either zero or infinite and the true *kinetic* impulse must lie between the two limiting conditions. Penner and Altman have given this problem extensive consideration and have derived approximate criteria for the realization of near-frozen and near-equilibrium flow (1).[2] It appears desirable to study the actual kinetic impulse as a function of rocket and kinetic parameters for a simple model. Krieger (2) has carried out an exact numerical solution of hydrogen gas expanding in a nozzle, starting at 3500 K (about 12 per cent dissociation), for a particular set of conditions. He found that about 85 per cent of the difference between frozen and equilibrium flow was realized for a motor diameter of 10 cm, a recombination rate constant of 10¹⁰liter²/mole² sec, and a chamber pressure of 300 psi.

Another use for this study of nozzle kinetics is the observation of the effect of the new data on recombination rate constants (3–5). Penner and Krieger used recombination rate constants in the range 10¹⁰-10¹¹liter²/mole² sec, which were derived from rather old room-temperature data. The later values (for recombination of iodine and bromine) were obtained in a shock tube up to 2800 K, and were not only smaller than previous values, but also showed a decrease with temperature.

The present precision of the data is only sufficient to indicate that the rate constant is inversely proportional to the first or perhaps three-halves power of the temperature. A number of rudimentary theoretical treatments of the recombination problem have been made (6–8), generally indicating an inverse one-half power dependence of rate constant with temperature. Recombination rates are larger for larger third bodies, such as benzene, but only small molecules and atoms are available at flame temperatures. All things considered, the best order of magnitude of atomic recombination rate constants under nozzle conditions (2000–3000 K) now appears to be 10⁸liter²/mole² sec, a factor of 10²-10³ smaller than previously thought.

Even if we restrict the problem to a single recombination reaction and make other noncritical simplifications, such as constant heat capacities and zero chamber velocity, a numerical solution is still necessary. An approximate closed analytical solution can be obtained if, following Penner, we use a constant average value of the cooling rate in the nozzle, $-dT/dt$. The result for the true *kinetic* impulse should still reflect the variation with the three parameters under study: Rate constant, chamber pressure and motor diameter. In order to find the true impulse we must find the gas composition at T_e, the exhaust temperature; that is, we must assess the extent to which reaction [1] proceeds

$$2R + X \underset{k_b}{\overset{k_f}{\rightleftharpoons}} R_2 + X \ldots\ldots\ldots\ldots [1]$$

[2] Numbers in parentheses indicate References at end of paper.

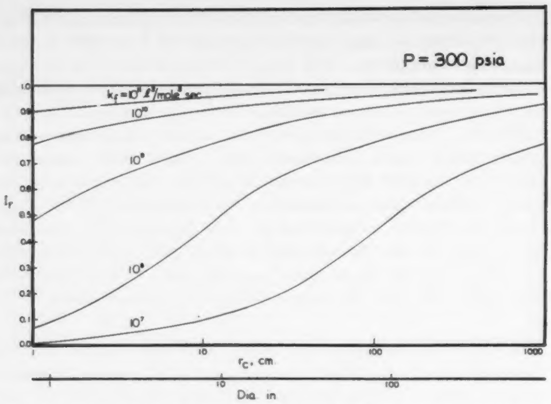

Fig. 1 The variation of I_r with recombination rate constant and motor diameter at 300 psi

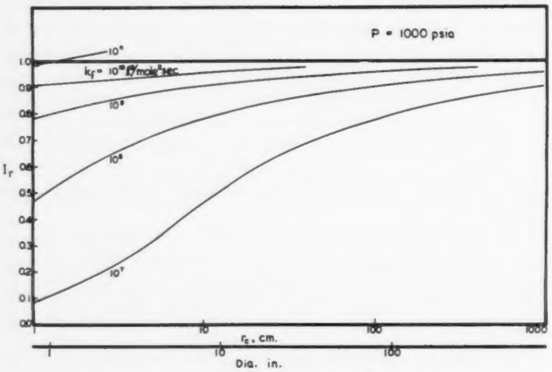

Fig. 2 The variation of I_r with recombination rate constant and motor diameter at 1000 psi

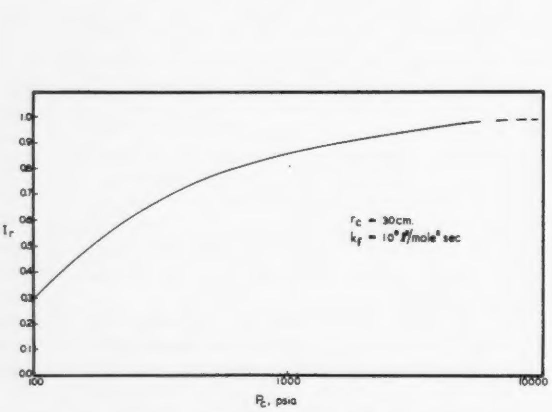

Fig. 3 The variation of I_r with chamber pressure

where R is a radical or atom, X is a third body, and k_f and k_b are the forward and back rate constants, respectively. The parameters which are fixed at typical values in this study are

T_c = 3500° K
P_e/P_c = 1/68
v_c $\cong$ chamber velocity = zero
D_0 = dissociation energy of R_2 = 100 kcal
y_c = mole fraction radicals at T_c = 0.10
ΔS_1 = −23 cal/mole° K
C_p = 8 cal/mole° K

The general plan of approach is to find the exhaust temperature and composition from the constant entropy condition and the relation provided by the kinetics of reaction [1]. The specific impulses for frozen, equilibrium and kinetic flow are then calculated by standard formulas. The dependent variable will be a reduced impulse I_r defined as

$$I_r = \frac{I_{\text{true}} - I_{\text{frozen}}}{I_{\text{equil}} - I_{\text{frozen}}} \qquad [2]$$

which expresses the fractional difference realized between frozen and equilibrium flow. Thus, when $y_c = y_e$ (frozen flow), $I_r = 0$; and when $y_c \gg y_e$ (equilibrium flow), $I_r = 1$. A plot of I_r vs. $y_c - y_e$ is nearly linear.

Returning to the kinetic problem, the time rate of change of concentration of R is given by (1)

$$-\frac{dR}{dt} = \frac{-R}{(\gamma - 1)T}\frac{dT}{dt} + 2k_fR^2X\left[1 - \frac{R_2}{R^2K_c}\right] \qquad [3]$$

where R, R_2, and X are the concentrations of the respective species in mole/cc, $K_c = k_f/k_b = R_gTK_p$ is a concentration equilibrium constant and γ is a suitable mean heat capacity ratio. The first term on the right expresses the change in R due to expansion. It disappears when Equation [3] is transformed to mole fractions

$$\frac{-dy}{dt} = \frac{2k_f}{R_g^2T^2}\left[y^2p^2 - \frac{(1 - y)}{K_p}P\right] \qquad [4]$$

Equation [4] may be solved analytically by using certain approximations which are at least as good as the assumption of a constant average cooling rate. The details will not be given here, but the result is an equation relating exhaust temperature and composition. With the aid of Equation [1] the results in Figs. 1, 2 and 3 were derived.

An inspection of the figures shows that with the new order of magnitude of the recombination rate constant k_f (10^8) the recombination is not complete, but that 20–80 per cent of the difference between frozen and equilibrium flow is realized, depending on the parameters. For example, with a motor diameter of 60 cm and a recombination rate constant of 10^8, 67 per cent of the difference in impulse between equilibrium and frozen flow will be realized at 300-psi pressure and 86 per cent will be realized at 1000-psi pressure. However, if the recombination rate constant is 10^7, only 20 per cent of the difference in impulse will be realized at 300-psi and 65 per cent at 1000-psi pressure.

References

1 Penner, S. S., "Chemical Reactions in Flow Systems," Butterworths Scientific Publications, London, 1955.

2 Krieger, F. J., "Chemical Kinetics and Rocket Nozzle Design," *Journal of the American Rocket Society*, vol. 21, 1951, p. 179.

3 Britton, D., Davidson, N., and Schott, G., "The Rate of Dissociation of Molecular Iodine," *Disc. Faraday Society*, vol. 17, 1954, p. 58.

4 Britton, D., and Davidson, N., "Rate Dissociation of Molecular Bromine," *Journal of Chemical Physics*, vol. 25, 1956, p. 810.

5 Palmer, H. B., and Hornig, D. F., "Rate of Dissociation of Bromine in Shock Waves," *Journal of Chemical Physics*, vol. 26, 1957, p. 98.

6 Wigner, E. P., "Calculation of Rates of Elementary Association Reactions," *Journal of Chemical Physics*, vol. 5, 1937, p. 720.

7 Rice, O. K., "On Recombination of Iodine and Bromine Atoms," *Journal of Chemical Physics*, vol. 9, 1941, p. 258.

8 Careri, G., "Rate of Recombination of Free Atoms," *Journal of Chemical Physics*, vol. 21, 1953, p. 749.

Transfer Between Vehicles in Circular Orbits

BERNARD H. PAIEWONSKY[1]

Wright Air Development Center, Ohio

Nomenclature

A = initial vehicle
B = terminal vehicle
γ = gravitational constant
M_e = mass of the earth
R_A = radius of circular orbit of vehicle A
R_B = radius of circular orbit of vehicle B
ω_A = angular velocity of A
ω_B = angular velocity of B
τ_H = time of flight in Hohmann orbit
T_H = period of Hohmann orbit
θ = central angle between vehicles A and B

Angles *ABCDE:*

Angle *D:* angle between true vertical and horizon as seen by vehicle A
Angle *E:* angle between horizon and terminal vehicle as seen by initial vehicle A
Angle E_0: angle E at time of launch

Introduction

THE purpose of this investigation is to examine the orbital transfer of a commuter vehicle between two co-planar satellites. Suppose we wish to go from one satellite vehicle to another by means of a commuter rocket using chemical propellants. In order to conserve fuel, an orbit requiring the minimum expenditure of impulse should be sought. The optimum paths for transfer between circular orbits have been found by Hohmann (1)[2] to consist of the family of cotangential ellipses. In practice, it will usually be necessary to go from one vehicle to another, rather than merely changing orbits. In order to do this without applying corrective thrust in flight, the launching of the commuter rocket from the initial orbit must be timed so that the commuter arrives at the terminal orbit coincident with the second orbital vehicle. D. F. Lawden (2, 3) has derived in general terms the equations for orbital transfer between two planets. This note presents a simple approach to the restricted case of co-planar satellites in concentric circular orbits.

Transfer Between Satellite Vehicles

The analysis presented here considers only Hohmann transfer orbits requiring minimum expenditure of fuel. In order to use a Hohmann orbit (a cotangential ellipse) there is a definite angular relation that must exist between the initial and terminal vehicles. This relationship is based on the requirement that the orbital vehicle and the commuting vehicle meet. A lead-collision calculation is required.

Let vehicle A be the initial vehicle and let vehicle B be the terminal vehicle. For convenience, assume a geocentric polar coordinate system (r, θ) with $\theta = 0$ taken through the initial vehicle at time $t = 0$. Let R_A, R_B be radii of orbits of vehicles A and B respectively. The case of $R_A = R_B$ will not be considered. The angular velocities ω_A and ω_B of the satellites in these orbits are given by

$$\left.\begin{aligned} \omega_A &= \sqrt{\gamma M_e}\quad R_A{}^{-3/2} \\ \omega_B &= \sqrt{\gamma M_e}\quad R_B{}^{-3/2} \end{aligned}\right\} \qquad [1]$$

The time of flight, τ_H in the Hohmann orbit, from apogee to perigee is given by half the period, T_H, of the Hohmann orbit.

$$\tau_H = \frac{T_H}{2} = \frac{1}{2}\frac{2\pi}{\sqrt{\gamma M_e}}\left[\frac{R_A + R_B}{2}\right]^{3/2} \qquad [2]$$

where $(R_A + R_B)/2$ is the semimajor axis of the orbit of transfer (4).

The commuter vehicle will reach the terminal orbit at $\theta = \pi$. The problem now is to find a position of vehicle B at the time of launch such that the commuter vehicle from A will meet it at $\theta = \pi$. In the time t, vehicle B has gone an angular distance $\Delta\theta$ given by

$$\Delta\theta_B = \omega_B t$$

where $\Delta\theta_B$ is taken congruent modulo 2π.[3]

From Equation [2] we know that

$$\tau_H = \left[\frac{R_A + R_B}{2}\right]^{3/2} \cdot \frac{\pi}{\sqrt{\gamma M_e}}$$

Thus

$$\Delta\theta_B = \sqrt{\gamma M_e}\quad R_B{}^{-3/2}\frac{\pi}{\sqrt{\gamma M_e}}\left[\frac{R_A + R_B}{2}\right]^{3/2}$$

$$= \pi\left[\frac{R_A + R_B}{2R_B}\right]^{3/2} \qquad [3]$$

The angular location $(\theta_B)_{t=0}$ of vehicle B at $t = 0$ can be found by subtracting $\Delta\theta_B$ from π.

$$(\theta_B)_{t=0} = \pi - \Delta\theta_B = \pi\left(1 - \left[\frac{R_A + R_B}{2R_B}\right]^{3/2}\right) \qquad [4]$$

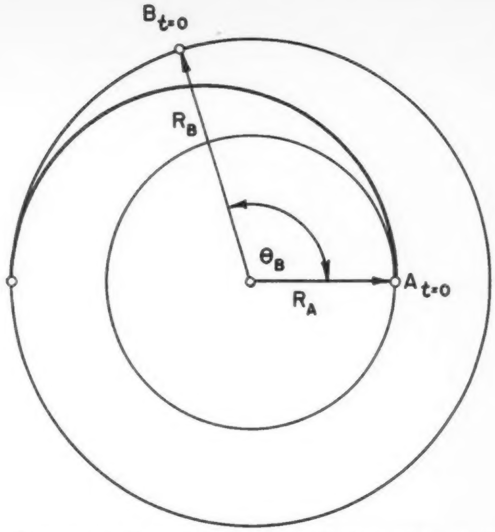

Fig. 1 Hohmann orbit showing positions of initial and terminal vehicles

The geometry of the maneuver is shown in Fig. 1.

If we wish to go from an outer orbit to an inner orbit and if R_B is very much greater than R_A, we must take $\Delta\theta$ congruent modulo 2π and count the number of revolutions of the vehicle in the inner orbit. That is, if the time of transfer exceeds the period of the inner or terminal vehicle, integral multiples of the period must be subtracted from the transfer time. The remainder t is then used to compute $\Delta\theta$ and to determine the

---

Received July 15, 1957.

[1] Aeronautical Research Engineer, Flight Control Laboratory; now at Princeton University. Mem. ARS.

[2] Numbers in parentheses indicate References at end of paper.

[3] This means that integral multiples of 2π are subtracted from $\omega_B t$. The final remainder, $\Delta\theta_B$, is thus $< 2\pi$.

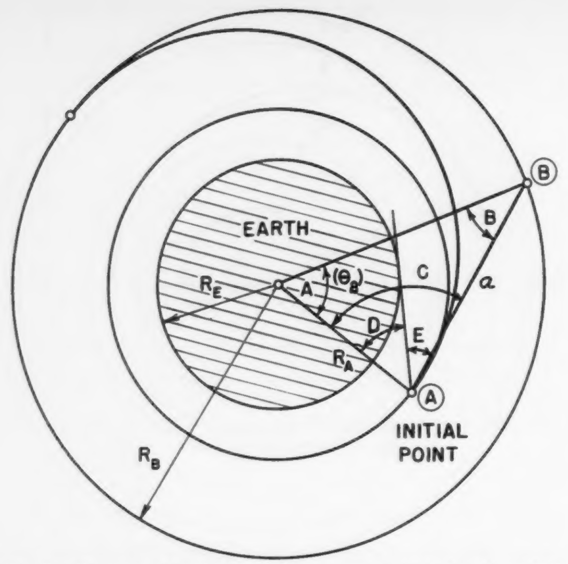

Fig. 2 Diagram of in-flight angular measurements (not to scale)

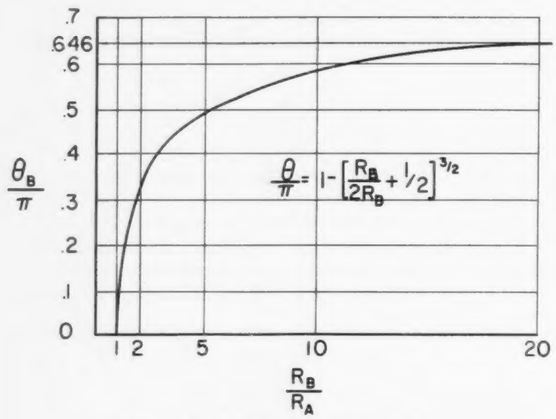

Fig. 3 Initial angle vs. radius ratio

proper initial angular relation between the two satellites at the time of launch from Equation [4].

In-Flight Determination of Angular Relationships Between Satellites

It will be necessary for the commuter rocket to know the angle between the terminal vehicle and the initial vehicle prior to launching. This information may be obtained by communication with an outside observer or by direct measurements. By means of measurements of the angle between the horizon and the terminal vehicle, and the known quantities, R_A, R_B, and $(\theta)_{t=0}$, the time to launch may be determined. It may happen that the required angular relationship between the vehicles is such that visual observations cannot be made. This method works only when there is an unobstructed line of sight between the observers. Fig. 2 illustrates the measurements required.

Formulas from elementary trigonometry provide the solution. The lettered angles are shown in Fig. 2.

$$\frac{a}{\text{Sin } A} = \frac{R_A}{\text{Sin } B} = \frac{R_B}{\text{Sin } C} = \frac{R_B}{\text{Sin } (D + E)}$$

when $A = \theta_{B\text{req.}}$

$$a = \sqrt{R_A^2 + R_B^2 - 2R_AR_B \cos \theta_B}$$

Let

$$K = \sin (D + E) = \frac{R_B \sin \theta_B}{\sqrt{R_A^2 + R_B^2 - 2R_AR_B \cos \theta_B}}$$

$$E = (\sin^{-1} K) - D$$

The value of angle E at the time of launch can be calculated and is called E_0.

When the angle between the horizon and the terminal vehicle is determined to be equal to E_0 the separation angle between the vehicles is the required θ_{AB} and the commuter rocket should be launched.[4]

The effects of errors in measurements and navigation are not considered in this paper although they certainly will be of importance in the practice of space travel.

Results

The relationship between θ_B and R_B/R_A is illustrated in Fig. 3. As R_B/R_A gets very large it is seen that θ_B/π approaches a maximum value of 0.646. Although the case $R_A = R_B$ was not considered in the derivation, the θ_B curve goes through zero when this occurs. This means that if the satellites have the same initial radii then they must coincide, otherwise one cannot travel between them using only one Hohmann orbit.

These results will now be applied to some problems. For a trip between two artificial earth satellites with radii $R_A = R_e + 500$ km and $R_B = R_e + 1000$ km, $R_e = 6370$ km. Fig. 3 shows $\theta_B = 9.08$ deg.

The conditions necessary at the start of a trip between a space station staging satellite and the moon are also obtained from Fig. 3. If the space station R_A is 7000 km from the earth's center and the moon is assumed to be in a circular orbit with radius $R_B = 3.88 \times 10^5$ km, then θ_B is found to be 115 deg. The time of flight for this trip is

$$\tau_H = \frac{\pi}{\sqrt{\gamma M}} \left[\frac{R_A + R_B}{2}\right]^{3/2} = 122 \text{ hours}$$

or a little over five days.

This method can also be used for rough calculations for interplanetary travel. Suppose we are planning a trip between the earth and mars, using chemical propellants. The elliptical planetary orbits are approximated by circular orbits about the sun.

$$R_A \text{ (earth)} = 1.41 \times 10^8 \text{ km}$$

$$R_B \text{ (mars)} = 2.28 \times 10^8 \text{ km}$$

The initial angle between the planets, θ_B, is seen to be nearly 45 deg. The time of flight for this journey is 264 days. The time of flight for this trip using 1-g acceleration has been computed by Jones (5) to be 2.08 days. The most economical flight path is not the shortest in time of travel.

A return trip from the Moon to the space station circling the earth may be examined using Equation [4]. Using the radii given in the previous example we can obtain θ_B' and $(\theta_A)_{t=0}$.

Let the staging vehicle be at a radius $R_A = 7000$ km. The moon is assumed to be at radius $R_B = 3.88 \times 10^5$ km.

$$\Delta\theta_B = \pi \left[\frac{R_A + R_B}{2R_A}\right]^{3/2} = 149.9\pi$$

$$\Delta\theta_B \equiv \Delta\theta'_B \text{ (mod } 2\pi)$$

$$\Delta\theta_B' = 0.93(2\pi) = 335.9°$$

$$(\theta_A)_{t=0} = \pi - \Delta\theta_B' = -155.9° \approx -156°$$

[4] It has been pointed out by a reviewer that the angle E_0 may correspond to two distinct values of θ_B in the case of transfer from a larger to a smaller orbit. A cure for this ambiguity is to measure the distance between vehicles A and B. The correct range has already been computed and is equal to a, with angle $A = \theta_{B\text{req.}}$

Another question may be raised at this point. Suppose vehicles A and B are initially in arbitrary positions with separation angle ϵ. How long must they wait to be in the proper position to use a Hohmann orbit? The delay is easily found to be

$$t_{\text{delay}} = \frac{\theta_{\text{req}} - \epsilon}{|\omega_A - \omega_B|}$$

The maximum time delay occurs if $(\theta_{\text{req}} - \epsilon) = 2\pi$. Thus

$$t_{\text{max delay}} = \frac{2\pi}{|\omega_A - \omega_B|}$$

Summary and Conclusions

A simple method is developed for calculating the angular relationship required between vehicles desiring to use Hohmann orbits for orbital transfer. This angular relationship is computed and is shown to depend only on the radius ratio of the orbits. A method is also presented for determining the relative angular positions of the satellites from in-flight measurements.

References

1 Hohmann, W., "Die Erreichbarkeit der Himmelskorper," R. Oldenbourg, Munich, 1925.

2 Lawden, D. F., *Journal of the British Interplanetary Society*, vol. 11, 1952, pp. 321 ff.

3 Lawden, D. F., "Transfer Between Circular Orbits," Jet Propulsion, vol. 26, July 1956, Part I, pp. 551–558.

4 Goldstein, H., "Classical Mechanics," Addison Wesley, 1953, pp. 79–80.

5 Jones, R. T., "Times for Interplanetary Trips," Jet Propulsion, vol,. 26, Feb. 1956 p. 102.

Some Observations of Flame Stabilization in Sudden Expansions

PETER A. ROSS[1]

Gas Dynamics Laboratory, Northwestern University, Evanston, Ill.

Introduction

PREMIXED flames stabilized by sudden expansions exhibit oscillatory burning within the region of stabilization when the length-to-diameter ratio of the chamber is large. An experimental study of such a configuration was conducted to determine the effects of the oscillatory combustion on the limits of stabilization. The results are presented herein for consideration.

Combustion instability as applied to afterburners has been studied previously by Rogers and Marble (1),[2] and Noreen and Kaskan (2). Although the proposed mechanisms are controversial, there seems to be general agreement that the oscillations are defined acoustically by the chamber geometry. The configuration under investigation exhibited an organ pipe type of oscillatory combustion in which the observed frequency corresponded to the longitudinal resonant frequency of the chamber.

The oscillatory combustion had relatively no effect on the lean limits, but had a large influence on the rich limits of stabilization.

Received Sept. 2, 1957.

[1] Phillips Petroleum Company Research Fellow in Gas Dynamics; now Research Assistant, Department of Mechanical Engineering, University of Wisconsin. Mem. ARS.

[2] Numbers in parentheses indicate References at end of paper.

Laboratory Work

A schematic diagram of the variable length sudden expansion combustion chamber used in this investigation is shown in Fig. 1. From this figure it is apparent that the desired variation in length is facilitated by the installation of a metallic plunger which can be positioned within the Vycor tube combustion chamber. The plunger is mounted by means of an O-ring and asbestos seal ring to prevent leakage and heat transfer within the annular cavity between the concentric cylindrical sections. Not shown in this figure are two 200-mesh screens placed upstream in the feed line to assure adequate mixing of the propane with the air. It is noted that the expansion ratio can be represented by the quotient A^2/B^2.

The frequency spectrum of the sound emitted from the exhaust is measured with a General Radio sound level meter and analyzer. The corresponding sound wave is determined from oscilloscopic recordings, the oscilloscope being used in the place of the analyzer in the primary measuring system. The wave shape is either saw-tooth sinusoidal or flat, depending on whether the burning is oscillatory or smooth. The frequencies obtained from the wave diagrams are in excellent agreement with those measured from the analyzer.

Qualitative Observations

Fig. 2 is a sketch of the various zones observed with a stable flame. The sharp increase in axial pressure near the sudden expansion (i.e., note flaring of the flame), along with the velocity gradient present at the jet interface, create a recirculation in the region around the mixing zone near the face of the plunger. As in the case of bluff body stabilization this recirculation zone provides the necessary ignition energy to the premixed fuel-air entering the mixing zone. The length of the flame decreases slightly with increasing Reynolds number, but is relatively insensitive to the length of the chamber. However, at any given approach velocity, the mixture strength greatly affects the length of the flame.

As the lean limit of combustion is approached, both the length and width of the flame decreases until, immediately prior to blowout, the flame appears as a faint brush around the jet. With rich blowout the length of the flame again decreases, but its width increases, filling the tube. Striations appear in the middle of the flame, extending upstream into the mixture jet; and the volume of the recirculation zone is

A	B	α
0.98	0.580	2.85
1.000	0.505	3.92

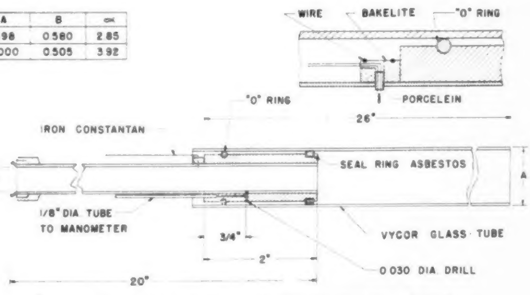

Fig. 1 Variable length sudden expansion chambers

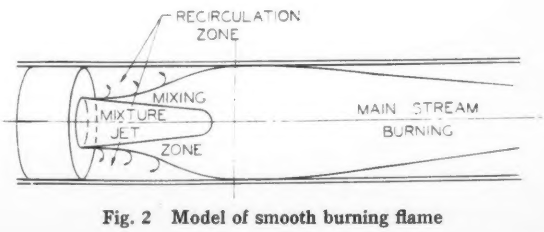

Fig. 2 Model of smooth burning flame

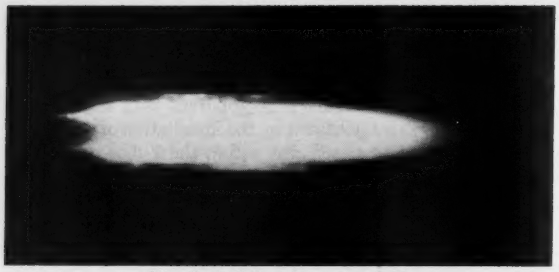

(a) Smooth burning; $\phi = 0.80$

(b) Oscillatory burning; $\phi = 1.20$

Fig. 3 Comparison of smooth burning with oscillatory burning; $V = 110$ fps, $L = 20$ in.

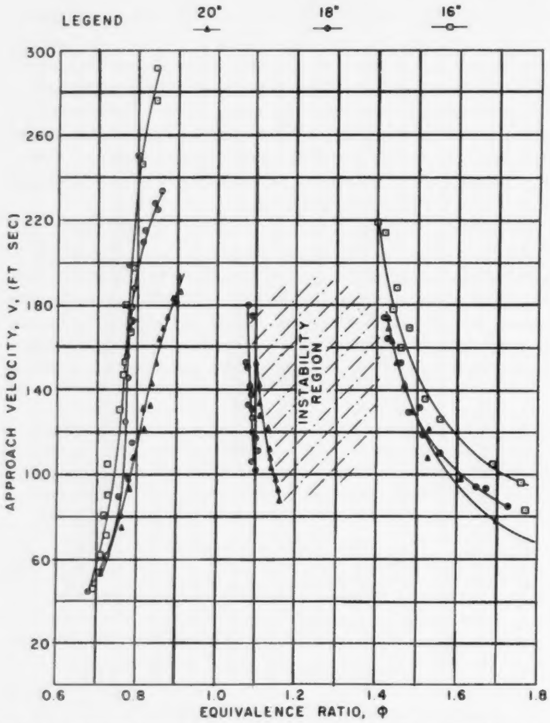

Fig. 4 Blowoff curves for a 16-, 18-, and 20-in.-length chamber with an expansion ratio of 3.92; limits of oscillatory burning for the 18- and 20-in. chamber

noticeably reduced. In this condition the flame blows off immediately with the incidence of any flame pulsations.

The flame photographs shown in Fig. 3 illustrate the change in the flame configuration which occurs with oscillatory combustion. The recirculation zone is no longer definable; the jet, previously sharply outlined, is now obscured; and the whole flame is pushed up against the face of the piston. Accompanying this change is a three- to fourfold increase in static pressure, indicating that flame blockage is significantly increased with the onset of oscillatory burning.

Results

The stability limits for the 16-, 18- and 20-in.-length chambers with expansion ratios of 3.92:1 are presented in Fig. 4. Also shown in the figure are the regions of oscillatory burning encountered in the 18- and 20-in. chambers; combustion in the 16-in. chamber was smooth throughout its region of stabilization. The upper portion of the blowout curves could not be definitely established because of the rough burning encountered at the high velocities. Rough burning is distinctly different from oscillatory burning, the former occurring intermittently at a random frequency and the latter exhibiting sustained operation at constant frequency.

The lean limits of oscillatory burning were obtained by decreasing the fuel-air mixture ratio of an oscillatory system until smooth burning is achieved. The data obtained in this manner are remarkably consistent and reproducible. The rich limit of oscillatory combustion is not as sharply defined, however. As the mixture fuel-air ratio is increased, the oscillatory burning gradually changes to either smooth or rough burning, depending on the magnitude of the approach velocity. The region of oscillatory burning is indicated by the cross-hatched area in Fig. 4.

Further inspection of Fig. 4 indicates that the rich blowoff limits for the 18- and 20-in. chambers are coincident through the range of velocities in which oscillatory burning occurred, and no definite rich limits could be determined at velocities greater than 180 fps. In addition, it is noted that the region of oscillatory combustion extends up to the stability limits of rich burning for the 18- and 20-in. combustors. From these observations it is evident that the existence of oscillatory combustion restricts the range of stable burning and imposes an upper bound on the velocities at which rich blowoff can be determined. It is noted that Polanyi and Markstein (4) reported similar narrowing of the stability region by the imposition of high frequency (3–12.5 kc) sound on a premixed flame.

High speed motion pictures of the oscillatory phenomenon in a 20-in. chamber with an expansion ratio of 3.92:1 are shown in Fig. 5. These pictures were obtained with a 16-mm Fastex camera operating at 3000 frames per sec with the necessary luminosity provided by the introduction of magnesium oxide into the flame. The frame sequence proceeds from top to bottom and from left to right. The region photographed is that area near the edge of the expansion. These pictures clearly show the longitudinal character of the pulsations, approximately three cycles appearing in the sequence. Nicholson and Field (3) obtained similar pulsation pictures of a flame stabilized on a V-gutter which indicate that the character of the pulsations, once they are established, is independent of the mode of stabilization.

Further study revealed that the frequency of oscillatory burning is insensitive to expansion ratio while varying inversely with the length of the chamber. The measured frequencies for the 18-, 20- and 22-in. chambers with expansion ratios of 2.85:1 and 3.92:1 were correlated by the equation

$$f = a/4L\left(\frac{1}{1 - M^2}\right) \qquad [1]$$

with a maximum deviation of 5 per cent. In this equation, which was obtained from a simplified one-dimensional perturbation analysis of the chamber flow process, a and M are the speed of sound and Mach number of the hot gases in the chamber, respectively; and L is the length of the chamber. A similar analysis was performed previously by Woolstan and Runyon, the details of which can be found in (3). The correlation presented by Equation [1] further establishes the longitudinal character of the oscillations which were observed.

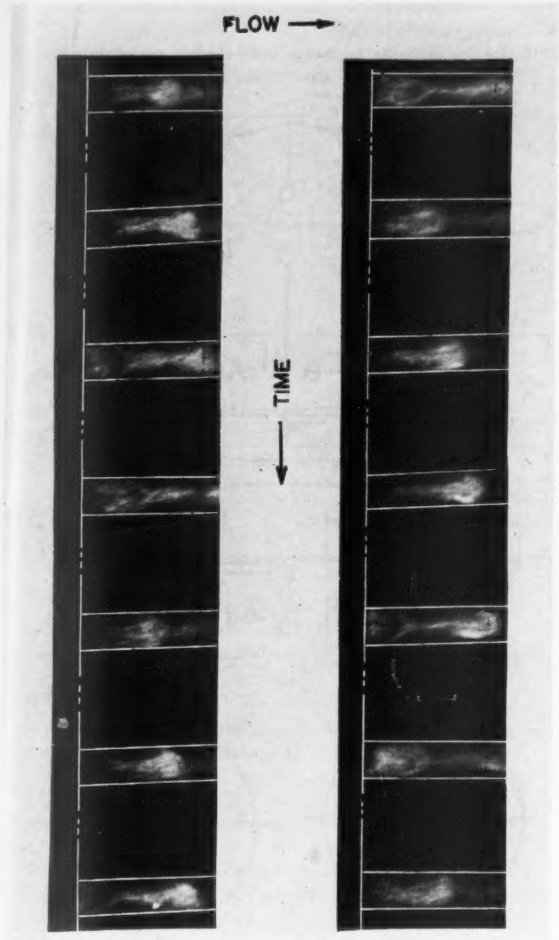

Fig. 5 High-speed motion pictures of oscillatory burning; 3000 frames per sec, L = 18 in., V = 140 fps, ϕ = 1.15

Conclusions

1 Oscillatory burning restricts the range of stable burning for rich flames and imposes an upper bound on the velocities at which rich blowoff can be determined, but it had no effect on the lean limits of stabilization.

2 The lean limit of oscillatory burning is sharply defined whereas the rich limit is vague.

3 The flame blockage is significantly greater with oscillatory combustion.

4 The oscillations are longitudinal and correspond to the resonant frequency of the chamber. After oscillatory combustion has been established, the character of the pulsations is independent of the mode of stabilization.

Acknowledgments

This note is based on the M.S. thesis of the author. The work was financed through a Phillips Petroleum Company Fellowship Grant and Faculty Research Project 103-54 of Northwestern University. The author wishes to express his gratitude to A. B. Cambel and the members of the Gas Dynamics Laboratory of Northwestern University for their advice and inspiration.

References

1 Rogers, Don E., and Marble, Frank E., "A Mechanism for High Frequency Oscillation in Ramjet Combustors and Afterburners," Heat Transfer and Fluid Mechanics Institute, VIII, June 1955.

2 Kaskan, W. E., and Noreen, A. E., "High-Frequency Oscillations of a Flame Held by a Bluff Body," *Trans. ASME*, vol. 77, 1955, p. 885.

3 Nicholson, H. M., and Fields, J. P., "Some Experimental Techniques to Investigate the Mechanism of Flame Stabilization in the Wakes of Bluff Bodies," Third Symposium on Combustion, p. 44.

4 Polanyi, M. L., and Markstein, G. H., "Phenomena in Electrically and Acoustically Disturbed Bunsen Burner Flames," SQUID Technical Memorandum CAL-3, Cornell Aeronautical Laboratory, 1947.

On Radiation From Combustion Gas

SYŌGO MATSUNAGA[1]

University of Osaka Prefecture, Sakai, Osaka, Japan

When the temperature of combustion gas in the furnace is held constant, combustion gas burning perfectly radiates weaker than combustion gas burning imperfectly by the effect of unburned carbon particles illuminating in the combustion gas.

If we burn gas imperfectly for the purpose of obtaining more radiation from combustion gas by the effect of illuminating carbon particles, then the gas temperature falls by the effect of imperfect combustion.

In this paper, the author presents the method of burning gas for obtaining more radiation than the usual combustion method, by which we can burn gas perfectly for obtaining high temperature combustion gas under the condition of combustion gas having metallic ion or other ions in gas, and these ions give the radiation effect of the illuminating carbon particles to perfect combustion gas.

The experimental method can be seen in Fig. 1; the experiments were performed by adjusting the air flow rates into the Bunsen burner for obtaining the gas flame at the condition of perfect combustion. For the two cases, i.e., the case of free combustion of gas and the case of combustion of gas

Received Sept. 30, 1957.

[1] Assistant Professor, Department of Mechanical Engineering, Engineering College.

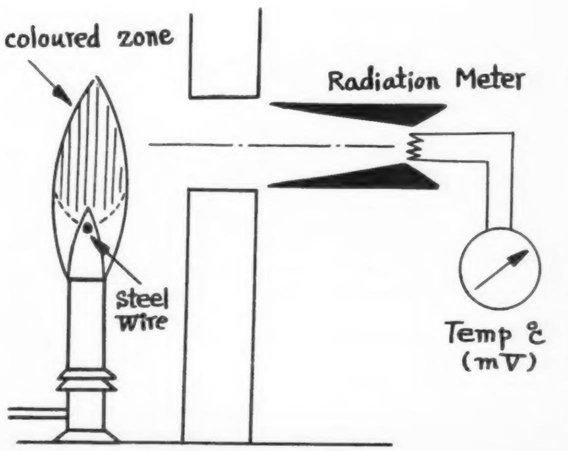

Fig. 1 Experimental methods

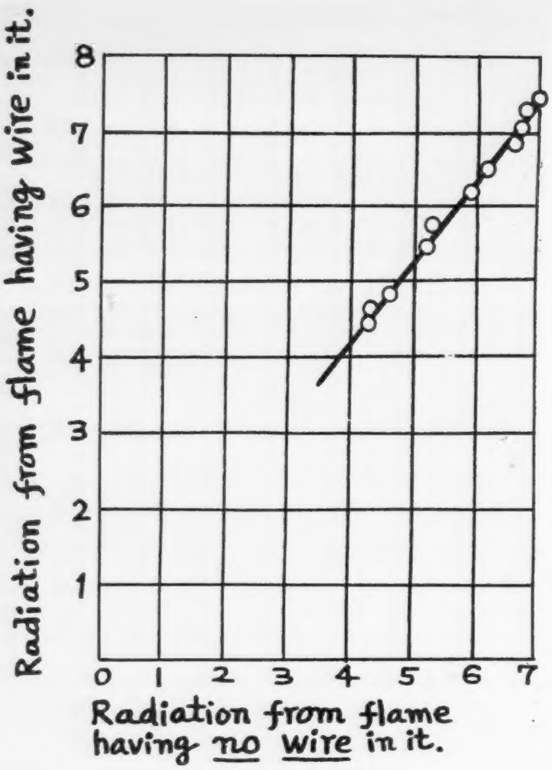

Fig. 2 Experimental result

colored by the small steel wire held horizontally in the gas flame, the author read the temperature scale of the radiation meter.

The experimental results can be seen in Fig. 2, by which we can understand the following facts:

1 The temperature drop caused by the latent heat of vaporization of metal can be neglected.

2 The radiation effect of the perfectly burned gas will be made stronger by adding the ions used for coloring the gas flame.

On the Thermal Resistance of the Water Droplet on the Metallic Surface

SYŌGO MATSUNAGA[1]

University of Osaka Prefecture, Sakai, Osaka, Japan

IN THIS note, the author presents the new electric tank method for study of heat conduction in solids. The solid mixture of paraffin wax and carbon black powder can be used in the electric tank filled with city water.

Using this method, the author presents an example. The thermal resistance of the water droplet on the metallic surface can be obtained by the following process:

The experimental method is shown in Fig. 1, where

R_A = electric resistance (i.e., thermal resistance for the metal sheet and water droplet)

R_B = electric resistance (i.e., thermal resistance of metal sheet)

λ_1 = thermal conductivity of metal sheet (given by city water in the electric tank)

λ_2 = thermal conductivity of water droplet (given by the solid mixture of paraffin wax and carbon black powder in the electric tank)

$L_A L_B$ = distance between two electric poles adjusted its position in the water tank.

Received Oct. 11, 1957.

[1] Assistant Professor, Department of Mechanical Engineering, Engineering College.

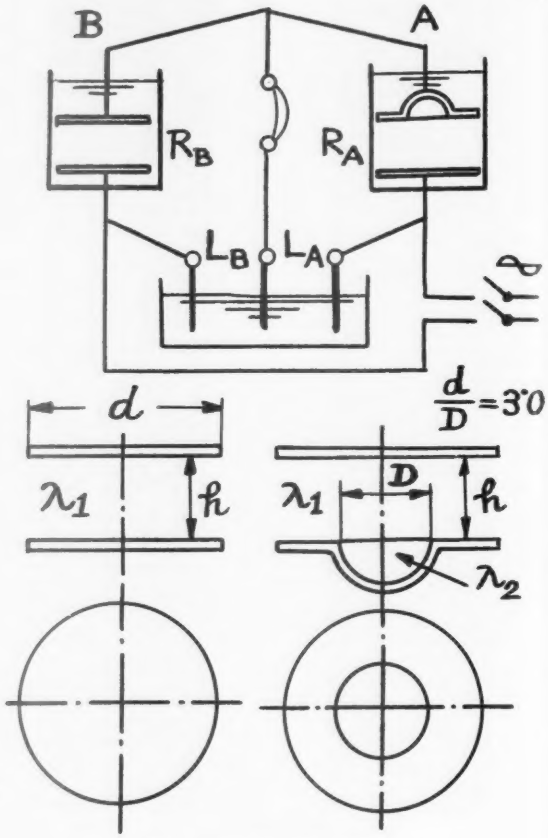

Fig. 1 Experimental method

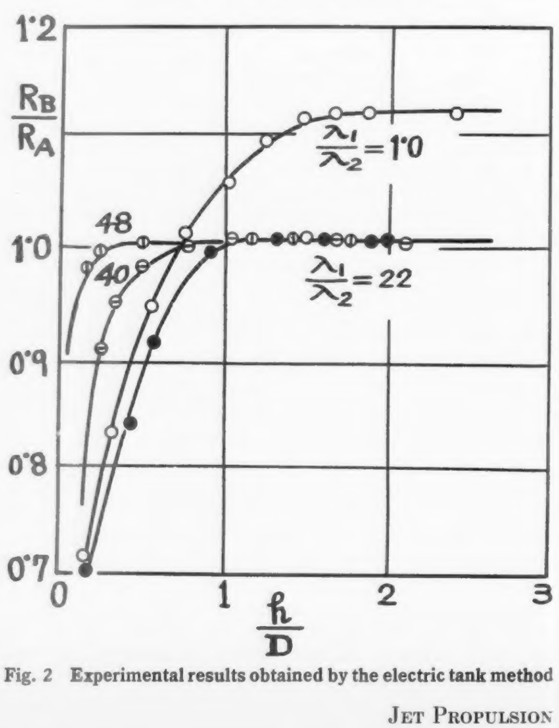

Fig. 2 Experimental results obtained by the electric tank method

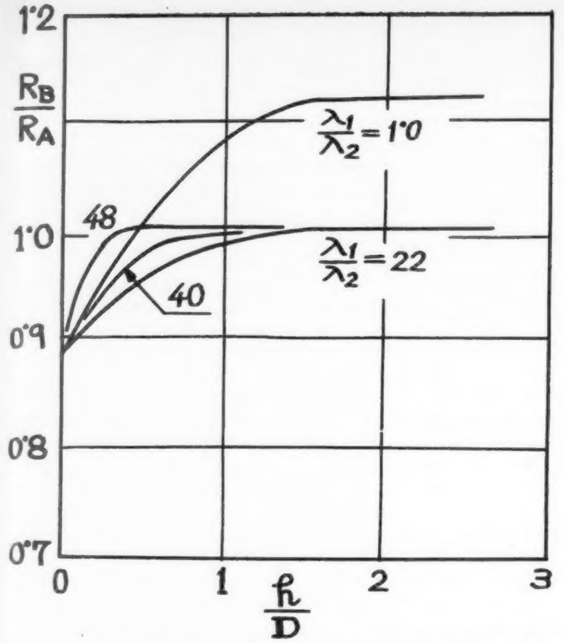

Fig. 3 **Thermal resistance of the water droplet on the metallic surface**

When we adjust L_A and L_B to the balanced state of the Wheaston Bridge, the relation of

$$\frac{R_A}{R_B} = \frac{L_A}{L_B}$$

can be obtained.

The experimental results can be seen in Fig. 2.

When h has the value of nearly zero, the ratio of R_B/R_A must be nearly equal to the inverse ratio of the contact surface area, i.e.

$$\frac{R_B}{R_A} = \frac{\pi(d^2 - D^2)}{\pi d^2} = 0.89$$

so the curves in Fig. 2 must have the value of $R_B/R_A = 0.89$ at $h/D = 0$. By this fact, the curves of the thermal resistance can be written as shown in Fig.3.

Calculated Viscosity of a Solid Propellant Rocket Exhaust Gas Mixture

W. GIN[1]

Hughes Aircraft Company, Culver City, Calif.

The absolute viscosity of the exhaust gas mixture from the rocket combustion of a composite-type solid propellant has been calculated according to rigorous kinetic theory (Reference 2). Seven species including trace concentrations were considered, and the temperature of the mixture was taken to be 2160 R. The computed value of the viscosity is 9.76 (10^{-7}) lb-sec/ft², which is shown to be approximated well by a value obtained from less rigorous theory.

Discussion

THE purpose of this note is to report the result of a calculation of the absolute viscosity associated with the laminar shearing stress of a composite-type, solid propellant exhaust gas mixture. This mixture is assumed to be under the thermodynamic conditions prevailing near the exit plane of a supersonic rocket nozzle. There is considerable interest in the heat transfer characteristics near the exit of the nozzle because of the possible location in that section of various devices like jet deflectors or parasitically ignited tracking flares. Although the flow conditions may be turbulent rather than laminar in the nozzle exit region, the value of viscosity due to molecular momentum exchange is nevertheless of practical application (1).[2]

For this computation, the temperature of the gaseous mixture is 2160 R, the assumed local static temperature of the free stream at the nozzle exit. A total of seven molecular species in the concentrations shown in Table 1 was considered. Chemical equilibrium is assumed.

Table 1 Exhaust gas composition of composite-type solid propellant

Component	Mole fraction
H_2O	0.25
HCl	0.23
CO	0.18
CO_2	0.14
N_2	0.09
SO_2	0.07
S_2	0.03

NOTE: There remains less than 1 per cent of other gases.

At first, the rigorous kinetic theory of Hirshfelder, Curtiss, Bird and Spotz (2) was applied to this calculation. The procedure entailed the determination of the force constants for each species in like as well as unlike molecular collisions and the formulation of a somewhat unwieldy eighth-order determinant. The evaluation of the determinant was performed by the staff with the IBM 650 digital computer. The resulting value for the absolute viscosity of the mixture is 9.76 (10^{-7}) lb-sec/ft².

Reference (2) indicates a correction to be applied to the viscosity calculation in the event that a strongly polar molecule like water occurs as one of the components of the mixture. Table 1 shows that H_2O turns up as one of the major components. The correction is to be made in the evaluation of the interaction force constant of water vapor with the other constituent gases. However, when the correction was made, it was found that the changes on the force constants were comparatively insignificant, so that H_2O in this calculation may be treated as a nonpolar molecule.

Although there is no published experimental information available to the writer for verification of this result, a check of some data (3) concerning the viscosity of some of the pure component gases indicates that the calculated result for the mixture is very credible. As the method of Hirshfelder and his associates is based on the Lennard-Jones model of the molecule, there may be some question as to the conformance of the components of a high temperature gaseous mixture to that model. Whalley and Schneider (4) have pointed out that the viscosity is not greatly affected by departure from the Lennard-Jones model and that extrapolation of the viscosity vs. temperature may be accomplished up to 2700 R with 5 per cent or better accuracy. It would seem that for the temperature range generally encountered in the exit section of rocket nozzles, viscosity calculations by this method should lead to satisfactory results.

However, it is realized that the comparatively weak dependence of heat transfer coefficients on the value of viscosity and other usually gross assumptions made in heat transfer analyses may not justify the careful and time-consuming calculation of viscosity by the rigorous method (assuming that

Received Oct. 14, 1957.

[1] Now Research Engineer, Jet Propulsion Laboratory, California Institute of Technology, Pasadena, Calif. Mem. ARS.

[2] Numbers in parentheses indicate References at end of paper.

the method leads to correct values). In this regard, the viscosity of the same mixture was also calculated by the method of Wilke which is based on simplified kinetic theory and does not require the evaluation of force constants (5). The procedure is thereby greatly shortened and yields, for engineering purposes, a result of adequate agreement with the value given by the more sophisticated theory of Hirshfelder et al. The viscosity for the mixture at the same temperature is 9.14 (10^{-7}) lb-sec/ft^2 according to Wilke's equation.

References

1 Bartz, D. R., "The Role of Transport Properties in the Problems of Jet Engines and Rockets," paper presented at the 1957 Gas Dynamics Symposium on "Transport Properties of Gases at High Pressures and High Temperatures," Northwestern University.

2 Hirshfelder, J. O., et al., "The Transport Properties of Gases and Gaseous Mixtures," Section D in "High Speed Aerodynamics and Jet Propulsion, vol. I. Thermodynamics and Physics of Matter," edited by Rossini, F. D., Princeton University Press, Princeton, 1955, pp. 339–418.

3 Reuel, N. C., and Friedman, J., editors, "Liquid Rocket Design Manual," North American Aviation Aerophysics Laboratory Report 259, 1947.

4 Whalley, E., and Schneider, W. G., "The Lennard-Jones 12:6 Potential and the Viscosity of Gases," *Journal of Chemical Physics*, vol. 20, 1952, pp. 657–661.

5 Wilke, C. R., "A Viscosity Equation for Gas Mixtures," *Journal of Chemical Physics*, vol. 18, 1950, pp. 517–519.

Dynamic Pressure Measurement

(*Continued from page 85*)

able for high temperature operation, but are widely used as blast gages.[6] They were difficult to calibrate statically because of the lack of extremely high input impedance amplifiers until the recent introduction of electrometer tube circuits and dielectrics which make possible the retention of charges for static calibration.

The research work done by Brosa, Nier and Mauer in Germany has led to the development at Freiburg of several successful models of water-cooled and air-cooled quartz pickups (16). The over-all designs appear to be similar to that of the Li-Liu pickup and are believed capable of operation at elevated temperatures. The Swiss Locomotive and Machine Works (in Switzerland) piezo-electric (SLM) pickup has a number of novel design features. A sealed steel tube, not unlike the strain tube, tightly compressing two quartz pieces of semicircular cross section constitutes the sensing element. Axial loading of the cylinder results in both axial and transverse stresses in the quartz to produce the piezo-electric effect. Although they are highly promising transducers, the SLM pickups nevertheless suffer from appreciable hysteresis (about 2 per cent maximum) and substantial temperature drift. At very high neutron flux a considerable amount of error is introduced.

In using the high output impedance type of sensing element, like the piezo-electric and capacitance types, the connecting cable is an important factor in the dependability of the measurement. Perls has pointed out that large errors can be caused by the migration of electric charges when a coaxial cable is subjected to vibration (17). His research led to the development of the low noise coaxial cable which, when used in a short length adjacent to the pickup, can eliminate these vibration generated noises.

The magnetic type of sensing elements, such as the Ultradyne variable reluctance pickup, has good zero stability and high signal-to-noise ratio. Many magnetic pickups, however, are sensitive to temperature effects and their responses are limited by the relatively low carrier frequency—usually less than 20 kc—and by the core loss. The inductive type of gage, which is less susceptible to temperature effects and has a relatively large output, can be made linear over a given range but still suffers from core losses at high carrier frequencies, and the relatively large moving mass prevents its use for measurements above 1000 cps. A few specially built types, among which is one German pickup, are known to be able to operate up to 3 kc.

Generally speaking, pickups which use changes in inductance and capacitance do not have wide linear range. By restricting their use to a small part of the general curve or through use of external linearizing devices, closer linear operation can be obtained.

Pressure gages using the optical interference principle originally reported by Buck and Barkas in 1948 (18), have gained increasing acceptance in recent years although they are bulky and cannot be used at elevated temperatures. The data presentation form also is quite awkward to use.

Diaphragmless Devices

The possibility of sensing pressure without resorting to diaphragm-type transducers has been investigated recently by aeronautical researchers. Some of their investigations in the low pressure measurement field have included the well-known Alphatron, x-ray and electron beam methods (19). These are primarily density measuring devices, but for simple gas systems at constant temperature their outputs can be calibrated in terms of pressure. The Alphatron uses a radioactive source which emits alpha particles at a speed 0.05 that of light. When the alpha particles collide with gas molecules, the latter are ionized by the loss of an electron. Under standard atmospheric conditions, a single particle will ionize 10^4 air molecules per cm. Thus, an electric field imposed between the electrodes generates a current proportional to the number of ionized particles produced per unit time. Over wide ranges of pressure, however, the output of the Alphatron is by no means linear.

The electron beam method depends partly upon the absorption and partly upon the scattering of an electron beam by the molecules in gases (20), and the x-ray technique makes use of the absorption of soft rays, i.e., x-rays with wave length longer than 2 Å to measure the density (21). These two methods are based upon the familiar absorption law

$$I = I_0 e^{-\mu l}$$

where μ is the absorption coefficient, and is a function of the density and the atomic number of the absorbing gas; l is the thickness of the layer of matter to be measured. Arnold, Dimeff and Kistiakowsky were among the workers who have applied the x-ray techniques to measurement of transients (22). Except in special applications, however, none of these systems has, at the present stage, attained the degree of simplicity and versatility of the diaphragm-type sensing element systems. A knowledge of the status of development in diaphragm design is, therefore, essential to dynamic pressure measurement engineering. A discussion of this topic is outside the realm of the present paper. The classic writings in the field are well known and have been reviewed in (23). Analytical information on practical design aspects of various pressure receiving elements is presented in (24).

Very High Speed Transient Pressure Measurement

Electromechanical pickups cannot, in general, by themselves fulfill the requirements of ultra high speed measurement because:

1 The ringing of pickups at their natural frequencies tends to obscure the waveform of the input pressure phenomena.

2 They do not have the requisite

[6] Newer ceramic-type piezo-electric materials such as Piezite II, lead metaniobate, and lead zirconate-lead titanate show promise as sensing elements for lower temperature operation.

Kodak reports on:

keeping your fingers dry . . . ideas that gel, or turn thixotropic . . . what the founder of the foundry didn't know

Brute force

Photographic paper which requires no processing is of itself no news.* There may be a little news in that at least two major manufacturers of moving-mirror oscillographs now offer recording instruments based on what we call *Kodak Linagraph Direct Print Paper*. If *they* want to call it something else, we love them none the less.

In giving up photographic development, one gives up for the sake of dry fingers an energy amplification factor of enormous power. Nevertheless, we agree that dry fingers are nicer than wet fingers. We bow low to the optical design ingenuity that has contrived cool and quiet little boxes in which most satisfactory traces are put down through brute force of u-v radiation. One company claims frequencies to 2,000; the other, to "above 3,000," with trace velocities "above 30,000 inches per second."

At low recording and writing speeds, focused energy from a high-intensity Hg-vapor ultraviolet point source is sufficient for a legible record. Where it isn't, use is made of a post-exposure to some 60 foot-candles from a fluorescent lamp. For all practical purposes the post-exposure raises the speed several hundred times. The trace comes out blue on a buff background. As with most miracles, the miracle of *Kodak Linagraph Direct Print Paper* becomes a little less miraculous upon quantitative study. The total energy delivered to the paper in the writing and the post-exposure is about the same as the radiant energy required by a conventional photographic enlarging paper. It's just that the energy requirement can be supplied in two separate doses.

If interested in this type of oscillography, watch for pertinent ads in the technical press and alert your purchasing agent to send in the next man who comes around with one of these instruments. If you have other ideas for this type of paper, Eastman Kodak Company, Graphic Reproduction Division, Rochester 4, N. Y., will try to be helpful by arranging with a local dealer to sell you some of it for experimentation.

Mono-and-water

We have run into a few matters in the field of colloid chemistry that can stand being presented straight. They concern monoglycerides, a kind of fat widely used in baking. Monoglycerides can seize water and imprison it.

• When a monoglyceride at a temperature above its melting point—which for some may not much exceed that of water—is poured into water at the same temperature, a firm gel is instantly formed. The gel contains 15 to 25% of water. Child of what appears to be hydrogen bonding of water to oil, it is dispersible in the former not at all and soluble in the latter only with difficulty. Turbid when first formed, this gel turns quite transparent shortly thereafter. As long as kept warmer than the melting point of

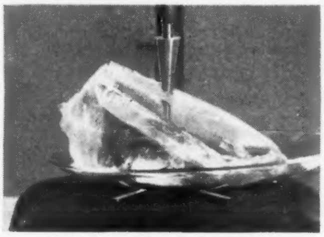

the monoglyceride, the gel is indefinitely stable. Its life is limited by evaporation loss of the water if left open to the atmosphere.

• When the pouring is done the other way—water into the liquid monoglyceride—viscosity of the equilibrized system rises continuously until a non-pourable transparent "solid" results. By severe manipulation, it is possible to make thus a gel as firm as putty, containing up to 45% water without leaking. Its conductivity is that of water, which is very much higher than that of water-in-oil emulsions.

• Clear homogeneous liquids can be made from water, plain fat, and monoglyceride. The water can carry water-soluble substances while the fat carries oil-soluble substances.

• With liquid monoglyceride, water, and soap, one can make a translucent thixotropic liquid that is "springy," like egg white. When cooled below a certain point, it changes to a crystalline character in which it is like translucent pudding, but still thixotropic. A word like "thixotropy," casually dropped in non-rheological company, can help a person.

Notice how nothing is said about applications? That's because we want you, gentle reader, to have a head start over your competitors. For a full report on mono-and-water, as we see it to date, write Distillation Products Industries, Rochester 3, N. Y. (Division of Eastman Kodak Company).

The radiographer enlightened

The foundry had been dedicated by the proprietor's grandfather to the peaceful production of parlor stoves. One day the treasurer came to the boss and told him the x-ray machine had paid for itself. How is that? asked the boss. Why, in metal saved. Radiography of the pilot castings had pointed out the real danger spots in mold design and had showed where the need for 400% safety factors on cross-section was imaginary.

So the radiographer acquired an assistant to do the work, went off to the annual convention, and came home sounding like this:

"By virtue partly of photoelectron emission and partly of secondary x-rays generated as a fluorescence process, a .005″ sheet of lead foil can serve to intensify an x-ray image on a film in intimate contact with the foil. At the same time, such a lead screen preferentially attenuates the less-penetrating longer wavelengths of the primary radiation. Obviously, both the intensification and filtration effects are strongly kilovoltage-dependent. It has been shown recently that by employing one or both of these effects with two (or even three) films of different (or even the same) speed in the exposure holder, a wider range of specimen thickness can be adequately radiographed in a single exposure, with the achievement thereby of a substantial saving of time and, consequently, of cost."

He heard that from a Kodak man named Ralph E. Turner. If you want a clearer idea of what Mr. Turner said, request a copy of the paper from Eastman Kodak Company, X-ray Division, Rochester 4, N. Y.

---

*For better than 60 years we have made studio proof paper. On it many portrait photographers submit those brownish-purple proofs from which the customers select the poses they like. The proofs are to be returned. People who instead stick them up on their boudoir mirrors find they don't last very long in the light of day. That's the idea with studio proof paper—no developing *and no fixing*.

This is another advertisement where Eastman Kodak Company probes at random for mutual interests and occasionally a little revenue from those whose work has something to do with science

Kodak
TRADE MARK

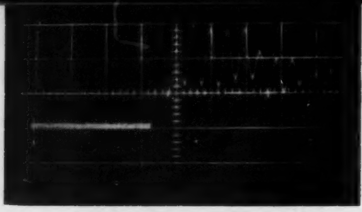

Fig. 3 (a) Response of transducer to shock wave using GN_2 (sweep speed: 10 μ sec/cm)

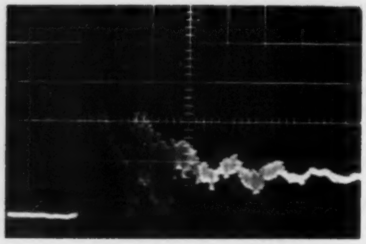

Fig. 3 (b) Response of a Rutishauser transducer to a shock tube employing pneumatic feedback (sweep speed: 200μ sec/cm)

Fig. 3 (c) Response of Fig. 3 (a) equalized by DADEE (sweep speed: 10 μ sec/cm)

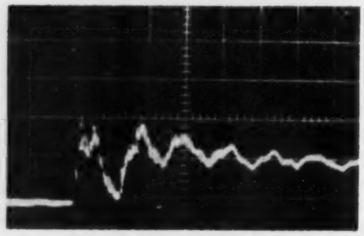

Fig. 3 (d) Response of Fig. 3 (b) equalized by DADEE (sweep speed: 200μ sec/cm)

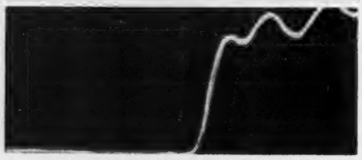

Fig. 4 Response to a step pressure using DADEE (sweep speed: 2 μ sec/cm)

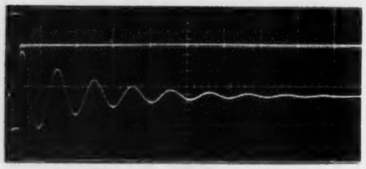

Fig. 5 Driving function, simulated transducer output, and equalized DADEE output (sweep speed: 10 μ sec/cm)

transient response and, therefore, cannot indicate the true pressure magnitude without overshoot or attenuation and phase shift.

These inadequacies are immediately apparent when one examines Figs. 3(a) and 3(b) which show the response of two pickups respectively to a step function and to a complex pressure function. The true waveforms of the same driving functions are shown in Fig. 3(c) and 3(d). The driving functions shown in Fig. 3(c) and 3(d) were measured and recorded instantaneously by the DADEE system (Dynamic Analog Differential Equation Equalizer) developed by the authors at Rocketdyne (25). This system and the Dyna-electronic Transientgraph are two new methods by which fast pressure phenomena can be measured without any postmeasurement correction for dynamic errors except an extremely small amount of time delay. With the present model of the DADEE, pressure transients with rise times as short as 0.5 microsec have been measured.[6] New models promise even faster response. Fig. 4 shows a 1-microsec pressure front taken with a Rutishauser pickup whose natural frequency is 80 kc.

Briefly, the DADEE system automatically compensates for the transducer dynamic characteristics during any transient or steady-state measurement.

An exhaustive series of tests has been carried out at Rocketdyne in order to prove the validity of this system. To illustrate the results, Fig. 5 shows a driving function in the form of an electronic pulse whose rise time is estimated to be of the order of millimicroseconds. The ordinary response of a simulated pickup is shown next to its driving function. Note that this response function has very little resemblance to the original function. On the contrary, the output of the DADEE system as shown in the bottom of the picture is a close reproduction of the original function.

With DADEE designed on the basis of a linear differential equation, the question naturally arises as to the applicability of this technique to nonlinear pickups. Nonlinear pickups are known by such response characteristics as jump phenomena and ultra- and subharmonic resonances. In some well designed pickups these nonlinear characteristics are minimized through design skill but, when this is insufficient, we must resort to the technical solution of the nonlinear problem. An effective technical tool in approaching the nonlinear pickup problem is the Transientgraph system which was developed by Liu and is based upon the phase-plane method (Fig. 6).

[6] A detailed description of the DADEE system will be published separately. The systems have been submitted for patent application by Rocketdyne under the authors' names.

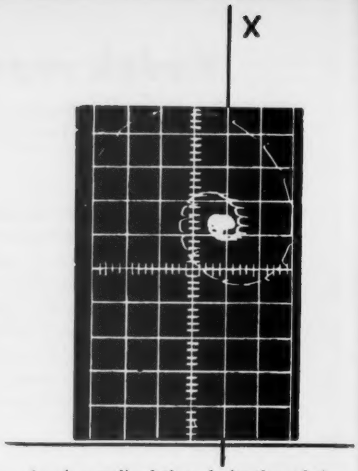

Δx (normalized time derivation of x)

Fig. 6 Dyna-electronic Transientgraph (nat. frequency = 60,000 cps)

As a tool for solving nonlinear systems, this approach has been studied by Andronow and Chaikin (26) and others. When modified to apply the Ritz-Klotter method, it is possible to extend it to the solution of steady-state nonlinear vibration problems (27). This presentation provides, in a single picture, all the essential information in the time and space domain from which natural frequency, damping ratio, etc., can be determined. With this information available, one can use simple graphical methods to reconstruct accurately the true waveform from the phase-plane diagram[7] The present models of the Transientgraph are practical systems which can be used to deal with transducers having nonlinear characteristics and even those with more than one degree of freedom.

References

1 Ross, C. C., and Datner, P. P., "Combustion Instability in Liquid Propellant Rocket Motor—A Survey," AGARD, NATO, Dec. 1953.

2 Glass, I. I., and Patterson, G. N., "A Theoretical and Experimental Study of Shock-tube Flows," *Journal of the Aeronautical Sciences*, vol. 22, Feb. 1955, particularly pp. 99–100.

Davis, R. M., et al., "Pressure Measurements in Detonating Gases," *Proceedings of the Royal Society*, A, vol. 204, 1950, pp. 17–19.

3 Iberall, A. S., "Attenuation of Oscillatory Pressure in Instrument Lines," *N.B.S. Journal of Research*, vol. 4, 1952, p. 85.

4 Hornig, D. F., "Shock Front Measurement by Light Reflectivity," High Speed Aerodynamics and Jet Propulsion, vol. IX, Princeton, 1950.

5 Draper, C. S., and Li, Y. T., "A New High-Performance Engine Indicator

[7] The detailed methods of reconstructing the original waveform will not be elaborated in this article but will be presented in a separate paper in the future.

of the Strain-gage Type," *Journal of the Aeronautical Sciences*, vol. 16, Oct. 1949, p. 593.

Li, Y. T., "Dynamic Pressure Measuring System for Jet Research," JET PROPULSION, vol. 23, 1953.

Matthews, G. B., "The Development of Li-Liu Pickup," Princeton Aeronautical Engineering Department Report 216F, Dec. 1953.

6 For an excellent bibliographical work on pressure measurement, consult: Brombacher, W. G., and Lashof, T. W., "Bibliography and Index on Dynamic Pressure Measurement," N.B.S. Circular C558, (G.P.O., Washington, D.C., 1955).

Li, Y. T., "Pressure Measuring Systems," Chap. 33 of "Instrumentation Engineering," vol. III, McGraw-Hill, 1955.

Hermann, P., and Stiefelmeyer, G., "Beitrag zur elektrischen Messung von Druckvorgängen," *Elektronik*, vol. 5, 1956, p. 94.

Schwartz, Jean (French), "Electronic Gages," *Microtecnic* 11, 5.

Olson, H. F., "Mechano-Electronic Transducers," *Journal of the Acoustical Society of America*, vol. 19, March 1947, p. 307.

7 "Dehnungmesstreifen," *Archiv. fur Tech. Messen.*, 5–238.

"What are Effects of Radiation on Electronic Components," *Nucleonics*, July 1956, p. 33.

8 Instruction books and bulletins of Statham Laboratories.

Sailer, O. W., "Miniaturization of Transducers for Mobile Application," Consolidated Engineering Corp., Pasadena, Calif.

9 Private communication from Mr. Statham of Statham Laboratories.

10 Yates, J. G., "Pulse Excitation of Impedance Bridges," *Nature*, vol. 163, no. 4134, Jan. 1949.

Yates, J. G., Lucus, D. H., Johnston, D. L., "Pulse Excitation of Resistance Stress Gages for Dynamic Multi-channel Observation," *Proceedings, Experimental Stress Analysis*, vol. XI, no. 1, 1952, p. 35.

Sander, N. D., and Brodie, G. H., "Application of Pulse Techniques to Strain Gage," NACA RM E-54 1308.

11 Alman, J., "Pressure Recorders for Rocket Motor Studies," *Electronics*, May 1953, p. 146. (Note: the Rutishauser-Omega uses phase-modulation techniques both tube and transistor version.)

Hett, J. H., and King, R. W., Jr., "A Frequency Modulation Pressure Recording System," *Review of Scientific Instruments*, vol. 21, Feb. 1950, pp. 150–153.

Grinstead, C. E., Fawley, R. N., et al., "An Improved Indicator for Measuring Static and Dynamic Pressures," *SAE Trans.*, vol. 52, 1944.

12 Private communication from F. L. Bentzen of SPERT (Phillips Petroleum Co.).

Rogers, F. T., Jr., "Effect of Pile Irradiation on the Dielectric Constant of Ceramic $BaTiO_3$," *Journal of Applied Physics*, vol. 27, Sept. 1956, p. 1066.

13 Ir. Diehl, E. J., and Ir. Visser, H., "Measurement of Rapidly Fluctuating Pressures," *International Shipbuilding Progress*, vol. 1, no. 3, 1954.

14 Linlor, W. I., Kerns, Q. A., Mark, J. W., "Bubble Chamber Pressure Gage," UCRL-3173 (Rev.) for AEC, Jan. 1957.

15 Bleakney and Arons, op. cit.; Arons, A. B., and Cole, R. H., "Design and Use of Piezoelectric Gages for Measurement of Large Pressure," *Review of Scientific Instruments*, vol. 21, 1950, p. 31.

16 Klein, P. E., "Piezoelecktrische Quarz-Geber fuer elektronische Druckmessungen," *Achiv. f. Tech. Messen*, V 132–20, Nov. 1956, p. 247.

Hutchinson, L. J., "An Apparatus for Recording Explosion in Compressed Gaseous Mixtures from Piezo-electric Transducers," Br. Armament Research Division, Ministry of Supply, Report 23/54, 1954.

17 Perls, T. A., "Electrical Noises from Instrument Cables Subjected to Shock and Vibration," *Journal of Applied Physics*, vol. 23, p. 674.

18 Buck, W., and Barkas, W. H., "Dynamic Pressure Measurement by Optical Interference," *Review of Scientific Instruments*, vol. 18, 1947, p. 188.

19 Spenser, N. W., Schulte, H. F., and Sicinski, H. S., "Rocket Instrumentation for Reliable Upper Atmosphere Temperature Determination," *Proc. I.R.E.*, July 1954.

Downing, J. R. and Mellon, G., "A Sensitive Vacuum Gage with Linear Response," *Review of Scientific Instruments*, vol. 17, June 1946, pp. 218–223.

20 Schopper, E., and Schumacher, B., "Messung von Gasdichten mit Korpuskularstrahsonden," *Z. Naturforsch* 6a, 700–705, 1951.

21 Winkler, E. M., "Spectral Absorption Method," in "Physical Measurements in Gas Dynamics and Combustion," edited by R. W. Ladenburg, B. Lewis, R. N. Pease, and H. S. Taylor, Princeton, 1954, p. 89.

22 Dimeff, J., Hallett, R. K., and Hansen, C. F., "X-ray Instrumentation for Density Measurement in a Supersonic Flow Field," NACA TN 2845, 1952.

Podgornyi, M., "X-ray Emission at the Start of a Gas Discharge," *Soviet Physics*, vol. 7 (no. 3, translated by American Institute of Physics, May-June 1956).

23 Liu, F. F., and Berwin, T. W., "Recent Advances in Dynamic Pressure Measurement Technique," ARS Preprint 435–57, 1957.

24 Li, Y. T., "Pressure Measuring Systems," Chap. 33 of C. S. Draper, W. McKay and S. Lees, "Instrumentation Engineering," McGraw-Hill, 1955, pp. 407–411.

25 Liu, F. F., and Berwin, T. W., "A New Instrument for Extending Transducer Transient Reponse," Rocketdyne Report R-408 (to be published).

26 Andronow, A. A., and Chaikin, C. E., "Theory of Oscillations," Princeton, 1949.

27 Klotter, K., "Steady-state Vibration in Systems Having Arbitrary Restoring and Arbitrary Damping Forces," *Proceedings of the Symposium on Nonlinear Circuit Analysis*, Polytechnic Institute of Brooklyn, April 23–24, 1953.

Klotter, K., "Non-linear Vibration Problems treated by the Averaging Method of W. Ritz," Proceedings of the First National Congress of Applied Mechanics, 1951, p. 125.

Book Reviews

Ali Bulent Cambel, Northwestern University, *Associate Editor*

Astrophysical Quantities, by C. W. Allen, John de Graeff, Inc., New York, 1955, 263 pp.

Reviewed by S. F. Singer
University of Maryland

This is probably the one indispensable handbook for an astrophysicist or anyone interested in the earth, solar system and stars. The unusual feature about the book is that it has been prepared by a single individual who is himself an outstanding astrophysicist and this leads to an important element of coherence which is so often lacking in handbooks. The volume is unusually complete in giving data connected with spectroscopy and atomic physics. Such matters as ionization potentials, electron affinities and atomic cross sections for collisions are well discussed, as are spectroscopic quantities, such as oscillator strengths, line broadening and strength of multiplets. One whole chapter deals with radiation phenomena, others with the earth, the sun, planets and satellites, interplanetary matter, normal stars, stars with special characteristics, star populations, clusters and galaxies, and interstellar space. There are of course very useful tables of general constants and units, and special tables which simplify astronomical calculations, e.g., tables for conversion from equatorial to galactic coordinates. An especially valuable feature of the book are the many good references. Every piece of information given is backed up by a reference to an original paper.

Nuclear Chemical Engineering, by Manson Benedict and Thomas H. Pigford, McGraw-Hill, New York, 1957, vii + 594 pp. $9.50.

Reviewed by Donald H. Loughridge
General Motors Corp.

The need for a comprehensive text on nuclear chemical processing has been realized by those working in nuclear engineering for some time. The present volume most adequately fulfills such a requirement. Both authors have had extensive experience in the fields covered by the present work, and in particular the senior author was one of the leaders during the war in the development of the gaseous diffusion method of uranium isotope separation.

The text is divided into twelve chapters, the first two of which provide a brief survey of nuclear properties and those important chemical elements entering into nuclear power applications. A clear presentation of the theory of radioactive decay chains and the neutron reactions entering into the fission process is presented. Next, the various fuel cycles appearing in thermal nuclear reactors and their quantitative considerations are fully developed. Illustrative problems are provided at the end of each chapter, thus greatly increasing the usefulness of the book as an advanced textbook for senior or graduate use.

Production processes utilized in preparing uranium feed material and the properties of those important elements, zirconium, thorium and beryllium, are presented with the necessary thermodynamic data to make such sections useful as reference material.

Theory and practice of solvent extraction of metals is here presented in the fullest detail (outside of AEC reports), and the properties of radiated fuel naturally lead the chemical engineer studying the text into the basic problem of the separation of reactor products. As might be expected in a text from such authorities, the subject of isotope separations of both light and heavy elements, the various theories underlying such processes, and the practical results obtained by the various methods to date, along with the economics of the various processes, occupy about the last third of the book.

The Appendix contains a section on fundamental physical constants, tables of the separation potential, tables of mass and energy equivalents, and a long table giving the known properties of the nuclides.

It is to be hoped that soon each chemical engineering department in leading universities will be adequately staffed to present the material covered by this book, and without doubt instructors in the field will feel a great debt of gratitude to the authors for their obviously tremendous task of preparing a text and reference book of such high standard. The printing is large and clear, the drawings adequate in size, and the mathematical typography well arranged.

New Horizons in Astronomy (vol. 1, no. 1, Smithsonian Contributions to Astrophysics), edited by Fred L. Whipple, Smithsonian Institution, Washington, D. C., 1956, 181 pp. $1.50.

Reviewed by S. F. Singer
University of Maryland

This is a first issue of Smithsonian Contributions to Astrophysics, which is to consist of short monographs on astronomical topics. This first issue contains a large number of short contributions which give an impression of where astronomy stands in various fields. The main headings are: Techniques and Instrumentation, which includes optical and radio methods for studying astronomical objects. The next heading is Related Sciences, which includes a short discussion of rocketry and fields of physics which are of importance to astrophysics. The third main section is the Solar System and includes the earth and smaller planets and meteors. The final section deals with Stars and the Galaxy. As expressed by the editor, Fred L. Whipple, who is the Director of the Smithsonian Astrophysical Laboratory, one of the main purposes of the volume is to encourage established astronomers to pause for a moment and reflect on the most advantageous planning in their own field of research, and supply them with a broader insight into the activities in other fields of astronomy, possibly related to their own. The first volume is perhaps less useful to a non-astronomer, since in some cases the discussion is very cursory and without references, in other cases too specialized. It is, however, a book which is easily read and should therefore be studied by anyone who has an interest in astrophysics.

Subsequent issues are being written by individual authors who will cover many important astrophysical topics of current interest.

Experimental Design: Theory and Application by Walter Federer, Macmillan, New York, 1955, xix + 544 pp. with 47 planographed problems bound with the book. $11.

Reviewed by Fred M. Westfield
Northwestern University

This is a text in statistics which will be used as a reference book in many laboratories. It deals with schemes for planning experimental investigations so as to permit efficient application of the tools of statistical inference.

While the subject matter of this book has become especially important for those many areas of modern research where costs of observations are high and the extent of laboratory control decidedly limited, it is to be regretted that most of the specific examples and problems are taken from biological and agricultural experimentation. But for this the author can hardly be blamed. Historically, this is largely where the techniques of experimental design were studied and developed, and the title page tells us that the author is professor of biological statistics in the Department of Plant Breeding at Cornell University.

The book is readily accessible to the reader familiar with basic statistical techniques as taught in a good first-course in statistics at the college level. Knowledge of the calculus or matrix algebra is not required. The bibliography is excellent.

Light Scattering by Small Particles, edited by H. C. van de Hulst, Wiley, New York, 1957, 470 pp. $12.

Reviewed by S. F. Singer
University of Maryland

This book has already become a classic in its field and should be in the library of anyone who deals with scattering problems. It is particularly concerned with the scattering of electromagnetic waves, light and radiowaves, and is by far the most

comprehensive treatise on this subject. Fortunately it has been written by a single individual who is an expert in all of the applications as well as the theory, and who has made many important contributions himself, particularly in astronomy. Van de Hulst first covers basic scattering theory, applicable to any problem; most of the book, however, is devoted to scattering by special types of particles. There are simplifications which can be introduced, either when the particles are small compared to the wave length or when the particles are large compared to the wave length. The rigorous theory can be applied for spheres of arbitrary size and has been developed by Mie. There one distinguishes between nonabsorbing spheres which introduce an important simplification, and spheres with refractive index near 1 which can be handled in a special way. In the case of very large spheres, other approaches can be applied. The case of absorbing spheres falls again in a different category. Van de Hulst discusses in detail the optics of the rain drop, a classical problem. Then there is also a discussion of scattering by circular cylinders and particles of other forms. The applications of scattering and extinction experiments are many. They are applied to chemistry to determine the size of small particles and macromolecules. Scattering experiments are of importance in aerosol physics. In meteorology scattering is of importance in connection with atmospheric haze and dust. Scattering phenomena occur in clouds and fog, and the subject is of great importance for radar meteorology.

It is in astronomy, however, where scattering phenomena give us the greatest information about inaccessible objects. The author takes up applications to planetary atmospheres and to his particular specialty, the determination of the size of interplanetary dust particles from the zodiacal light, which is really scattered sunlight.

For the practical user the book is especially valuable because it tells him just where and how to apply scattering for his measurements; the book summarizes numerical results and graphical data which are spread throughout the literature and are now made accessible for the first time in usable form.

Book Notices

Engineering Enrollment in the United States, edited by Norman N. Barish, New York University Press, 1957. This volume presents statistics of enrollment in engineering education. It discusses and interprets the data. Future requirements for engineering education are suggested.

Energy, by Sir Oliver Lodge, John F. Rider Publisher, Inc., 1957. This is a new version of Sir Oliver Lodge's publication first written in 1929.

Principles of Engineering Heat Transfer, by Warren H. Giedt, D. Van Nostrand Company, Inc., 1957. This volume is excellently suited as a textbook for the first course in engineering heat transfer. It covers conduction, convection and radiation.

New Patents

George F. McLaughlin, *Contributor*

Jet action rotors for use in a jet propulsion system (2,812,898). Ernest H. Buell, Albany, N. Y.

Turbo compressor system having a first hollow outer shaft and containing an inner shaft. An outer compressor rotor is formed in two sections, one integral with the hollow shaft. A second hollow outer shaft is integral with the other of the outer compressor rotor sections. This shaft receives an end of the inner shaft, forming a combined unit for rotation in the direction opposite to the outer shafts and rotors.

Intake sprinkler for gas turbine engines (2,812,899). R. G. Meschino, Toronto, Canada, assignor to A. V. Roe Canada, Ltd.

A rotatable spinner fairing into the contour of the wall of the central fairing adjacent the intake. A passage for liquid extends through the spinner shaft and head opening into the intake through a hole in the surface of the head.

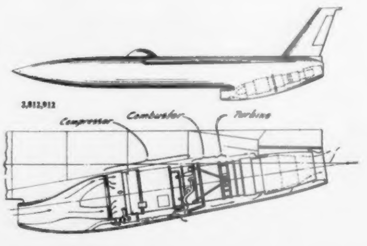

Inclined engine installation for jet aircraft (2,812,912). Wm. P. Stevens and Arthur Nitikman, Inglewood, Calif., assignors to Northrop Aircraft, Inc.

Engine assembly extending forwardly and downwardly with the longitudinal axis at an acute angle to the fuselage axis. The opening of the air intake duct is adjacent and below the lower surface of the fuselage.

Fuel injection system for ramjet aircraft (2,812,978). Louis S. Billman, Lancaster, Calif., assignor to the U. S. Navy.

Flush skin fastening of fuel injection nozzles. A cylindrical sleeve is receivable into the inner body so that its retaining collar is even in surface with the diffuser inner body surface.

Jet deflecting device (2,812,980). M. Kadosch, F. G. Paris, J. Bertin and R. H. Marchal, Paris, France, assignors to SNECMA Co.

Laterally extending guide vanes positioned downstream of the nozzle outside the normal flow path of the jet. Vanes define successive passages having inlet ends spaced along the flow path, and outlet ends opening into the atmosphere at a substantial angle with the nozzle axis.

Sight mount for a rocket launcher (2,814,-**118**). P. I. Evans and H. Harvey, Redondo Beach, Calif., assignors to the U. S. Army.

Range plate fixed on a bracket coaxially of the elevation axis. The plate is operable to hold a sight mount body in a selected elevation adjustment about the axis of a post journaled in a normally horizontal pivot bearing.

Return burning motor (2,814,179). L. B. Edelman and C. F. Miller, Sacramento, Calif., assignors to the U. S. Navy.

Rocket motor comprising a front plate from which a first cylindrical wall extends forwardly from the rear of the rocket, terminating to the rear of the front plate, forming an annular chamber and a cylindrical chamber inwardly. A single propellant charge fills the chambers, burning from the front of the annular chamber rearwardly, and from the rear of the cylindrical chamber forwardly.

Flow responsive dump valve for gas turbine fuel systems (2,814,180). J. P. Hession, Indianapolis, Ind., assignor to General Motors Corp.

Bypass having an inlet and an outlet with a fluid conduit on opposite sides of a pressure drop creating means. A control connected to a servo actuator is provided for initiating and discontinuing fluid flow.

Aircraft propulsion apparatus (2,814,349). D. W. Berry, Kansas City, Kans., assignor to Westinghouse Electric Corp.

Jet propelled helicopter rotor blades with ducts extending from the hub to exhaust nozzles at blade tips. A gas turbine is disposed in each duct. A driving means, interposed between the compressor and the turbine power take-off shaft, delivers compressed air to the turbines.

Aircraft duct screen arrangement (2,814,-454). F. W. Atkins and H. W. Elkin, Pasadena, Calif., assignors to North American Aviation.

Foldable screen covering the powerplant air intake duct and carried by the retractable landing gear. The screen moves from a stowed position within a well, to an operative position in which it screens air entering the intake duct.

Flap type variable area thrust nozzle (2,813,395). Robert E. Meyer, Glastonbury, Conn., assignor to United Aircraft Corp.

Jet engine thrust nozzle surrounded by an elongated ring with flaps pivoted at the discharge end. Openings in the forward end of the ring effect an injector action at the flaps to draw cooling air through the nozzle.

Tail cone and resilient mounting therefor (2,813,396). Ralph Kress, La Mesa, Calif., assignor to Solar Aircraft Co.

Packing of braided metallic gaskets to dampen vibrations tending to pass from the inner tail cone to the outer shell during operation of a jet engine.

Thermal expansion means for combustion chambers (2,813,397). Earl R. Fisher, Charles D. Robin and Richard C. Hurd, Manchester, Conn., assignors to United Aircraft Corp.

Fuel manifold with an air swirler unit comprising an inner sleeve telescoped in sliding fit into the fuel nozzle exterior. An outer sleeve is spaced externally from the inner sleeve, with vanes projecting between. Outer and inner cups at the forward end of the combustion chamber are free to expand without stress to the parts.

EDITORS NOTE: Patents listed above were selected from the Official Gazette of the U.S. Patent Office. Printed copies of Patents may be obtoined from the Commissioner of Patents, Washington 25, D. C., at a cost of 25 cents each; design patents, 10 cents.

TALOS

a step beyond push-button warfare!

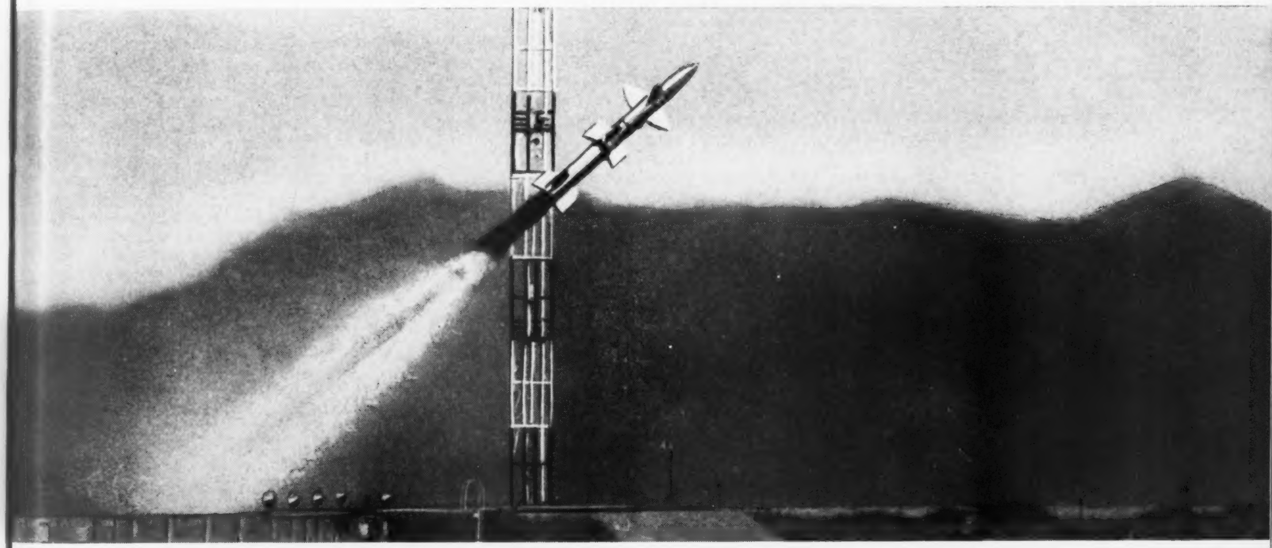

This Talos launching from the RCA Defense System on Dec. 13, 1957, resulted in direct hit on distant drone plane.

The RCA Talos Defense System is the first *completely automatic* land-based system for launching and guiding missiles, and utilizes the Talos Missile developed by the Applied Physics Laboratory and produced by Bendix. The Defense Unit receives target signals from remote outposts, analyzes them with regard to number of attackers, location, course and speed. Next, computers determine the logical points of interception, order the missiles loaded on launchers, guide them at supersonic speed to the vicinity of the target, after which the missiles "lock" on the target and close in for its destruction. All without even the touch of a button! The RCA Talos Defense System, with its electronic equipment and guidance systems, was designed, developed and built by RCA as prime contractor, aided by many subcontractors. It was turned over to the U. S. Army on October 15, 1957, and is a missile milestone, exemplifying the continuing determination of American enterprise to secure peace with honor and justice.

RCA Tmk(s) ®

RADIO CORPORATION of AMERICA

DEFENSE ELECTRONIC PRODUCTS

CAMDEN, N. J.

Wind tunnel pressure pick-ups (2,813,421). Gordon H. Cheney, John H. Russell and Phillip C. Whitener, Seattle, Wash., assignors to Boeing Airplane Co.

Wall with apertures aligned at intervals lengthwise of the airflow. A carriage guided along the line of apertures has a part which registers with successive single apertures during its advancement. A stylus, electrically operated from the carriage, records pressure as the part comes in registry with each aperture.

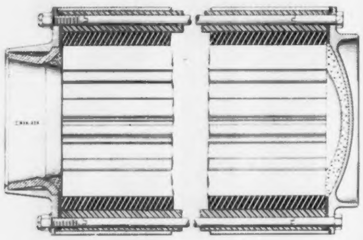

Shaped propellant charges for solid fuel rocket type motors (2,816,418). A. C. Loedding, Princeton, N. J., assignor to Unexcelled Chemical Corp.

An annularly disposed charge having an axial opening of hill and valley shape for regulating the burning characteristics of the charge radially outward. The charge consists of four quadrants with triangular stringers between.

Hydronamic bullet catcher (2,813,422). Karl E. Schuessler, Philadelphia, Pa., assignor to the U. S. Navy.

Trap for high speed projectiles consisting of a tube with an inlet for projectiles and water. A solid conical surface of water adjacent to the inlet faces and impedes projectiles entering the tube.

Ball and socket joint with internal bearing means (2,813,731). W. D. Tracy, A. L. Mager and C. A. Dasney, Arcadia, Calif., assignors to Southwest Products Co.

Duct assembly with a gasket ring recessed in an outer tubular member having an annular concave bearing surface. The gasket abuts a convex surface on an inner tubular member. Members are held together at a hub supported on spiders, permitting angular movement of the inner ring.

Leak recovering device for pulse jet units (2,814,930). H. L. P. Meulien, M. J. Baraut and J. Le Foll, Pre Saint-Gervais, France, assignors to SNECMA Co.

Jet propulsion plant in which combustion gases flow both rearwardly through the exhaust and forwardly through the intake portion, to issue from both ends of the pulsejet units. Tubular members extending forward are spaced to allow free passage of ambient air into the intake.

Gas-turbine power plant installations with means for disposal of drainage fuel (2,814,931). C. L. Johnson, Allestree, England, assignor to Rolls-Royce, Ltd.

Fuel drain arrangement including a venturi passage having an inlet connected to a source of air pressure. Fuel in a collector tank is entrained in the air flowing through the venturi passage and delivered into the exhaust gas stream, carrying the fuel clear of the installation.

Fuel system for gas-turbine engine reheat combustion stage (2,814,928). D. O. Davies and A. Jubb, Bradford, England, assignors to Rolls-Royce, Ltd.

Device located between the compressor delivery and the turbine inlet, and between the turbine and the propelling nozzle. The device is sensitive to a preselected value of the ratios of pressures at the various points, and operates the throttle to maintain a preselected value of the ratio.

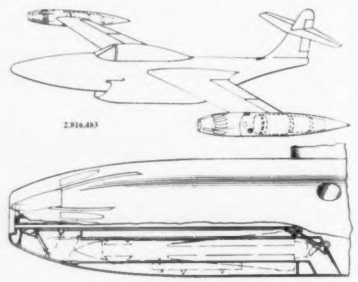

Exhaust actuated missile exit door (2,816,483). R. T. Johnson, Pacific Palisades, Calif., assignor to Northrop Aircraft, Inc.

Conduit in an airplane wingtip pod rearwardly of a rocket launching tube providing a passageway for exhaust gases. An actuating flap in the conduit is moved from closed to open position upon impingement of exhaust gas on the flap.

Fuel supply control for rocket-type jet propulsion units (2,814,929). A. W. Morley and A. R. Mortimer, Ickenham, England, assignors to D. Napier & Son, Ltd.

Bullet-like member extending into and axially movable within the nozzle passage of a reaction chamber to vary its cross-sectional area. As liquid propellant control valves are opened, the member is moved progressively to increase the area of the passage, and the supply working fluid is increased correspondingly.

Ejection seat thruster (2,815,008). G. E. Hirt, New Haven, Conn., assignor to Talco Engineering Co., Inc.

Firing of a cartridge within a housing actuates a piston to move hydraulic fluid in a cylinder. An orifice plate restricts the flow of fluid from the cylinder to an adjacent buffer casing.

Fuel (2,815,270). E. A. Lawrence and F. L. von Brecht, Monrovia, Calif., assignors to Aerojet-General Corp.

Fuel comprising 20 to 40 per cent (by volume) of nitropropane dissolved in nitromethane, and containing chromium acetonyl acetonate.

Fuel (2,815,271). F. Zwicky, F. J. Ewing, J. M. Carter and A. J. Stosick, Pasadena, Calif., assignors to Aerojet-General Corp.

Self-combustible, shock-proof stable fuel comprising a mixture of nitromethane with 25 per cent to 70 per cent (by volume) of the mixture of nitroethane and chrome acetonyl acetonate.

Vertically airborne aircarft design (181,599). N. E. Nelson and J. B. Reichert, Los Angeles, Calif., assignors to Doak Aircraft Co.

Ducted fan type of aircraft supported in vertical position on the ground by shock-absorbing casters at the tips of directional fins.

Remote control fuze removing device (2,815,565). E. M. Johnson and R. Tripp, Vallejo, Calif., assignors to the U. S. Navy.

A vise which may be raised and lowered mounted beneath a drive head and fuse puller for holding ammunition to be defuzed. Clutch fingers engage when the drive head is rotated, unscrewing the fuze from the projectile.

Variable area nozzle (2,815,643). F. L. Geary and W. G. Taylor Jr., Glastonbury, Conn., assignors to United Aircraft Corp.

Flaps pivotally mounted to vary the area of a duct outlet. Pivots are located inwardly from their ends. Sealing means extend around the duct at the forward ends of flaps, forming a chamber in communication with the space between the duct and flaps.

Diffuser (2,815,770). A. G. Thorp II, Wallingford, Pa., assignor to Westinghouse Electric Corp.

Preformed section for use between the compressor and combustion sections of an axial flow gas turbine. It comprises a pair of converging and a pair of diverging concentric tubular members spaced to form inner and outer annular fluid conduit sections.

Control system for dual rotor pump drives (2,816,417). D. J. Bloomberg, Newton, Mass., assignor to General Electric Co.

Gas turbine arrangement of separate means for supplying fuel to part of the arc of one tier of blading on each rotor. Pump generated pressures govern operation of the fuel supply means.

Propellant displacement gas generators (2,816,419). H. E. Mueller, Kenmore, N.Y., assignor to Bell Aircraft Corp.

Container of ammonium carbonate compound adapted to progressively decompose when heated, evolving large quantities of gas to the oxidant and fuel tanks.

High speed motor vehicle (2,816,615). L. Kraus, Stuttgart-Rotenberg, Germany, assignor to Daimler-Benz Aktiengesellschaft.

Jet producing device including a rotary blower with its axis at an angle to the vertical central plane of the vehicle. When driving through a curve, a jet of air is discharged to counteract the effect of centrifugal force.

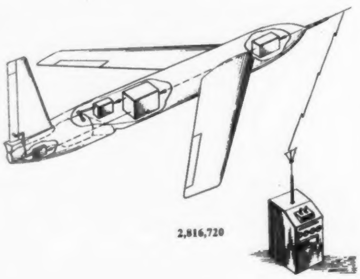

2,816,720

Incremental remote radio control system (2,816,720). W. G. Hodson, W. E. Peterson, H. H. Kenkel, J. J. Hagopian and S. R. Hennies, Englewood, Calif., assignors to Northrop Aircraft, Inc.

System in which the control signals are in increments, or pulses, rather than being continuously proportional. Zero-drift is eliminated, rendering the attitude of the controlled vehicle exactly in correspondence with the indications of the controller.

Rocket powered aerial vehicle (2,816,721). R. J. Taylor, Buffalo, N.Y., assignor to the U. S. Navy.

Spaced forward and rearward combustion chambers located symmetrical with the vehicle. Propellant burns rearwardly in the forward chamber and forwardly in the rearward chamber. Thus, as the propellant in both chambers is consumed at an equal rate, the center of gravity of the rocket remains constant.

Technical Literature Digest

M. H. Smith, *Associate Editor,* **and M. H. Fisher,** *Contributor*
The James Forrestal Research Center, Princeton University

Combustion, Fuels and Propellants

Hydrogen Peroxide and the Peroxide Compounds, by M. E. Pozina, Moscow, 1951, 475 pp. (*Mass. Inst. Tech., Dept. Chem. Engng., Rep.* 52, April 1957).

Phase Relationships in the Three Component Liquid System CO_2-H_2O-C_2H_5 OH at High Pressures, by Louis C. W. Baker and Thomas F. Anderson, *J. Amer. Chem. Soc.*, vol. 79, May 5, 1957, pp. 2071–2074.

Electronic Spectra of Cyclic Aromatic Hydrocarbon Radicals and Ions by H. C. Longuet-Higgins and K. Lenore McEwen, *J. Chem. Physics*, vol. 26, April 1957, pp. 719–723.

Gaseous Detonations in Mixtures of Cyanogen and Oxygen, by H. Milton Peek and R. G. Thrap, *J Chem. Physics*, vol. 26, April 1957, pp. 704–745.

Infrared Spectrum of Solid Nitrous Oxide, by David A. Dows, *J. Chem. Physics*, vol. 26, April 1957, pp. 745–747.

Statistical Mechanics of Liquid-Vapor Equilibrium, by B. Widom, *J. Chem. Physics*, vol. 26, April 1957, pp. 887–893.

Thermodynamic Formulas for Two-Phase Systems, by James C. M. Li, *J. Chem. Physics*, vol. 26, April 1957, pp. 909–913

Research on the Mechanism of Oxydation of Single Iron Crystals at High Temperature and Under Low Oxygen Pressure, by Jean Bardolle, *France, Ministere de l'Air, Pub. Sci. Tech.* 327, 1957, 62 pp. (in French).

Titanium Cut J54 Weight by 16 Per Cent, by D. C. Goldberg, *Aviation Age*, vol. 27, June 1957, pp. 112–115.

Researches on Corrosion and Inhibition. Adsorption, Inhibition and the Langmuir Equation, by George S. Gardner, *J. Franklin Inst.*, vol. 263, June 1957, pp. 523–535.

On the Activation Energy of High Temperature Creep in Metals, by Paul Feltham, *Philos. Mag.*, 8th Series, vol. 2, May 1957, pp. 584–588.

Rocket Propellants for Underwater Missiles, by Alfred J. Zaehringer, *Missiles and Rockets*, vol. 2, May 1957, pp. 91–93.

Reaction Bomb for Use at Elevated Temperatures and Pressures, by Edwin M. Larsen and James J. Leddy, *Rev. Sci. Instrum.*, vol. 28, April 1957, pp. 292–293

A Theory of Inflammability Limits and Flame-Quenching, by D. B. Spalding, *Proc. Royal Soc.*, vol. A240, April 24, 1957, pp. 83–89.

Instrumentation, Telemetering, Data Recording

Data Reduction Center Clears Way for Missile Research, *Industrial Labs.*, vol. 8, April 1957, pp. 48–49.

Accuracy of the Cutler-Hammer Recording Gas Calorimeter when Used with Gases of High Heating Value, by John H. Eiseman and Elwin A. Potter, *J. Res. Nat. Bur. Standards*, vol. 58, April 1957, pp. 213–226.

Instrumentation Used in Measurement of the Three-Dimensional Flow in an Axial Flow Compressor, by J. Horlock, *Gt. Brit., Aeron. Res. Council, Curr. Pap.* 321 (*ARC TR* 17518), 1957, 12 pp.

NAMTC Instrumentation Status Report as of 1 March 1950 with Addendum to 1 March 1951, *Naval Air Missile Test Center, Tech. Mem. Rep.* 48, May 1951, 106 pp. (Declassified from Confidential by authority of *ASTIA TAB* 123, p. 40, 4/15/57.)

Preset Gating Unit for Aeroballistic Testing, by Samuel E. Dorsey, *Electronics*, vol. 30, May 1957, pp. 164–169.

Missile Telemeter Uses Transistor Amplifier, by John H. Porter, *Electronics*, vol. 30, May 1957, pp. 170–175.

Ultra-High-Speed Flash Chemicrograph, by J. S. Courtney-Oratt and Charles M. Huggins, *Rev. Sci. Instrum.*, vol. 28, April 1957, pp. 254–255.

Construction and Performance of a High-Speed Cinemicrograph, by J. S. Courtney-Pratt and Charles M. Higgins, *Rev. Sci. Instrum.*, vol. 28, April 1957, pp. 256–262.

Metal System for Chemical Reactions and for Studying Properties of Gases and Liquids, by H. V. Neher and Satya Prakash, *Rev. Sci. Instrum.*, vol. 28, April 1957, pp. 267–270.

Device for Measuring Friction, by James L. Lauer and Patrick J. Friel, *Rev. Sci. Instrum.*, vol. 28, April 1957, pp. 294–295.

Mercury in Quartz Thermometers for Very High Accuracy, by H. Moreau, J. A. Hall and Vera M. Leaver, *J. Sci. Instruments*, vol. 34, April 1957, pp. 147–151.

Telemetering Ground Equipment for the Corporal E, by N. R. Silk, *Calif. Inst. Tech., Jet Propulsion Lab., Progress Rep.* 4-32, July 1947, 31 pp. (Declassified from Confidential by authority of *Calif. Inst. Tech., Jet Propulsion Lab., Pub.* 38, p. 7, 1/3/55.)

Telemetering Nose Equipment for the WAC Corporal, by C. I. Cummings, *Calif. Inst. Tech., Jet Propulsion Lab., Progress Rep.* 4-33, July 1947, 42 pp. (Declassified from Confidential by authority of *Calif. Inst. Tech., Jet Propulsion Lab., Pub.* 38, p. 7, 1/3/55.)

Recent Modifications of Corporal E Telemetering Systems, by F. W. Lehan, *Calif. Inst. Tech., Jet Propulsion Lab., Progress Rep.* 4-60, April 1948, 28 pp. (Declassified from Confidential by authority of *Calif. Inst. Tech., Jet Propulsion Lab., Pub.* 38, p. 8, 1/3/55.)

Corporal E Telemetering Antenna Pattern Based on Model Tests at 400 Megacycles, by Henry Curtis, *Calif. Inst. Tech., Jet Propulsion Lab., Mem.* 4-30, June 1948, 8 pp. (Declassified from Confidential by authority of *Calif. Inst. Tech., Jet Propulsion Lab., Pub.* 38, p. 10, 1/3/55.)

Air Borne Telemetering Equipment for the Corporal, by Alvin W. Newberry, *Calif. Inst. Tech., Jet Propulsion Lab., Rep.* 20-63, Jan. 1952, 38 pp. (Declassi-

EDITOR'S NOTE: Contributions from E. R. G. Eckert, J. P. Hartnett, T. F. Irvine Jr. and P. J. Schneider of the Heat Transfer Laboratory, University of Minnesota, are gratefully acknowledged.

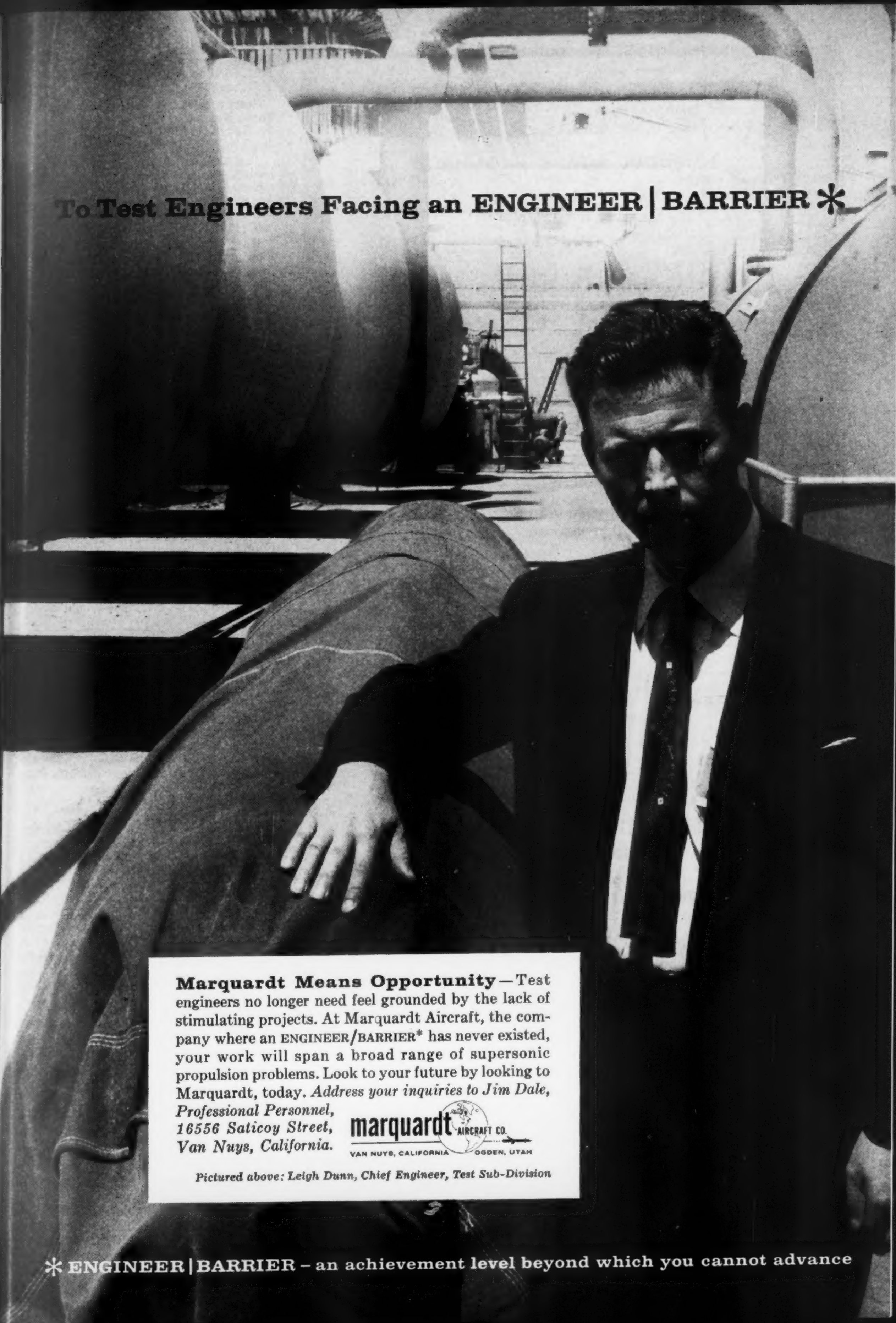
To Test Engineers Facing an ENGINEER|BARRIER *
Marquardt Means Opportunity — Test engineers no longer need feel grounded by the lack of stimulating projects. At Marquardt Aircraft, the company where an ENGINEER/BARRIER* has never existed, your work will span a broad range of supersonic propulsion problems. Look to your future by looking to Marquardt, today. Address your inquiries to Jim Dale, Professional Personnel, 16556 Saticoy Street, Van Nuys, California.
marquardt AIRCRAFT CO.
VAN NUYS, CALIFORNIA OGDEN, UTAH
Pictured above: Leigh Dunn, Chief Engineer, Test Sub-Division
* ENGINEER|BARRIER – an achievement level beyond which you cannot advance

fied from Confidential by authority of *Calif. Inst. Tech., Jet Propulsion Lab., Pub.* 32, p. 15, 1/3/55.)

Theory of Free Molecule, Orifice Type, Pressure Probes in Isentropic Flows, by G. N. Patterson, *Toronto University, Inst. Aerophysics, Rep.* 41, Nov. 1956, 15 pp.

Data Mechanization Speeds Ramjet Engine Testing, *Industrial Labs.*, vol. 9, May 1957, p. 95.

A New Adventure into Micro-Miniaturization. *Instruments and Automation*, vol. 30, April 1957, pp. 667–669.

Programming a Computer, by Martin L. Klein, Frank K. Williams and Harry C. Morgan, *Instruments and Automation*, vol. 30, April 1957, pp. 671–676.

Recording 10 TC/SEC, by E. N. Kaufman, *Instruments and Automation*, vol. 30, April 1957, p. 703.

Rapid Measurement of Thermal Conductivity by Transient Heating of a Fine Thermo-Junction, by R. A. W. Hill, *Proc. Royal Soc.*, vol. A239, April 9, 1957, pp. 476–486.

High Speed Systems of Wind Tunnel Data Handling, by J. Lukasiewicz, J. A. Van der Bliek, and J. G. Scott, *North Atlantic Treaty Organization, Advisory Group Aeron. Res. and Dev., Rep.* 17, Feb. 1956, 24 pp.

Absolute Intensities and Line Width Measurements, by D. Weber, *Calif. Inst. Tech., Daniel and Florence Guggenheim Jet Propulsion Center, Tech. Rep.* 23, March 1957, 6 pp.

Cytac: Air Force's New Position-Fixing System, by Henry P. Steier, *American Aviation*, vol. 20, April 8, 1957, p. 52.

The Application of Rocket Sled Techniques to Flutter Testing, by W. R. Laidlaw and V. L. Beals Jr., *Inst. Aeron. Sci., Prepr.* 666, Jan. 1957, 38 pp.

Technique for Flutter Tests Using Ground Launched Rockets, with Results for Unswept Wings, by W. G. Molyneux, F. Ruddlesden and P. J. Cutt, *Gt. Brit. Aeron. Res. Council, R&M* 2944 (Formerly *ARC TR* 13562 and 14606, *Roy. Aircr. Estab., Rep. Structures* 72 and 118), 1956, 19 pp.

Materials of Construction

Properties and Applications of Ferrites in the U. H. F. Faraday Effect, by M. Vassilev, *Fusées et Recherche Aéronautique*, vol. 1, no. 2, Oct. 1956, pp. 143–149 (in French).

Aerodynamics of Jet Propelled Vehicles

Analysis of Supersonic Wind Tunnel Tests on a $\frac{1}{15}$ Scale Model of the Shore to Ship Guided Missile, by J. B. Kendrick, *Calif. Inst. Tech., Jet Propulsion Lab., Mem.* 4–15, Aug. 1947, 31 pp. (Declassified from Confidential by authority of *Calif. Inst. Tech., Jet Propulsion Lab., Pub.* 38, p. 10, 1/3/55.)

Characteristic Methods for Quasilinear Hyperbolic Differential Equations and an Application to Axially Symmetric Supersonic Flow Past an Ogive, by H. K. Forster, *Calif. Inst. Tech., Jet Propulsion Lab., Rep.* 4–34, Aug. 1947, 31 pp. (Declassified from Confidential by authority of *Calif. Inst. Tech., Jet Propulsion Lab., Pub.* 38, p. 6, 1/3/55.)

Some Stability Considerations for a Rocket Launched at Great Altitudes, by H. K. Forster, *Calif. Inst. Tech., Jet Propulsion Lab., Rep.* 4–32, March 1947, 28 pp. (Declassified from Confidential by authority of *Calif. Inst. Tech., Jet Propulsion Lab., Pub.* 38, p. 6, 1/3/55.)

Experimental Investigations with Jet Control Vanes, by W. B. Powell, *Calif. Inst. Tech., Jet Propulsion Lab., Rep.* 4–30, July 1948, 20 pp. (Declassified from Confidential by authority of *Calif. Inst. Tech., Jet Propulsion Lab., Pub.* 38, p. 6, 1/3/55.)

A Comparison of Long Range Surface to Surface Rocket and Ramjet Missile, by R. W. Krueger and J. E. Lipp, *Rand Corp., R*-174, May 1950, 37 pp. (Declassified from Secret by authority of *ASTIA TAB* U-119, p. 46, 2/18/57.)

The Erosion of Meteors and High-Speed Vehicles in the Upper Atmosphere, by C. Frederick Hansen, *NACA TN* 3962, March 1957, 38 pp.

Heat Transfer and Fluid Flow

Study of Chemical Relaxation Behind Shock Waves, by M. Steinberg and T. F. Lyon, *Wright Air Dev. Center., Tech. Rep.* 56–394 (*ASTIA AD* 118050), Jan. 1957, 18 pp.

The Design of Supersonic Nozzles for Rockets, by R. P. Fraser and P. N. Rowe, *Gt. Brit., Directorate Guided Weapons Res. and Dev., D.G.G.W. Rep./EMR/*55/3 (*Imperial College Sci. Tech., Rep. JRL* 28), Oct. 1954, 22 pp., 33 figs.

On Jet Separation in Supersonic Rocket Nozzles, I. The Characteristics of Flow, by P. Eisenklam and D. Wilkie, *Gt. Brit., Directorate Guided Weapons Res. and Dev., D.G.G.W. Rep./EMR/*55/4 (*Imperial College Sci. Tech., Rep. JRL* 29), May 1955, 55 pp., 29 figs.

Matrix Analysis of Heat Transfer Problems, by Louis A. Pipes, *J. Franklin Inst.*, vol. 263, March 1957, pp. 195–206.

Experimental Study of Stagnation Temperature in Free Molecular Flow, by Marcel Devienne, *Fusées et Recherche Aéronautique*, vol. 1, no. 3, Dec. 1956, pp. 261–267 (in French).

The Numerical Integration of the Laminar Compressibility Boundary Layer Equations with Special Reference to the Position of Separation When the Wall Is Cooled, by G. E. Gadd, *Gt. Brit., Aeron. Res. Council, Curr. Pap.* 312, (formerly *ARC TR* 15101), 1957, 17 pp.

Water Cooling Combustion Gases for Cubicle 3 Exhaust Chamber, by S. E. Matthews and C. R. Walton, *Johns Hopkins Univ., Appl. Phys Lab., CF* 2619, Feb. 1957, 6 pp.

Analysis of Heat-Driven Oscillations of Gas Flows, I. General Considerations, by H. J. Merk, *Appl. Sci. Res.*, vol. 6, Sect. A, no. 4, 1957, pp. 317–336.

Stability of Laminar Flow in Curved Channels, by Chia-Shun Yih and W. M. Sangster, *Phil. Mag.*, vol. 2, 8th Ser. March 1957, pp. 305–310.

Fluctuations and Irreversible Thermodynamics, by Laszlo Tisza and Irwin Manning, *Phys. Rev.*, vol. 105, March 15, 1957, pp. 1695–1705.

Spectrum of Turbulent Fluctuations Produced by Convective Mixing of Gradients, by Albert D. Wheelon, *Phys. Rev.*, vol. 105, March 15, 1957, pp. 1706–1716.

Intensity, Scale and Spectra of Turbulence in Mixing Region of Free Subsonic Jet, by James C. Laurence, *NACA Rep.* 1292, 1956, 27 pp. (supersedes *NACA TN* 3561 and 3576).

Survey of the Acoustic Near Field of Three Nozzles at a Pressure Ratio of 30, by Harold R. Mull and John C. Erickson Jr., *NACA TN* 3978, Apr. 1957, 32 pp.

The Cooling of Walls by Parietal Injection, by Jean Berger (Aerothermal Seminar of the Faculté des Sciences de Paris, Année 1954–1955), *France, Ministère de l'Air, Pub. Sci. Tech., Notes Tech.* 63, 1957, 110 pp., pp. 1–11 (in French).

Heat Transfer from Liquid Metals Flowing in Tubes of Circular Cross Section, by Marcel Robin (Aerothermal Seminar of the Faculté des Sciences de Paris Année 1954–1955), *France, Ministère de l'Air, Pub. Sci. Tech., Notes Tech.* 63, 1957, 110 pp., pp. 13–27 (in French).

Skin Heating During Re-entry of Satellite Vehicles to the Atmosphere, by T. R. F. Nonweiler, *J. Brit. Interplan. Soc.*, vol. 16, Jan.-March 1957, pp. 10–21.

The Surface Temperature of a Missile in High Speed Flight, by P. L. Chambre, *Calif. Inst. Tech., Jet Propulsion Lab., Progress Rep.* 4–13, May 1945, 17 pp., 5 figs. (Declassified from Secret by authority of *Calif. Inst. Tech., Jet Propulsion Lab., Pub.* 38, p. 7, 1/3/55.)

The Skin Temperature of the Bumper WAC in High Speed Flight, by J. Lorrell, *Calif. Inst. Tech., Jet Propulsion Lab., Rep.* 4–37, July 1947, 22 pp. (Declassified from Confidential by authority of *Calif. Inst. Tech., Jet Propulsion Lab., Pub.* 38. p. 6, 1/3/56.)

Heat-Transfer Problems of Liquid-Cooled Gas-Turbine Blades, by Henry Cohen and F. J. Bayley, *Proc., Inst. Mech. Engrs.*, vol. 169, no. 53, 1955, pp. 1063–1080.

Oblique Flow Losses in Screen Matrix Heat Exchangers, by W. H. Comtois, *Stanford Univ., Dept. Mech. Engng., Contract Nonr* 225 (23), *Tech Rep.* 29, June 1956, 72 pp.

Research on Application of Cooling to Gas Turbines, by J. B. Esgar, J.N.B. Livengood, and R. O. Hickel, *Trans., ASME*, vol. 79, April 1957, pp. 645–652.

Generalized Optimal Heat-exchanger Design, by D. H. Fix and R. R. Mills Jr., *Trans. ASME*, vol. 79, April 1957, pp. 653–662.

Review of Industrial Applications of Heat Transfer to Electronics, by J. Kaye, *Proc. Inst. Radio Engrs.*, vol. 44, Aug. 1956, pp. 977–991.

Criteria for Validity of Lumpted-Parameter Representation of Ducting Airflow Characteristics, by T. R. Stalzer and G. J. Giedler, *Trans. ASME*, vol. 79, pp. 833–840.

Heat Transfer in the Critical Region. by R. P. Bringer and J. M. Smith, *J. Amer. Inst. Chem. Engrs.*, vol. 3, March 1957, pp. 49–55.

Theoretical Investigation of the Influence of Cooling Wall Height on the Heat Transfer of Condensing Droplets, by R. Gregorig, *Chemie-Ing.-Technik*, vol. 28, Aug.-Sept. 1956, pp. 551–553 (in German).

Heat Transfer to Boiling Binary Liquid Mixtures, by W. R. van Wijk, A. S. Vos, S.J.D. van Stralen, *Chem. Engng. Sci.*, vol. 5, no. 2, April 1956, pp. 68–80.

Heat Transfer in Pipe Flow at High Speeds, by J. E. Bialokoz and O. A. Saunders *Combustion and Boilerhouse Engng.*, vol. 10, no. 11, Nov. 1956, pp. 412–420.

Heat Transfer from Turbulent Flowing Gas in a Tube Inlet, by G. Grass, *Allgem.*

Warmetechnik, vol. 7, no. 2, 1956, pp. 58–64 (in German).

Pressure Loss in Pipes of Cross-Section at High Velocities, by A. Naumann, *Allgem. Warmetechnik*, vol. 7, no. 2, 1956, pp. 32–41 (in German).

Effect of Axial Fluid Conduction on Heat Transfer in the Entrance Regions of Parallel Plates and Tubes, by P. J. Schneider, *Trans. ASME*, vol. 79, May 1957, pp. 765–774.

Jet and Rocket Propulsion Engines

The Problem of Goddard and Optimum Thrust Programming, by Frank D. Faulkner, *Naval Postgrad. School. Res. Pap.* 11, March 1957, 10 pp.

Underwater Propulsion, by Jack W. Hoyt, G. G. Gould, J. F. Brady, S. Wolf and R. M. Dunlap, *Missiles and Rockets*, vol. 2, May 1957, pp. 71–72, 75–77.

Lycoming T53 Gas Turbine, by Anselm Franz, *SAE J.*, vol. 65, May 1957, p. 25.

Turboprops, by Brooke E. Allen, *SAE J.* vol. 65, May 1957, p. 31.

Orion Gas-Generator Turbocompound Engine Provided Unusual Development Problems, by Ralph J. Hooker, *SAE J.*, vol. 65, May 1957, pp. 51–56.

Boeing 502-10c Gas Turbine, by Wallace E. Skidmore, *SAE J.*, vol. 65, May 1957, pp. 57–59.

Processes in Pulse Jet Engines, by Fritz Staab, *Z. Flugwissenschaften*, vol. 5, March 1957, pp. 77–87, 22 ref. (in German).

Investigation of Acceleration Characteristics of a Single-Spool Turbojet Engine, by Frank L. Oppenheimer and George J. Pack, *NACA RM* E53H26, Oct. 1953, 29 pp. (Declassified from Confidential by authority of *NACA Res. Abstracts* 115, p. 12, 5/22/57.)

Altitude Performance of Compressor, Combustor, and Turbine Components of XT38-A-2 Turboprop Engine, by Frederick W. Schulze and William R. Prince, *NACA RM* E54E04, Aug. 1954, 37 pp. (Declassified from Confidential by authority of *NACA Res. Abstracts* 115, p. 12, 5/22/57.)

Temperatures in a J47-25 Turbojet-Engine Combustor and Turbine Sections during Steady-State and Transient Operation in a Sea-Level Test Stand, by C. R. Morse and J. R. Johnston, *NACA-RM* E54K30a, June 1955, 45 pp. (Declassified from Confidential by authority of *NACA Res. Abstracts* 115, p. 12, 5/22/57).

Analysis of a Form of Peak Holding Control, by G. J. Delio, *NACA RM* E56B10, March 1956, 57 pp. (Declassified from Confidential by authority of *NACA Res. Abstracts* 115, p. 12, 5/22/57.)

Removal of Secondary-Flow Accumulations in a Two-Dimensional Turbine Nozzle Passage by Boundary-Layer Bleed, by Robert Y. Wong, *NACA RM* E55E11, June 1955, 22 pp. (Declassified from Confidential by authority of *NACA Res. Abstracts* 115, p. 12, 5/22/57.)

An Experimental Investigation of the Effect of High-Pressure Tail-Pipe Length on the Performance of Solid-Propellant Motors for Rocket-Powered Aircraft, by Charles J. Rodriguez, *NACA RM* L52E12a, Aug. 1952, 37 pp. (Declassified from Confidential by authority of *NACA Res. Abstracts* 115, p. 16, 5/22/57.)

Seal Leakage in the Rotary Regenerator and Its Effect on Rotary-Regenerator Design for Gas Turbines, by D. B. Har-

per, *Trans. ASME*, vol. 79, Feb. 1957, pp. 233–245.

Studies for New Hot Air Engine—3, by H. A. Havemann, N. N. Narayan Rao, P. Jayachandra, and G. C. Garg, *J. Indian Inst. Sci., Sec. B*, vol. 38, July 1956, pp. 172–202.

Experimental Investigation of Turbine Stator-Blade-Outlet Boundary-Layer Characteristics and a Comparison with Theoretical Results, by Warren J. Whitney, Warner L. Stewart and James W. Miser, *NACA RM* E55K24, March 1956, 24 pp. (Declassified from Confidential by authority of *NACA Res. Abs.* 116, p. 29, 7/5/57.)

Distribution of Losses Behind a Compressor Rotor as Measured by a Rotating Rake, by William R. Godwin, *NACA RM* L55F29, Jan. 1956, 66 pp. (Declassified from Confidential by authority of *NACA Res. Abs.* 116, p. 23, 7/5/57.)

Method for Estimating Combustion Efficiency at Altitude Flight Conditions for Combustor Tests at Low Pressures, by Walter T. Olson, J. Howard Childs and Wilfred E. Scull, *NACA RM* E53F17, Aug. 1953, 15 pp. (Declassified from Confidential by authority of *NACA Res. Abs.* 116, p. 16, 7/5/57.)

Application of Stream-filament Techniques to Design of Diffuser between Compressor in a Gas-Turbine Engine, by Norbert O. Stockman, *NACA RM* E55F06, Aug. 1955, 15 pp. (Declassified from Confidential by authority of *NACA Res. Abs.* 116, p. 20, 7/5/57.)

An Investigation of the High Alternating Stresses in the Blades of an Axial Flow Compressor, by J. R. Forshaw, *Gt. Brit. Aeron. Res. Council, Rep. & Mem.* 2988 (formerly *ARC Tech. Rep.* 17132; *Nat. Gas Turbine Estab. Rep.* R157), 1957, 19 pp.

Satellite Rocket Power Plant, by J. O. Crum and S. L. Gendler, *Rand Corp.* RA15027, Feb. 1957, 110 pp. (Declassified from Secret by authority of ASTIA TAB U157, p. 57, 6/24/57.)

High-Temperature Lubricants and Bearings for Aircraft Turbine Engines, NACA Subcommittee on Lubrication and Wear. Appendix A: **High-speed Aircraft Missions,** by C. M. Michaels, Wright Air Dev. Center; Appendix B: **Engine Design Trends Affecting Lubricants and Bearings,** by C. C. Singleterry, Bur. Aeron., Dept. of the Navy; Appendix C: **Problems Encountered at High Temperatures in Lubrication Systems of Turbine Engines,** by G. P. Townsend, Westinghouse Electric Corp; Appendix D: **Turboprop Gear Lubrication Problems,** by C. J. McDowall, Gen. Motors Corp; Appendix E: **Notes on High-Temperature Fluids and Lubricants,** by E. E. Klaus and M. R. Penske, Penn. State College; Appendix F: **NACA Research on Lubricants, Bearings, and Lubrication for High-Temperature Turbine Engines,** by R. L. Johnson and E. E. Bisson; Appendix G: **High-Temperature Bearing Problems,** by F. W. Wellons. *NACA RM* E54D27, July 1954, 101 pp. (Declassified from Confidential by authority of *NACA Res. Abs.* 116, p. 18, 7/5/57.)

An Experimental Investigation of a Flat Ram-jet Engine on a Helicopter Rotor, by Robert D. Powell, Jr., and James P. Shivers, *NACA RM* L55F28, Jan. 1956, 27 pp. (Declassified from Confidential by authority of *NACA Res. Abs.* 116, p. 23, 7/5/57.)

Experimental Determination of Aerodynamic Forces Normal to the Chord Due to Rotating Stall Acting on Compressor Blading, by Donald F. Johnson and

Eleanor L. Costilow, *NACA R M* E57F14, Aug. 1954, 27 pp. (Declassified from Confidential by authority of *NACA Res. Abs.* 116, p. 18, 7/5/57.)

Noise Survey of a Full-Scale Supersonic Turbine-Driven Propeller Under Static Conditions, by Max C. Kurbjun, *NACA TN* 4059, July 1957, 20 pp.

Performance of Inconel 550 Turbine Blades in a Turbojet Engine and Effects of Different Forging Temperatures and Heat Treatments, by C. A. Gyorgak, J. R. Johnston, and J. W. Weeton, *NACA RM* E55F08, Aug. 1955, 55 pp. (Declassified from Confidential by authority by *NACA Res. Abs.* 116, p. 20, 7/5/57.)

Equilibrium Operating Conditions of Turbine-Compressor Gas Generators, by A. Capetti, *L'Aerotechnica*, vol. 37, Feb. 1957, pp. 3–6.

Static Thrust of Turbojet with and without Afterburner; Limitations of Increasing the Compression Ratio of the Compressor, by G. Santangelo, *L'Aerotecnica*, vol. 37, Feb. 1957, pp. 24–28.

Inflow Conditions for Supersonic Compressor with Curved Blades, by Philip Levine, *J. Applied Mech.*, vol. 24, June 1957, pp. 165–169.

Design Progress: Napier Gazell—Power Unit for Helicopters, by Randolph Hawthorne, *Aviation Age*, vol. 28, July 1957, pp. 32–33.

Reds' Type K Outperforms Western Turboprops, by Walter P. Moser, *Aviation Age*, vol. 28, July 1957, pp. 50–55.

Space Dynamics Techniques Hinge on Propulsion System, by John de Nike, Jorgen Jensen and Michael Stoiko, *Aviation Age*, vol. 28, July 1957, pp. 26–31.

Research and Development Trends, *Aviation Age, Research and Development Technical Handbook, 1957–1958*, Section C. Propulsion, pp. C-3–C-9;(Chemical Rockets-Photonic & Ionic Rockets-Gas Turbines & Ramjets-Fuels & Lubricants).

Gas Turbines for Aircraft (Table), *Aviation Age, Research and Development Technical Handbook, 1957-1958*, pp. C-10–C-17; Data Review, pp. C-18, 22–41.

O-Ring Valve Used in Rockets, *Aviation Week*, vol. 67, July 15, 1957, p. 63.

Injection by Concurrent Jets in Liquid Rocket Combustion Chambers, by R. Kling, Mme. G. Chevalerias and A. Maman, *Recherche Aeron.*, no. 57, 1957, pp. 19–22 (in French).

Turbo-Prop Performance Analysis and Flight Planning—A Viscount Operator's Approach, by J. R. Baxter, *J. Royal Aeron. Soc.*, vol. 61, June 1957, pp. 391–404.

Ram-jets, by R. R. Jamison, *J. Royal Aeron. Soc.*, vol. 61, June 1957, pp. 407–421.

Ramjet-Turbojet Combinations for Supersonic Flight, by R. T. DeVault, *SAE J.*, vol. 65, July 1957, pp. 35–38.

Rockets-on-Rotor System, by Donald S. Chatfield, *SAE J.*, vol. 65, July 1957, pp. 51–52.

Small Turbojets Cover Mach 2-3 Range at 50,000-70,000 Ft. Altitudes, by Reece V. Hensley, Stanley R. Shapiro and Raymond Capiaux, *SAE J.*, vol. 65, July 1957, pp. 90–93.

Ramjets Come to Fore as Component Design Improves, by F. R. Garbarine, *Aviation Age*, vol. 28, Aug. 1957, pp. 66–71.

Turboprop v. Turbojet, by Frank Robertson, *Flight*, vol. 72, Aug. 2, 1957, p. 157.

Gyron, *Flight*, vol. 72, Aug. 2, 1957, pp. 163–168.

Index to Advertisers

ULSION